UNIVERSIDADE DE LISBOA
FACULDADE DE CIÊNCIAS
DEPARTAMENTO DE FÍSICA

Atomic structure calculations in lanthanide ions relevant to kilonovae

Ricardo Alexandre Pinto Ferreira da Silva

Mestrado em Física
Especialização em Física Nuclear e Partículas

Dissertação orientada por:
Prof. Dr. José Pires Marques
Prof. Dr. Jorge Sampaio

2021

Acknowledgments

Firstly, I would also like to extend my deepest gratitude to both of my supervisors, Prof. Dr. José Pires Marques and Prof. Dr. Jorge Sampaio not only for the knowledge sharing but mostly for their patience and support during all my work. This gratitude extends to all the professors and colleagues from LIP's NUC-RIA group for all the teachings and for accompanying me during this journey.

I would also like to thank Prof. Dr. Pedro Amaro, for all the insights regarding the FAC code, and Prof. Dr. Gabriel Martinez-Pinedo and all the collaborators of the GSI TNA group for many useful discussions.

Lastly, a special thanks to my family for always encouraging me, and to all my colleagues and friends at FCUL, in particular to André Torcato and Afonso Jantarada for always believing in me.

Resumo

Neste trabalho, tentamos dar resposta a uma das questões mais relevantes nos domínios da física atómica e da física astro nuclear: "De onde surgem os elementos mais pesados da tabelas periódica?". Na verdade, sabe-se que grande parte dos elementos mais pesados que o ferro são produzidos em estrelas gigantes e muito luminosas através de processo "s", um processo de captura lenta ("slow") de neutrões, comparativamente à escala temporal de decaimento β. Contudo, elementos mais pesados (com número de massa $A \gtrsim 140$), onde se incluem os lantanídeos e os actinídeos não são produzidos por estes processos. Para tal, é necessário um fluxo de neutrões superior, de modo a permitir a síntese de isotopos mais massivos, antes de estes se desintegrarem por decaimento β. A este processo de captura rápida de neutrões dá-se o nome de processo r.

Assim, qualquer ambiente que permita que este processo ocorra naturalmente terá que ser extremamente rico em neutrões. As supernovas de tipo II, que resultam do colapso gravitacional do núcleo de uma estrela massiva, foram um dos primeiros locais a serem sugeridos onde elementos pesados podiam estar a ser produzidos por processo r. Desenvolvimentos na modelação destes ambientes levam a crer, no entanto, que estes não possuam as condições necessárias. Todavia, a observação, pela primeira vez em Agosto de 2017, de um transiente eletromagnético associado à colisão de duas estrelas de neutrões, ao qual denominamos por "kilonova" parece indicar que estes ambientes explosivos requerem todas as condições para a formação de elementos por rápida captura de neutrões.

Uma das principais barreiras à modelação do fluxo e das curvas de luminosidade de kilonovas recai na falta de informação sobre as propriedades atómicas de elementos formados por processo r, em particular de elementos do bloco f, lantanídeos e actínideos. Assim, a presente dissertação diz respeito a cálculos de estrutura atómica para estes elementos. Concentrámos-nos, essencialmente, em cálculos dos níveis de energias e da força dos oscilador para transições dipolares elétricas (E1), uma vez que estes são os parâmetros atómicos mais relevantes para a modelação da opacidade do meio e, consequentemente, do fluxo de kilonovas em Equilíbrio Termodinâmico Local (LTE).

É importante referir que cálculos de alta precisão para iões do bloco f são extremamente exigentes computacionalmente, dado ao elevado número de níveis característicos deste elementos. Tendo isto em conta, neste trabalho, realizaram-se cálculos para Nd III e U III, dois iões representativos deste conjunto de elementos. Com isto tentámos, não só colmatar a falta de cálculos de estrutura disponíveis na literatura, mas também transmitir um conhecimento mais profundo sobre as características destes iões, algo essencial para cálculos futuros em larga escala cada vez mais precisos.

O Flexible Atomic Code (FAC) [1], acessível ao público geral, foi o código escolhido para a grande maioria dos cálculos. O código baseia-se no método de Interação de Configurações

Relativista (RCI) à semelhança de outros que códigos que têm sido utilizados em para cálculos sistemáticos destes elementos [2].

Os resultados obtidos para Nd III foram adicionalmente comparados com cálculos obtidos através do método de Multi-configurações Dirac-Fock (MCDF), utilizando o código MCDFGME (Multi-Configuration Dirac-Fock and General Matrix Elements Program) [**Idelicato_1987**], bem como com resultados obtidos por Gaigalas et al. [3] utilizando uma versão do código GRASP (General-purpose Relativistic Atomic Structure Package) [4] e com os dados experimentais disponíveis. Verificámos que os resultados obtidos através do código FAC reproduziam de forma bastante razoável os resultados obtidos tanto pelos outros códigos como de forma experimental, para os níveis de mais baixa energia. No que diz respeito às forças de oscilador, detetámos alguma discrepância de resultados para transições de comprimento de onda mais elevado, particularmente entre as camadas $6d$ e $7p$. Ainda assim, após uma análise sobre a dependência da opacidade com os parâmetros atómicos, verificou-se que o impacto destas transições, que ocorrem entre níveis excitados, teria um impacto marginal nos cálculos de opacidade. Em condições de LTE, os estados de mais baixa energia encontram-se exponencialmente mais preenchidos, fazendo com que excitações desses níveis para níveis superiores sejam mais relevantes.

De facto, notou-se que apenas um número reduzido de linhas têm uma contribuição significativa para a opacidade. Medindo o número destas "strong lines" é possível diretamente aferir e comparar a influencia que certos iões têm para a opacidade. Para além disso, permite reduzir o número total de linhas utilizadas na modelação do espetro de kilonovas, o que é significativo principalmente para lantanídeos e actinídeos, dado o número de linhas extremamente elevado associados a estes iões. Neste trabalho é discutida uma expressão (ligeiramente diferente da utilizada habitualmente na literatura) para medir o impacto de uma linha para a opacidade, que tem em conta o comprimento de onda associado à transição.

Resultados semelhantes aos obtidos para Nd III foram alcançados para os cálculos realizados para U III. Neste caso, o número de niveís para os quais resultados, experimentais e computacionais, estão disponíveis na literatura é bastante menor. Em todo o caso, as níveis de energias obtidos para U III foram comparados com resultados obtidos por Savukov et al. [5] obtidos por um método híbrido conjugando métodos Interação de Configurações e de "Coupled Cluster" linear [6], e com dados experimentais disponibilizados por Blaise et al. Tal como no caso do ião Nd III, os resultados obtidos com FAC concordam com os dados experimentais dentro da margem de incerteza do código de $\Delta E \sim 1$ eV. Ainda assim, o número de configurações utilizadas nos cálculos foi bastante reduzido, o que não permite garantir a convergência dos resultados, nem a inclusão de um grau de correlação eletrónica suficiente que consista numa aproximação razoável à de uma base "completa". Assim, apesar dos bons resultados comparativamente aos dados experimentais, a validação dos mesmos resultados por cálculos mais detalhados é indispensável para garantir a sua fiabilidade.

Por fim, para ambos os iões, foi calculada a opacidade de expansão, em condições de LTE, em função do comprimento de onda. Demonstrámos que as discrepâncias entre cálculos realizados por diferentes códigos, quando existem, têm maior impacto nos comprimentos de onda ultravioleta e visível. Em comprimentos de onda mais longos, a sensibilidade da opacidade com a precisão dos cálculos parece diminuir, o que pode permitir obter resultados fiáveis para a opacidade de lantanídeos e actinídeos através da realização de cálculos em larga escala, mesmo que estes tenham um grau de precisão mais reduzida. Por outro lado, o estudo

de características do espetro que possam ser permitir a identificação de elementos específicos requer um grau de precisão muito superior, principalmente, no que diz respeito aos níveis de mais baixa energia.

Um dos principais resultados deste trabalho prende-se com a opacidade de U III, que mostrámos ser superior, em cerca de uma ordem de grandeza à opacidade de Nd III. Isto é explicado pela maior densidade de níveis de baixa energia existente em U III, o que está relacionado com o maior número atómico Z e maior um maior raio da orbital f de valência em actínidios, comparativamente com lantanídeos. Em geral, antecipamos que esta característica do espectro se estenda para mais pares lantanídeos-actinídeos. Assim, apesar de cálculos mais precisos e para um maior número de iões seja necessário para confirmarem estas observações, é previsível que a opacidade dos actinídeos possa ter um impacto mensurável na luminosidade de kilonovas, apesar se serem esperadas abundâncias muito baixas destes iões nestes ambientes.

Palavras-Chave: opacidade, dados atómicos, kilonovas, forças de oscilador, estrelas de neutrões

Abstract

The present dissertation concerns atomic structure calculations for lanthanide and actinide ions that are significant to kilonovae modeling of the ejecta spectra. In particular, calculations for Nd III and U III, two representative rare-earth ions, were achieved. Therefore, in this work we try to bridge the gap created by the lack of atomic structure calculations f-block ions available in the literature, while also providing valuable insight for future calculations.

We concentrated on level energies and oscillator strength calculations for electric dipole transitions (E1) since these are the most critical atomic parameters for simulating the flux of kilonovae in Local Thermodinamical Equilibrium (LTE). We mainly use the publicly accessible Flexible Atomic Code (FAC) for the computations, which employs a Relativistic Configuration Interaction (RCI) method. Not only that, but we compare our results to those obtained using a Multi-configuration Dirac-Fock (MCDF) method as well as to available computational and experimental data.

We demonstrated that discrepancies in the opacity spectra of Nd III across various calculations are higher at the ultraviolet and visible wavelengths. At longer wavelengths the sensitivity of the opacity with the accuracy of the calculations seems to decrease.

Additionally, we showed the opacity of U III to be about an order of magnitude higher than the opacity of Nd III due to a higher density of levels of the actinide. In general, we anticipate this feature of the spectrum to extend for more lanthanide-actinide pairs and, therefore, that the opacity of actinides to have a measurable impact in the luminosity of kilonovae.

Keywords: opacity, atomic data, kilonovae, oscillator strengths, neutron stars

Contents

List of Figures

List of Tables

List of Acronyms

ASF Atomic State Functions
CCSNe Core Collapse Supernovae
CSF Configuration State Function
DREAM Database on Rare Earths At Mons University
EOL Extended Optimal-Level
FAC Flexible Atomic Code
GRASP General-purpose relativistic atomic structure package
GRASP2K General-purpose relativistic atomic structure package version 2K
IR Infrared
LCC Linearized Coupled Cluster
LTE Local Thermodynamical Equilibirum
MBPT Many body perturbation theory
MCDF Multi-configuration Dirac-Fock
MCDFGME Multi-configuration Dirac-Fock and general matrix elements
NIR Near-Infrared
NIST National Institute of Standards & Technology (US)
NSM Neutron Star Merger
OL Optimal-Level
QED Quantum Electrodynamics
RCI Relativistic Configuration Interaction
SCF Self Consistent Field
SNIa Type Ia Supernovae
UV Ultraviolet

List of Symbols

Symbols related to Astronuclear physics

A	Atomic mass number
I	Intensity of radiation
L_{Sob}	Sobolev lenght
L_{ph}	Distance traveled by a photon
$M_{\odot}$	Solar mass
M_{ej}	Mass of the ejecta
T	Temperature
U_N	Partition function for a charged state of an ion with N electrons
U_e	Electronic partition function
X_{lan}	Mass fraction of lanthanides
Y_e	Electron fraction
Z	Atomic number
$\Delta\nu_{th}$	Thermal line width
α	Extinction Coefficient
κ_{exp}	Expansion opacity of the ejecta
κ	Opacity (Wavelenght independent)
λ	Wavelenght
$\mathcal{L}$	Luminosity
ν	Photon Frequency
σ	Absorption bound-bound cross section
τ	Optical Depth
c	Speed of light in the vacum
k_B	Boltzman Constant
n_n	Neutron density
n_p	Proton density
n	Ionic particle density
v_{ej}	Expansion velocity of the ejecta
v_{th}	Thermal Velocity

Symbols related to Atomic physics

H	Many-body Hamiltonian
J	Total angular momentum
M_{fi}	Transition Matrix Element
W_{fi}	Transition rate
Ψ^{ASF}	Atomic state function
Ψ	Wavefunction
α	Fine structure constant
β	Dirac's β matrix
$\boldsymbol{A}$	Vector Potential
$\boldsymbol{\alpha}$	Dirac's $\boldsymbol{\alpha}$ matrix
$\hbar$	Planks reduced constant
κ	Relativistic quantum number
ϕ	Single electron wavefunction
c	Speed of light in the vacum
e	Fundamental charge
f	Oscillator Strength
g	Statistical weight (related to an energy level)
h	Single-electron Hamiltioninan
l	Angular momentum quantum number
m_e	Electron mass
n	Principal quantum number
E1	Electric dipole transitions
E2	Electric quadrupolar transitions
M1	Magnétic dipole transitions

Chapter 1

Introduction

The field of atomic physics has been known to be connected to many different topics. From medical applications to materials engineering and even in astrophysics. In this work, the importance of atomic physics will be highlighted together with insights from nuclear and astrophysics motivated by a question which has been asked for a long time now: "Where do heavy elements come from?". A great part of the heavier-than-iron elements can be produced in stars from the asymptotic giant branch (AGB stars) through a neutron-capture process called s-process. The "s" comes from the slow capture rate of neutrons from seed nuclei, relative to the competing reaction of β-decay. In addition to the s-process, a more extreme a more extreme process is required, in which the rate of neutron capture is higher than the timescale of beta decay. This process is conveniently called rapid neutron capture (or simply r-process) and, hence, it is the most important process to explain the abundances of heavier elements up to uranium and polonium.

However, for such a process to occur naturally in the universe, the environment in which it is held must be extremely neutron rich. For that reason, core collapse supernovae explosions were suggested as the main site for the production of r-process elements. Recent developments in neutrino and nuclear physics and the lack of observations of its production in supernovae enviroments have led scientists to account for a different scenario - the collapse of two neutron stars. Not only computer simulations seem to show this site to possess the required electron fraction and entropy conditions, but the recent observations seem to agree with most theoretical predictions. One particularly important turning point for the study of r-process nucleosynthesis was the observation of the first electromagnetic counterpart from the collision of two neutron stars: a kilonova. This detection occurred in August 2017 after the detection of gravitational waves from a neutron star merger by the LIGO-Virgo experiment, the well-known GW170817 event. Subsequent triangulation of the source, which was made possible by a worldwide team effort that enabled us to track and find the origin of these gravitational waves quickly enough, allowed us, for the first time, the observation of its electromagnetic counterpart, designated by AT2017gfo. This transient has very specific characteristics that make it unique and distinguishes it from other transients. Its particularly high optical brightness quickly faded away in a couple of days, while its long-lived infrared emission, lasted for almost 2 weeks straight. Such characteristics are consistent with the ones one would expect from an ejecta where r-process heating is dominant. Such features, associated to the rapid color evolution of the ejecta, seem to be in accordance with some of the most recent theoretical models of kilonovae which take them as potential sites for the occurrence of heavy r-process.

Many models have been proposed to explain the optical and near infrared spectral features found in this so-called kilonova. However, there is still today a lack of information about the atomic properties of lanthanide and actinide ions and for that reason most radiation transport simulations are still using atomic data from lighter ions, like Fe, in its calculations. It is expected, however, the opacities of the produced ion to be 10 times higher than the ones associated with iron-like elements [7]. A complete atomic database of the most relevant properties of inner transition elements is required for accurate modeling of the flux and measurement of the abundances of ions which are produced in these environments. One of the main objectives of this work is to perform atomic calculations for some elements of interest, which can also provide better knowledge about differences that may exist between the production of actinides and lanthanides in those sites. More than that, we will also try to draw some conclusions about large-scale calculations for multiple ions and look into the drawbacks of some atomic codes that are used for that purpose.

1.1 Neutron star mergers as a potential r-process site

The origin of heavier-than-iron elements has been an open question in nuclear astrophysics for over 60 years now[8]. There is a consensus that roughly half of those elements are produced by a rapid neutron capture process, or r-process for short. This process is characterized by having a capture timescale shorter than the timescale for β-decay and nucleosynthesis runs along the neutron drip line [9].

In order for the r-process to be viable, it is critical that the stellar environment possesses a high density of neutrons. One of the most common quantities used to quantify the viability of r-process is the electron fraction, defined as the ratio of the density of protons to the total density of baryons, i.e.

$$Y_e \equiv \frac{n_p}{n_n + n_p}. \tag{1.1}$$

Light r-process elements are predicted to be created with Y_e values ranging from 0.5 to 0.25, but heavier elements, such as lanthanides and actinides, are generally produced only in environments with a very high neutron density ($Y_e < 0.25$). Other nucleosynthesis processes, such as s- and p-processes (the latter with capture of protons instead of neutrons), dominate when $Y_e > 0.5$ [10].

High entropy neutrino winds, emerging from the explosion of core collapse supernovae (CCSNe), have been considered one of the promising sources for the r-process. However, recent calculations in the beginning of the century have shown these sites to be unlikely to possess the required neutron-rich and high entropy conditions necessary for heavy elements (with mass number $A \gtrsim 140$) to be produced [11–17]. This strong component of the nuclear process, so-called heavy r-process, is the dominant one, accounting for essentially most of the solar-system abundances. In particular, the advances in nuclear modeling and more and precise radiative transport calculations [17–20] have established the critical role of neutrino interactions in raising the electron fraction to values $Y_e \sim 0.5$, which are not compatible with the production of rare-earth elements. Nevertheless, CCSNe are still considered an important site for the weak r-process contributing to the production of elements between Zn and Mo [19].

Possible exceptions to this picture include the explosions of highly massive stars [21], ν-induced spallation in the He shell [22], and magneto-rotational supernovae [23, 24]. In this latter case, the centrifugal rotation of the proto-neutron acts to reduce the electron fraction to values where heavy r-process is viable. Nevertheless, all these events are considered to be very rare and thus not reproducing the full solar-abundances of heavy elements observed. The recent detection of ^{244}Pu on the ocean floor has also shown abundances of about two orders of magnitude lower than the ones predicted using supernovae explosions as the main site of r-process [25]. On the other hand, recent observations of the electromagnetic counterparts of neutron star mergers [26, 27] have been giving strength to the recent studies of these collisions being associated with the productions of heavy elements by r-process. As already mentioned, the gravitational shock wave detected by the LIGO-Virgo[28] experiment in August 2017, followed by the observation of the first kilonova explosion [29] has been considered a hallmark in physics in astro and nuclear physics bringing a recent interest in this topic as we now have experimental data to which we can compare our previous models with.

The first overview of the physics of the electromagnetic transients associate with neutron star mergers (NSM) (and also neutron star - black hole mergers) was given by Li and Paczyski in 1998 [30]. In general the emission mechanism of kilonovae differs to that of type Ia supernova (SNIa) mostly by the hydrodynamical considerations, of which we won't go into much detail. Nevertheless, some aspects to keep in mind are the following: in mergers, we generally expect the ejection of material to be 2 orders of magnitude lower than in the case of supernovae, with the mass of the ejecta $M_{ej} \sim 0.01 M_{\odot}$ in NSM compared to $M_{ej} \sim 1.4 M_{\odot}$ from SNIa. Moreover, the expansion velocities are much higher for kilonovae of NSM, approaching relativistic velocities of $0.1c$-$0.2c$, while velocities of only 10000 km s^{-1} $\approx 0.03c$ are achieved for supernovae. These values are actually in line with some of the most recent simulations that try to reproduce the spectra of At2017gfo [7].

Another very important distinction is related to a three-part ejection mechanism in binary mergers, that contrasts with the homologous expansion process we find in both SNIa and CCSNe. In the initial phase of the collision, the surface layers of both neutron starts are stripped apart and ejected dynamically in what we call "tidal tails". Such ejecta is constituted mainly by neutrons (due to the nature of the neutron starts merging) and it's still quite cold, since it happens on the initial impact. As the neutron stars start to press into each other, matter gets also squeezed in and ejected into the polar regions. Finally, disk winds can form 1 second after the first set of ejections, blowing away the just formed remnant.

Recent studies have shown a lower electron fraction of $Y_e \lesssim 0.2$ can be maintained in the tidal tail ejecta as they are less subjected to neutrino irradiation [31, 32]. Furthermore, the ejecta properties, in particular in the disk wind, also depend on the remnant created. Most importantly, we should distinguish between the cases where a black hole is promptly formed and the case where a rapidly-spinning neutron star is formed. The main difference between the two scenarios is that is the first case, the flux of neutrinos that interacts with the disk wind ceases with the formation of the black hole, making the electron in the disk higher in the latter scenario where the magnetar is formed.

From the initial very high densities, radioactive elements are synthesized, which contribute to maintaining the initial hot temperature of the majority of the ejecta. As the ejecta expands, the photon diffusion time decreases and eventually the radiation can escape from it. The characteristic luminosity of kilonovae can be approximated by the radioactive heating during

the timescale of the expansion of the ejecta. It is given by the following expression [33]:

$$\mathcal{L} \approx 5 \times 10^{40}\,\mathrm{erg\,s^{-1}} \times \left(\frac{M}{0.01 M_\odot}\right)^{1-\frac{\alpha}{2}} \left(\frac{v_{ej}}{0.1c}\right)^{\frac{\alpha}{2}} \left(\frac{\kappa}{1\ \mathrm{cm^2\ g^{-1}}}\right)^{-\frac{\alpha}{2}}, \tag{1.2}$$

where a constant expansion velocity v_{ej} and opacity k is assumed for a mass M of the ejecta, given in solar masses $M_\odot$.

The opacity of the r-process elements in the ejecta is mainly dependent on bound-bound atomic transitions. It is therefore not surprising that the kilonova light-curve is highly dependent on the ejecta composition. If the Y_e of the ejecta is not sufficiently low ($Y_e \lesssim 0.25$), only light r-process elements will be produced ($28 < Z < 58$). In this case, the main contribution to the opacity is due to elements from the iron group, since they have the larger number of energy levels due to the valence d-shell. Nevertheless, if the ejected matter is sufficiently neutron rich ($Y_e \sim 0.1$) then heavier elements are produced ($58 < Z < 90$). In particular, lanthanides are expected to make up to 10% of the mass fraction of a heavy r-process ejecta.

Lanthanides have, contrary to iron-group elements, valence f-shell electrons, which greatly increases the number of energy levels while reducing the spacing between them. This is known to result in a large opacity ($\kappa \approx 10\ \mathrm{cm^2\ g^{-1}}$) for an ejecta with high mass fraction of lanthanides ($X_{lan} \geq 10^{-2}$), an ejecta with a low mass fraction of lanthanides ($X_{lan} \lesssim 10^{-4}$) is characterized by having low opacity ($\kappa \lesssim 1\ \mathrm{cm^2\ g^{-}1}$). In practice, it means that, if r-process elements are found in kilonovae environments, the amount of light that is able to escape the ejecta is much lower, as they get absorbed in the process of exciting the ions in the medium. This can be easily seen in the synthetic r-process transmission spectra produced by Watson et al. [34] illustrated in fig. 1.1. Here we can see how the presence of heavy r-process elements (from ${}_{56}$Ba to ${}_{92}$U) reduces the transmission of light to a value close to 0 in the ultraviolet (UV) and in the high optical range, while still having a measurable effect in infrared. Besides that, and as also reported in [34, 35] and more recently in [36] strontium has a particular noticeable feature in the Near-Infrared (NIR) at $\lambda \sim 8000$ Å. It has been argued that an identical feature can be found in the spectrum of AT2017gfo, which would indicate the presence of strontium ions in the ejecta.

From the geometry of the collision, two different components of the ejecta can be distinguished [33] - a blue region specially near the poles of the collision, where neutrino ejection is favored and only light r-process is possible, and a red component, favored in the equatorial plane, where heavy r-process is expected to occur. A schematic illustration of the different components of the ejecta is given in Figure 1.2 The inclusion of both components of the ejecta provides a complete theoretical model of the electromagnetic transient of a NSM in from the near UV to infrared wavelengths.

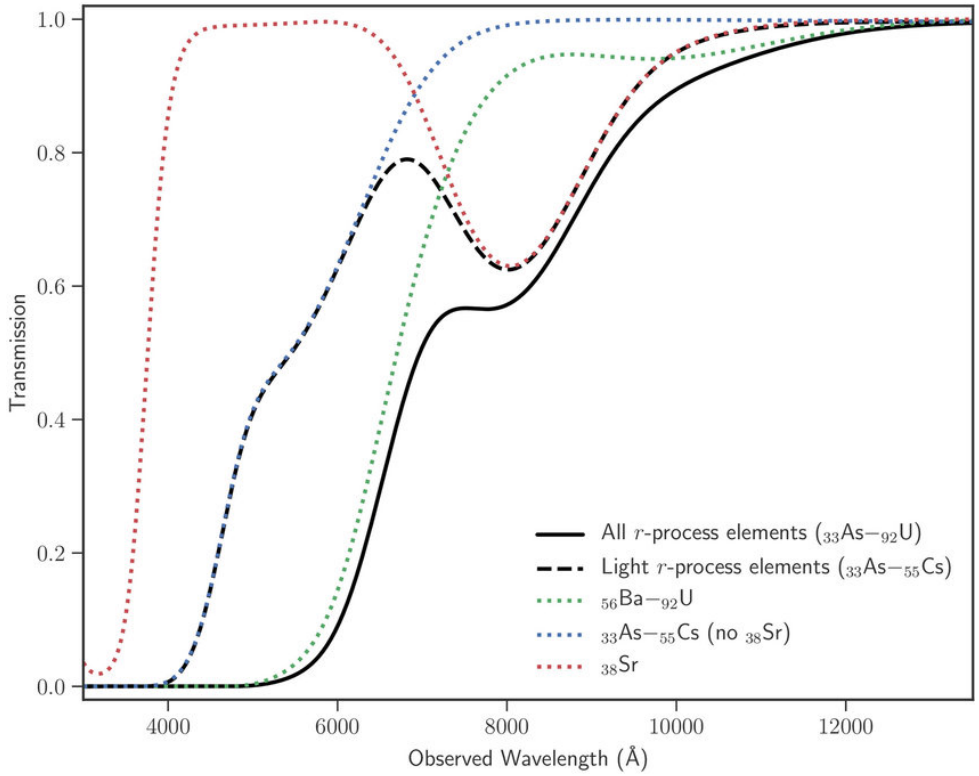

Figure 1.1: Synthetic r-process element transmission spectra for different subset of r-process elements. The solid black line includes the full contribution for all r-process elements, while the dashed black line excludes the contribution of heavy-elements. The spectra are generated using solar r-process abundances. Imaged reproduced from [34] and more details can be found in the original publication.

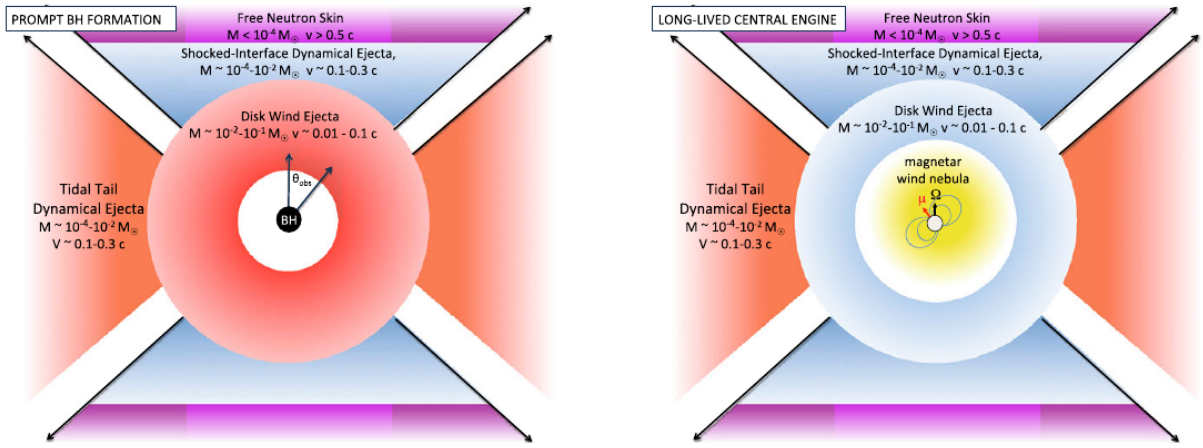

Figure 1.2: Different components of the ejecta from NS-NS mergers for the case of prompt black hole formation (in the left panel) and for a long-lived magnetar remnant (right panel). Red color symbolize a "red" kilonova emission with a high mass fraction of lanthanides, while blue color illustrates "blue" kilonova emission with associated with a higher electron fraction and no lanthanide production. "Red" kilonova emission is expected to peak at NIR wavelengths, while "blue" emission has their peak emission in the UV and optical wavelengths. In the case where a black hole is not promptly formed and the magnetar formed is stable enough, the neutrino emission is not suppressed which increases the electron fraction of the disk wind, reducing its opacity. Imaged reproduced from [32].

1.2 The importance of structure calculations and the lack of atomic data

As already mentioned, the kilonova light curve is highly dependent on the opacity of the medium. That parameter indirectly encodes the dependence of the composition of the medium on the luminosity of the explosion, being a measure of how much light is absorbed in the plasma. This will of course directly depend on the microscopic properties of the different ions and their absorption and scattering cross-section of photons. The biggest contribution to the opacity of kilonovae comes from bound-bound atomic transitions, which can be intuitively understood from the complexity of heavy r-process elements. The number of energy states for a certain atom is directly related to the number of distinct ways the electrons can be distributed within open shells. Hence, the more complex an atom is, the more possible transitions it will have, which, in terms of opacity, increases the probability of a photon being absorbed by such ion. By counting the number of possible permutations for valence electrons, we can get a simple estimate of the number of levels in a particular electron configuration

$$C = \prod_i \frac{g_i!}{k_i!\,(g_i - k_i)!} \tag{1.3}$$

with k_i representing the number of valence electrons for a given open nl-orbitals i with degeneracy $g_i = 2(2l_i + 1)$. The number of lines is expected to scale as C^2. Both lanthanides and actinides ions are characterized by having an open f-shell ($l = 3$), which makes them the most complex atoms in the whole periodic table and with a total number of levels and lines orders of magnitude higher than other heavy ions. Such high complexity is also associated with high degrees of correlation between the electrons, which makes the computation of those levels and transitions a challenge in itself. For obtaining high accuracy in such calculations, nuclear and electronic correlations must be included to full extent. However, this comes with the drawback of having to diagonalize incredibly large Hamiltonian matrices, increasing computation time significantly.

Traditionally, most groups working on atomic calculations privilege accuracy over the amount of calculations produced. Accurate calculations of f-shell elements, due to their extremely high number of levels, will not only require incredibly expensive computational resources, but would take months or even years to achieve. In addition to that, the extreme complexity of these ions makes semi-empirical models of energy levels unreliable. For this reason, lines and levels for lanthanide and actinide ions available in the literature are scarce. In this case, however, for a thorough model of the ejecta opacity and accurate modelling of the kilonovae lightcurves, an extensive set of levels and lines of rare-earth ions is needed.

Regarding this efficiency problem, one of the strategies employed in the most recent computations regarding this data is the use of codes which do not account for correlations individually for each level, but include them under a central local potential felt by all the electrons. Although they do not produce the most accurate results possible, these methods account for a significant part of the existing correlations, while being able to maintain a reasonable computing time. Many of such codes exist, and recent papers have been published on calculations on lanthanides and actinides using Autostructure [37] and Hullac [38] codes (see for example, [2, 33, 39, 40]). In this thesis, most of the calculations were performed using the publicly available Flexible Atomic Code (FAC) which employs a similar method to the

codes just mentioned, based on relativistic configuration interaction (RCI). A more detailed discussion of the method and of some its particularities of the code is supplied in section 2.4.

1.3 Thesis Outline

In this thesis we will discuss some subtleties regarding these calculations while contributing to our own results for the calculations on lanthanides and actinides. Results of different codes will be discussed, with a major focus on the impact of the atomic data on the opacity contribution. In particular, we will assess the impact of both quantity and quality of the data and try to explain why and when the accuracy of individual levels must not be neglected.

With those considerations in mind, this thesis is organized in the following way:

- In chapter 2, a brief review is given on the nuclear physics, astrophysics and atomic physics concepts, which are necessary not only for the computations done throughout this thesis, but most importantly for the analysis and understanding of the results and their implications. We start by explaining why Neutron Star mergers are being regarded as potential sites for (heavy) r-process and what are the main variables or observables we should tackle to study and test this hypothesis. Next, the prescription used for computing the opacity is explained, detailing the approximations used and in which conditions its application is viable. Finally, a brief description of the relativistic atomic structure calculation is given. We highlight some differences between the three main codes discussed during this work: MCDFGME (Multi-Configuration Dirac-Fock and General Matrix Elements program) [41], GRASP (General-purpose Relativistic Atomic Structure Package), particularly the most recent version, GRASP2K [4, 42], and FAC (Flexible Atomic Code) [1].

- Chapter 3 makes up the core of this thesis, where we report and discuss the results of the calculations performed on doubly ionized neodymium and uranium. We compare the results with the (scarce) experimental data available, and with other theoretical calculations, when possible. An in depth analysis of the data is done regarding the impact of the data on the opacity and on comparing the contribution of different elements based uniquely on their atomic properties. We discuss how actinides may have a bigger role on the flux than initially thought, and what consequences do these insights bring to radiation transport models.

- In the last chapter, we present the main conclusions of this work and some perspectives of future work regarding a systematic calculation of open f-elements and the creation of an atomic database of properties relevant to kilonovae models.

Chapter 2

Theoretical Background

2.1 The Sobolev line expansion approximation

As previously stated in the previous chapters, an accurate understanding of the opacity characteristics of the expanding medium is critical for determining the light curves associated with a kilonovae explosion. Previous works by Pinto & Eastman [43–45], in the study of light curves of SNIa (and later confirmed by more recent works in kilonovae [32]), have shown bound-bound transitions to be the major source of opacity, 2 orders of magnitude greater than other contributions from electron scattering and bound-free and free-free transitions. These latter effects, which are related to photoionization and bremsstrahlung processes, only pose minor corrections to the opacity. Nonetheless, they must be accounted for when local thermodynamical equilibrium conditions are not achieved, as they are important to determine the ionization balance in the medium. A closer look to this aspect will be given in Section 2.2.

Our main goal here is, therefore, to characterize the absorptivity of the medium, or, in other words, how does the intensity of the light varies as it moves through the medium. Neglecting any angular dependence of the medium, we can write the variation of the intensity I as:

$$\frac{dI(\nu)}{dr} = -\alpha I(\nu) \tag{2.1}$$

where α is the extinction coefficient, characterizing the rate at which the intensity decreases per unit distance dr. It can also be thought of as the inverse mean free path for a photon in the medium. We can then define an optical depth, denoted by τ as the probability of a photon being absorbed over the whole length of the medium, i.e,

$$\tau(\nu) = \int \alpha dr. \tag{2.2}$$

Solving for the intensity I in Equation (2.1) we get

$$I(\nu) = I_0 e^{-\tau(\nu)} \tag{2.3}$$

with I_0 being a constant associated with the intensity of the light before passing through the medium.

The probability of transmission of radiation (photons) will, therefore, decrease exponentially as $e^{-\tau(\nu)}$. This means that the probability of a photon being capture by an ion or escaping the medium can be described quantitatively by the optical depth. This enables a quantitative

distinction of a thin and thick plasma: for $\tau > 1$ we say that the plasma is optically thick since the probability of a photon escaping the plasma is very low; while on the opposite case of a thin plasma $\tau < 1$ the probability is much higher, culminating on a higher intensity of light.

Nevertheless, the photons, do not simply disappear in the material, as they are absorbed by the different ions that make up the medium. As a result, the number of photons absorbed will be proportional to the absorption cross section of the ions in the medium. This idea can be used to provide a second definition of the optical depth, from a microscopic perspective.

Following a similar reasoning that we apply when we think of the mean free path, which is defined as the number of interactions in a specified area (say 1 cm^2) for a given distance, we can define a column density N counting the number of ions for a specific column area i.e:

$$N[\mathrm{cm}^{-2}] = \int n[\mathrm{cm}^{-3}]dr \tag{2.4}$$

where the integration is performed over the path the photon takes. Considering the cross section $\sigma(\nu)$ for absorption of the photon in a line at frequency, ν we have that

$$\tau(\nu) = N\sigma(\nu) \tag{2.5}$$

with the cross section $\sigma(\nu)$ given in cm^2 so that τ remains dimensionless.

The absorption cross section for a single-transition in the ion actually assumes a simple form, only depending on the absorption oscillator strength f (which is defined in Section 2.3.4) and the line profile $\phi(\nu)$. In the c.g.s. system of units we can write

$$\sigma(\nu) = \left(\frac{\pi e^2}{m_\mathrm{e} c}\right) f\phi(\nu), \tag{2.6}$$

with e as the electron charge (given in Stat Coulomb), m_e the electron mass (in g), the speed of light c given in cm s^{-1} and $\phi(\nu)$ given in seconds, with the oscillator strength f being an adimentional unit.

2.1.1 The Sobolev Limit

In general, the determination of the shape of spectral features is a very complex task, as it requires considerations from both atomic physics and plasma physics, and the interplay of many mechanisms which are responsible for the widths and shapes in the spectra. In explosive environments, thermal fluctuations usually play a major role[1]. The intrinsic thermal broadening for a specific thermal velocity v_{th} is thus given by

$$\Delta\nu_{th} \equiv \frac{v_{th}}{c}\nu_0. \tag{2.7}$$

with the thermal width $\Delta\nu_{th}$ given with reference to the line center ν_0. An illustration of line broadening due to thermal Doppler shift is given in Figure 2.1 The line profile $\phi(\nu_{th})$ will thus be given by a Gaussian function

$$\phi(\nu_{th}) = \frac{1}{\Delta\nu_{th}\sqrt{\pi}} e^{-\frac{(\nu_{th}-\nu_0)^2}{\Delta\nu_{th}^2}} \tag{2.8}$$

[1]In general, the line profile is best described by a Voigt profile, accounting for contributions from collisional broadening, thermal and microturbulent motions. For simplicity, only thermal broadening is considered in the discussion. However, this doesn't affect the main conclusions and arguments considered in the derivation of the Sobolev approximation.

We should note, however, that as the photon is moving through the medium, it is also subjected to Doppler shift from the expansion of the ejecta. It's initial frequency ν will be shifted to ν' following

$$\nu' = \nu \left(1 - \frac{v_{exp}}{c}\right), \tag{2.9}$$

where v_{exp} represents the expansion velocity of the medium. This means that, in general, as the photon changes its comoving (Lagrangian) frame frequency while traveling through the medium [46], it will shift in and out of resonance with multiple lines.

The probability of a photon being absorbed by the medium must account not only for the line profile of the atomic transitions, but also for the shift of the photon due to expansion of the medium. Here we reach the definition of the Sobolev length, specifically named after the Russian physicist V.V. Sobolev, as it was the first to formalize the concept of an interaction length. For this case, it is simply given by the ratio of the thermal velocity to the velocity gradient

$$L_{Sob} = \frac{v_{th}}{dv_{exp}/dr} \tag{2.10}$$

The important point to keep in mind in our specific scenario is that the velocity of expansion of the medium in kilonova (and even in supernova) is much larger than the usual motion associated with thermal line widths as $v_{th} \sim 10^{-5}c$. When this situation occurs, i.e., when $v_{exp} \gg v_{th}$ we reach the so-called *Sobolev limit* which allow us to perform important approximations to the problem.

There are two main consequences when we consider the *Sobolev limit*:

- A photon Doppler shifts over the whole line profile while only traversing through a small part of the ejecta. We call this interaction to be local.
- A photon can come into resonance with multiple lines, which their rest separation is lower than the expansion velocity of the medium (v_{exp}/c)

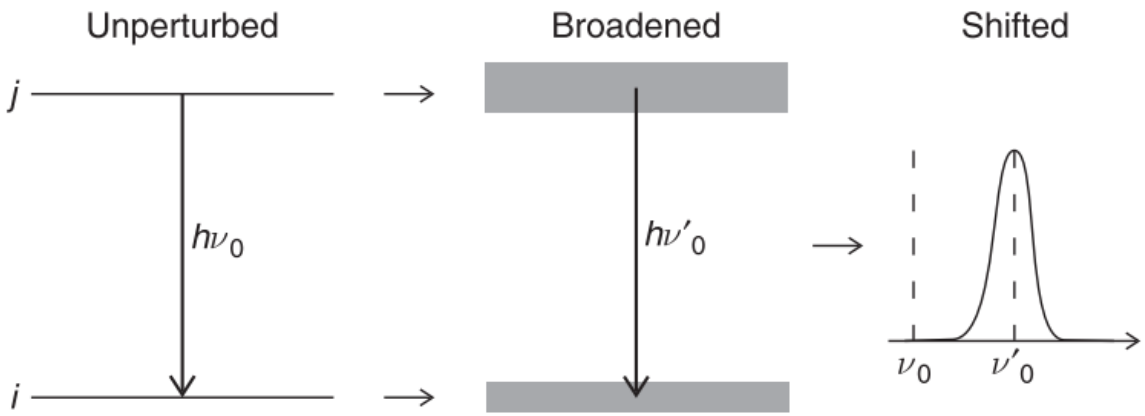

Figure 2.1: Illustration of the broadening of lines due to Doppler shift. It is important to keep in mind that, although this effect is the most prominent at the astrophysical scale, the thermal line width is much smaller than the velocity of expansion in both kilonovae and supernovae environments, i.e. $v_{th} \ll v_{exp}$. Image reproduced from [47].

As in many stellar astrophysics problems, a good first approximation to the model is to assume that the shape of the object does not change during the expansion process. In other words, we assume that the velocity gradient is inversely proportional to time. Under this homologous expansion approximation the radius of the ejecta is given by $R = v_{exp}t_{exp}$ while $L_{Sob} = v_{th}t_{exp}$. Therefore, in practice, in the Sobolev limit $L_{Sob} \ll R$.

The fact that we can assume the photon interactions to be local makes the exact shape of the line profile to be unimportant, as its width is very small when compared to the whole path of the photon. Hence, we are allowed to use an approximation for $\phi(\nu)$ as long as it doesn't greatly overestimate the mean path of the photon. One such approximation and that simplifies our calculations considerably is the following [48]:

$$\phi(\nu) \approx \tilde{\phi}(\nu) = \begin{cases} \dfrac{1}{\Delta\nu}, & \text{if } \nu_0 \leq \nu < \nu_0 + \Delta\nu \\ 0, & \text{otherwise} \end{cases} \tag{2.11}$$

where we are denoting $\tilde{\phi}(\nu)$ as the approximation for $\phi(\nu)$ and $\Delta\nu$ is an approximation of the true line width, with reference to the line center frequency ν_0. Since we are assuming thermal motion to give the major contribution, we can assume $\Delta\nu \approx \Delta\nu_{th}$.

With this major improvement to the line profile function, we now have all the ingredients to calculate the optical depth. Assuming the interaction occurs over a length L_{Sob}, we have that $N \approx n \times L_{Sob}$ from Equation (2.4). Substituting Equation (2.11) in Equation (2.6) and Equation (2.5), and we end up with the following expression for τ for a single absorption line k:

$$\begin{aligned} \tau_k(\nu) &= nL_{Sob}\left(\frac{\pi e^2}{m_e c}\right) f_k \frac{1}{\Delta\nu_{th_k}} \\ &= \left(\frac{\pi e^2}{m_e c}\right) f_k n v_{th} t_{exp} \frac{1}{v_{th}} \frac{c}{\nu_0} \end{aligned} \tag{2.12}$$

Canceling v_{th} and making explicit the dependence on the wavelength using $c/\nu_0 = \lambda_0 \equiv \lambda$ we reach the commonly used approximation for the optical depth

$$\tau_k(\lambda) = \left(\frac{\pi e^2}{m_e c}\right) n t_{exp} f_k \lambda. \tag{2.13}$$

This approximation was first derived in *Moving Envelopes of Stars* by V.V. Sobolev [49], being this expression commonly referenced in the literature as simply Sobolev's optical depth.

Apart from the constants, this expression for the optical depth is entirely dependent on three types of parameters: those that depend on the conditions of the explosion, in this case t_{exp}, since homologous expansion is assumed; n, which must be regarded as the number density of ions in the lower level of the transition, property related to the composition of the medium itself; and the atomic parameters f_k and λ_k, in which we will be focusing most of our attention in this work. For completeness, we will also give some insight on what is needed to compute the level number density at different stages of the kilonova explosion.

2.1.2 The expansion opacity formalism

As it was defined in eq. (2.13), τ_k represents only the optical depth for a single transition. This means that it only accounts for the interaction of the photon with only one line. As we are dealing with multiple interactions over the path of the photon, the optical depth must be given

by a sum over the set of lines that the photon interacts with. In principle, one must account also for the fact that the photon may get stuck in a single line while traveling, as the lines thicken due to the effect of the expansion of the medium. However, as explained previously, this effect of thermal destruction of photons is negligible under the Sobolev limit as the distance traveled by the photon within a line is negligible when compared to total the distance traveled by the photon. As a result, more than assuming a locality, we may view the photon's interaction with a line as instantaneous and not directly reliant on the optical depth of the transition. The total number of interactions a photon has in the range $\left[\nu(1-\frac{v_{exp}}{c}),\nu\right]$ will thus define the effective opacity of the medium. Still under the assumption of homologous expansion, the total distance travelled by the photon can be related to its frequency by

$$\begin{aligned} L_{ph} &= \frac{\nu}{\Delta\nu}\frac{dr}{dv}c \\ &= \frac{\nu}{\Delta\nu}t_{exp}c \end{aligned} \tag{2.14}$$

with the velocity gradient $dr/dv = t_{exp}$ for homologous expansion. The probability of a photon interacting with a line is given by $1-\exp(-\tau_k)$, which makes the probability of interaction of each photon $N_{Lines}\left(1-\exp(-\tau_k)\right)$ with N_{Lines} being the total number of lines that the photon interacts with. More generally, accounting for the fact that τ_k is different for every line we can define an effective total opacity by summing all individual interactions as follows:

$$\tau = \sum_k \left(1-e^{-\tau_k}\right) \tag{2.15}$$

where k runs for all lines over the distance L_{ph}.

It is interesting to see how the effective opacity behaves at limiting values to get a sense of what it really means: for $\tau_k \gg 1$, meaning a high probability of a photon interacting with each line, the whole sum just simplifies to the total number of lines, as expected; on the other hand, when $\tau_k \ll 1$ we get that $\tau \approx \sum_k \tau_k$ meaning that the effective optical depth for a high amount of weak interacting lines will behave similarly as the optical depth of one single thick line whose value is given by the sum of the optical depth for to all interactions.

With this expression for the optical depth, completely derived from microscopical considerations, we can now substitute in Equation (2.2), which defines τ from as a measure of the absorbance of light. We can get the final expression for the absorption coefficient α, which relates the macroscopic observables with the microscopic properties of the medium.

Considering α to be constant over the path of the photon, we simply have from rearranging Equation (2.2)

$$\alpha = \tau/L_{ph} \tag{2.16}$$

In practice, we cannot directly measure the shift nor the distance traveled by the photons at any point in time. This leads to some degree of arbitrariness in how the overall sum is performed, in particular the choice of the range of frequencies to account for the photons path L_{ph}. In this work, we decided to restrict to the usual formalism used in different works (see, for instance, [50]) and divide our wavelength range in small-sized bins $\Delta\lambda_{bin}$ and sum over all lines in that bin. With this approximation, we are assuming that there is no correlation between the interaction probability of individual lines. This assumption holds as long as there is not a

high overlap of lines, or, in other words that the space between strong lines (lines with a high optical depth) is much higher that the thermal width $\Delta\lambda_{th}$. Under this approximation and using Equation (2.14), we finally arrive at a computable final expression for α

$$\alpha(\lambda) = \frac{1}{ct_{exp}} \sum_k \frac{\lambda_k}{\Delta\lambda} (1 - e^{\tau_k}) \tag{2.17}$$

where we write the absorption coefficient as a function of the wavelength for consistency with our previous expression for the optical depth. As for the expansion opacity, which takes into account then mass density of the medium ρ, it is defined as $k_{exp} = \alpha/\rho$ and we get our final expression

$$\kappa_{\text{exp}} = \frac{1}{\rho ct_{exp}} \sum_k \frac{\lambda_k}{\Delta\lambda} (1 - e^{\tau_k}) \,. \tag{2.18}$$

This is the formalism for the expansion opacity, which is used in most of the recent works regarding opacity calculations in supernovae and more recently applied to the collision of NSM and their explosion in a kilonova. For that reason this will be the formalism used for our own opacity calculations. As a summary, the approximations used in deriving this expression are the following:

- Homologous expansion, where we assume that the rate of expansion is proportional to the radius of the explosion. This is a fairly common approximation in astrophysics and reasonably accurate for rapidly expanding mediums.
- The width of the lines is small when compared to the velocity of expansion of the ejecta, or, in other words $v_{th} \ll v_{exp}$. This assumption should be easily satisfied in rapidly evolving environments, where it is an expected a difference of around two orders of magnitude between the thermal and expansion velocities. This makes it such that we can regard the photons interactions as both local and instantaneous.
- We use a simpler approximation for the line profile $\phi(\nu)$, namely $\tilde{\phi}(\nu)$ given in Equation (2.11). Such an approximation is possible given the small width of the lines compared to the range of frequencies traversed by the photon.
- There is no overlap of strong lines, i.e., $\Delta\lambda_{bin}/N \gg \Delta\lambda_{th}$, with N here denoting the number of strong lines over that specific wavelength bin. This assumption is clearly valid for lighter ions, with open p and d-shells. However, it may be concerning when we consider open f-shell elements, where the number of lines is orders of magnitude higher. Recent works (for instance [2]) have also shown these assumptions to also be verified for lanthanides.

It is important to mention a different prescription for the opacity calculations that was suggested by Fontes et al. [51]. In their work they argue that straight discretization of the opacity is applicable to kilonovae, contrary to what happens in SNIa, for which Sobolev's framework was initially developed. Under this line-binned opacity formalism, the total optical depth in a wavelength bin is simply given by the sum of the optical depths of each line considered in the wavelength bin, i.e.

$$\tau_{\lambda,j}^{\text{bin}} = \sum_{i \in \Delta\lambda_j} \tau_i. \tag{2.19}$$

This expression is equivalent to a power series expansion of eq. (2.15) in the limit where $\tau_i \ll 1$. For that reason, it is easy to see that this definition of the optical depth always provides bigger values than the one suggested by Sobolev when this limit does not apply.

This approach has the advantage of allowing tabulation of the opacities, as no expansion properties are required for its computation. However, line-binned opacities are qualitatively and quantitatively different from the ones obtained from the expansion opacity formalism, specially in the intermediate and high optical depth regimes. Even though such calculations may be viable, not many calculations were produced using a line-binned approach, and for the reasons mentioned above the results obtained with both approaches are not directly comparable.

2.2 Ionic density calculations in LTE

For the opacity calculations, as it has become explicit from Equation (2.18) there are two main ingredients required for the opacity calculations: knowledge of the atomic data, specifically transition wavelengths and oscillator strengths for the evaluation of line strengths and absorption cross sections, and knowledge of the level density of the ions in the medium for which the interactions are relevant. For this reason, it is important to consider how we can estimate the population distribution in kilonovae mediums. As it was observed in the introduction, only a small mass of $0.01 M_\odot$ is expected to be ejected from NSM. This, together with the relativistic expansion velocities of the order of $0.2c - 0.3c$ suggest a very low density of the ejecta, even at early times. Specifically, at $t_{ej} \sim 1$ day it is expected densities of $\rho \sim 10^{-13}$ g cm^{-3}. This makes it such that the density of the gas is too low for local thermodynamical equilibrium (LTE) to be established by collisional processes.

On the other hand, the presence of r-process elements points to an optically thick ejecta in the same timescale. As firstly indicated by Pinto and Eastman in [45], this allows for the formation of pseudo-blackbodies, producing a spectrum which is almost identical to a Boltzmann distribution. The physical process is, however, completely difference from the scenario where LTE is established by thermal processes. In the usual picture, collisional processes dominate over the radiative ones, and the random transfer of momentum associated to the collisions ensures a Maxwellian-like distribution of the level populations. In the present case, the LTE distribution occurs from the high number of lines associated to iron group elements and rare-earth elements present in the medium. The high optical depths expected in the UV and optical ranges makes it such that high energy (short wavelength) photons are absorbed in the plasma. Those excited ions will thus, as they de-excite, remit the photons, by fluorescence, typically at higher wavelengths. Since the number of ways this redistribution of energy can occur is so high, due to the high number of lines from the presence of r-process elements, we can expect it to be sufficiently random to form a Boltzmann distribution of the level populations. Hence, under these conditions of a high optical depth, which is expected to be maintained during the early periods of the expansion, the assumption of LTE seems to provide a good approximation.

With this in mind, the level populations, for a particular density of ions n, will take the shape of a Boltzmann distribution for neutral states:

$$\frac{n_l}{n_0} = \frac{g_l}{g_0} n e^{-E_l/k_B T} \tag{2.20}$$

where k_B is the Boltzmann constant (in eV K^{-1}), T is the temperature (in K), E_l (in eV) is the

energy of the lower level of the transition, and g_l and g_0 are the statistical weight of the lower level of the transition and of the ground level, respectively, while n_0 represents the level density population of the ground state. Considering N to be the number of electrons in an ion, the ratio between two consecutive ionic stages is given by the Saha equation:

$$\frac{n_N}{n_{N-1}} = \frac{U_N(T)U_e(T)}{U_{N-1}(T)n_e} e^{-\chi_{N-1}/k_BT} \tag{2.21}$$

where n_e is the electronic density, χ_{N-1} is the ionization potential energy and n_N and n_{N-1} is the ionic density of two consecutive ionic stages with N and $N-1$ electrons, respectively. The electronic partition function U_e is given by:

$$U_e(T) = 2\left(\frac{m_e k_B T}{2\pi\hbar^2}\right)^{3/2} \tag{2.22}$$

While the partition function for the charge states U_N (at a temperature T) can be written in terms of the sum of the statistical weights ($g_i^{(N)}$) of each level weighted by a Boltzmann factor:

$$U_N(T) = \sum_i g_i^{(N)} e^{-E_i^{(N)}/k_BT} \tag{2.23}$$

Although LTE conditions can be applicable to the earlier phases of the explosion, we must keep in mind that the electromagnetic signal can last for days or even weeks after the explosion. At such stages, the ions in the medium will be significantly more spread out (due to the rapid expansion of the medium) and we anticipate a shift from an optically thick to an optically thin plasma. For that reason the assumption of local thermodynamic equilibrium may not be valid at later stages.

Departures from LTE conditions increase substantially the complexity of the opacity calculations, and in particular, the complexity of the atomic physics' contribution. This comes from the fact that, since the Saha-Boltzmann equations are no long valid in non-LTE regimes, the level populations must be ascertained explicitly. For that, we must account for recombination and ionization processes, as well as photon emission and electron ion collisions, in addition to the simple electromagnetic transitions which are required for the opacity calculations in LTE conditions. The population distribution of levels and ions in the ejecta can thus be determined numerically by solving a large set of coupled equations.

2.3 Atomic Calculations

Regarding the atomic parameters necessary for the calculation of bound-bound opacities, we must compute both the oscillator strengths and transition energies for the transitions described in the previous sections. For this computation, a variety of atomic codes are available, all based on the same principles from relativistic electron theory. In this section, we will try to show the general idea of the calculation, as well as the differences that may exist in different approaches.

Throughout this section and what follows from this work, and unless otherwise specified, atomic units (a.u) are used. This system of units is defined by requiring the electron's mass m_e, the electron charge e, the Bohr radius a_0, and the Planck's constant $\hbar$ to be equal to 1. This means that all base units can be defined uniquely by fundamental constants. The most important main base units for this work in their atomic units representation and their values in SI are given explicitly in Table 2.1.

Table 2.1: Atomic unit representation for important base units and their respective conversion factors to the currently accepted values SI values, based on the 2018 CODATA (Committee on Data for Science and Technology) recommendations [52]. In parentheses is the numerical value of the standard uncertainty referred to the corresponding last digits of the SI values, when applicable.

Base Unit	Atomic Unit representation	SI value
Mass	m_e	$9.1093837015(28) \times 10^{-31}$ kg
Length	a_0	$5.29177210903(80) \times 10^{-10}$ m
Charge	e	$1.602176634 \times 10^{-19}$ C
Action	$\hbar$	$1.054571817 \times 10^{-34}$ J s
Energy	$m_e e^4/\hbar^2 \equiv E_h$	$4.3597447222071(85) \times 10^{-18}$ J
Time	$\hbar/E_h$	$2.4188843265857(47) \times 10^{-17}$ s
Velocity	$v_B = \alpha c$	$2.18769126364(33) \times 10^{6}$ m s^{-1}
Potential	E_h/e	27.211386245988(53) V
Electric dipole moment	ea_0	$8.4783536255(13) \times 10^{-30}$ C m
Magnetic dipole moment	$e\hbar/m_e \equiv 2\mu_B$	$1.85480201566(56) \times 10^{-23}$J T^{-1}
Permitivity	$e^2/(a_0 E_h) \equiv 4\pi\epsilon_0$	$1.11265005545(17) \times 10^{-10}$ F m^{-1}

2.3.1 Atomic structure for one-electron systems

To calculate the energy states and wavefunctions of the system, and hence obtain the atomic structure, one must solve the Hamiltonian eigenvalue equation of the form:

$$H\Psi = E\Psi \tag{2.24}$$

where H, Ψ and E represent the Hamiltonian, wavefunction and energy for a bound state.

Employing Dirac's formalism [53, 54] to unsure Lorentz invariance of the electron in the calculation, we can write the Hamiltonian for a single electron as follows

$$h = c\boldsymbol{\alpha} \cdot \boldsymbol{p} + \beta c^2 + V_C\left(r\right) \tag{2.25}$$

with c being the speed of light, $\boldsymbol{p}$ the linear momentum, $V_C(r)$ the nuclear radial potential and $\boldsymbol{\alpha}$ and β the usual Dirac matrices

$$\boldsymbol{\alpha} = \begin{pmatrix} 0 & \boldsymbol{\sigma} \\ \boldsymbol{\sigma} & 0 \end{pmatrix} \quad \text{and} \quad \beta = \begin{pmatrix} 1 & 0 \\ 0 & -1 \end{pmatrix} \tag{2.26}$$

Since the potential is, by nature, spherically symmetric, the interaction has to be both invariant under rotations and reflections, making the solutions eigenfunctions of the angular momentum operators J^2, J_z and the parity operator Π. In addition, it is convenient to write the wave function as a product of their radial and angular components:

$$\phi_{n\kappa m}(r, \Omega) = \frac{1}{r} \begin{pmatrix} P_{n\kappa}(r)\chi_{\kappa m}(\Omega) \\ iQ_{n\kappa}(r)\chi_{-\kappa m}(\Omega) \end{pmatrix} \tag{2.27}$$

with n being the principal quantum number, κ the relativistic angular momentum related to the total angular momentum by $\kappa = (\ell - j)(2j + 1)$, m the magnetic quantum number. Here we use Ω to account for the total angular component. The spherical spinors can be written in terms of the known spherical harmonics like follows:

$$\chi_{\kappa m}(\Omega) = \begin{cases} \begin{bmatrix} \sqrt{\dfrac{\ell + 1/2 + m}{2\ell + 1}} Y_\ell^{m-1/2}(\Omega) \\ \sqrt{\dfrac{\ell + 1/2 - m}{2\ell + 1}} Y_\ell^{m+1/2}(\Omega) \end{bmatrix} & \text{for } j = \ell + \frac{1}{2} \\ \begin{bmatrix} \sqrt{\dfrac{\ell + 1/2 - m}{2\ell + 1}} Y_\ell^{m-1/2}(\Omega) \\ -\sqrt{\dfrac{\ell + 1/2 + m}{2\ell + 1}} Y_\ell^{m+1/2}(\Omega) \end{bmatrix} & \text{for } j = \ell - \frac{1}{2} \end{cases} \tag{2.28}$$

By solving the eigenvalue equation using $H = h$ from Equation (2.25) we can compute large and small radial components $P_{n\kappa}(r)$ and $Q_{n\kappa}(r)$ by solving the resulting coupled system of differential equations

$$\left(V_C(r) + c^2\right) P_{n\kappa}(r) + c\left(\frac{d}{dr} - \frac{\kappa}{r}\right) Q_{n\kappa}(r) = E_n P_{n\kappa}(r) \tag{2.29a}$$

$$-c\left(\frac{d}{dr} - \frac{\kappa}{r}\right) P_{n\kappa}(r) + \left(V_C(r) - c^2\right) Q_{n\kappa}(r) = E_n Q_{n\kappa}(r). \tag{2.29b}$$

This system of equations has an analytical solution for the case where we are only considering the Coulomb potential, which is given by the *Sommerfield fine-structure* formula [55].

$$E = -c^2 \left[1 + \frac{(Z\alpha)^2}{\left[n - j - \frac{1}{2} + \left[\left(j + \frac{1}{2}\right)^2 - (Z\alpha)^2\right]^{1/2}\right]^2}\right]^{-1/2} \tag{2.30}$$

2.3.2 Multi-electron systems

The natural approach when taking a step to a many-electron system is to consider the sum of the individual single-electron Hamiltonians and add a new term corresponding to the inter-electron interactions [56]

$$H = \sum_i^N h_i + \sum_{i<j} V(r_i, r_j) \tag{2.31}$$

with h given by Equation (2.25).

A caveat of extending the eigenvalue problem Equation (2.24) for many electrons is that we do not have any exact solutions like Equation (2.30), nor is it solvable for 3 or more electrons. In practice, and since the problem has a solution for a spherically symmetric potential, the Hamiltonian may be divided into two different parts:

$$H = H_0 + H_1 \tag{2.32}$$

H_0 accounts for the nuclear potential and the central component of the inter-electronic interactions while H_1, which is taken to be much smaller than H_0, accounts for all the non-central two-body contribution of the inter-electronic interactions. Hence, we can write

$$H_0 = \sum_{i=1}^N \left[h_i + U\left(r_i\right)\right] \tag{2.33a}$$

$$H_1 = \sum_{i=1}^{N} \left[-\frac{1}{r_i} - U(r_i) \right] + \sum_{i<j} V(r_i, r_j) \tag{2.33b}$$

where $U(r_i)$ corresponds to the average central potential, which accounts for all spherically symmetric interactions. Many choices for $U(r_i)$ are possible. Independent of the chosen potential, it is critical that it satisfies the boundary requirements that ensure that only the charge from the nuclear interaction is felt near the nucleus, while at further distances, that same charge is screened by the influence of $N-1$ electrons.

Since we are dealing with fermions, the wavefunctions for an N electron system has to be given by an antisymmetrized product of mono-electronic wavefunctions, due to the Pauli exclusion principle. That restriction can be stated conveniently by means of a Slater determinant

$$\psi(\boldsymbol{r}_1, \boldsymbol{r}_2, \ldots, \boldsymbol{r}_N) = \frac{1}{\sqrt{N!}} \begin{vmatrix} \phi_a(\boldsymbol{r}_1) & \phi_b(\boldsymbol{r}_1) & \cdots & \phi_N(\boldsymbol{r}_1) \\ \phi_a(\boldsymbol{r}_2) & \phi_b(\boldsymbol{r}_2) & \cdots & \phi_N(\boldsymbol{r}_2) \\ \vdots & & \ddots & \vdots \\ \phi_a(\boldsymbol{r}_N) & \phi_b(\boldsymbol{r}_N) & \cdots & \phi_N(\boldsymbol{r}_N) \end{vmatrix}. \tag{2.34}$$

However, a single Slater determinant is in most cases not an eigenfunction of J^2 and J_z. To make sure the wavefunctions satisfy that condition, the final wavefunction is written as a linear combination of Slater determinants in what we define as a configuration state function (CSF)

$$\Psi(\boldsymbol{r}_1, \ldots, \boldsymbol{r}_N) = \sum_i d_i \psi^i \tag{2.35}$$

2.3.3 Breit interaction and Radiative Corrections

Before proceeding, it's important to note that, to assure the best precision of the calculations, we must consider quantum electrodynamics (QED) contributions to the interactions. One of the most important contributions, in particular for high Z atoms, is the so-called Breit interaction. It adds a correction to the usual Coulomb repulsion that accounts for the exchange of a virtual photon between two electrons. The interaction potential, including this correction, can be compactly written as [57]

$$\begin{aligned} V(r_i, r_j) = & \frac{1}{r_{ij}} && \text{Coulomb interaction} \\ & - \frac{\boldsymbol{\alpha}_i \cdot \boldsymbol{\alpha}_j}{r_{ij}} \cos(\omega_{ij} r_{ij}) && \text{Gaunt term} \\ & + (\boldsymbol{\alpha}_i \cdot \nabla_i)(\boldsymbol{\alpha}_j \cdot \nabla_j) \frac{\cos(\omega_{ij} r_{ij}) - 1}{\omega_{ij}^2 r_{ij}} && \text{Breit retardation} \end{aligned} \tag{2.36}$$

with $r_{ij} = |(r_i) - (r_j)|$ it's the interelectronic distance and ω_{ij} denotes the energy of the photon exchanged between the two electrons. Both the Gaunt magnetic term and the Breit retardation (written in the Coulomb gauge) term make up the total contribution of the Breit interaction. In the Coulomb gauge, the retardation term can be expanded in a power series. The lowest term, of order α^2, is

$$g^R = \frac{\boldsymbol{\alpha}_i \cdot \boldsymbol{\alpha}_j}{2 r_{ij}} - \frac{(\boldsymbol{\alpha}_i \cdot r_{ij})(\boldsymbol{\alpha}_j \cdot r_{ij})}{2 r_{ij}^3} \tag{2.37}$$

In addition to that, to avoid degeneracy on the energy over the relativistic eigenvalue κ, two types of radiative corrections are also included: the self-energy contribution from the emission, and promptly the absorption of a virtual photon by the electron; and vacuum polarization, where spontaneously occurring electron-positrons pairs are polarized by the atom, changing the effective nuclear charge felt by each electron. These two radiative terms make up the total Lamb shift corrections to the system. The Feynman diagrams that represent these interactions are shown in interactions are shown in Figure 2.2.

The contribution due to vacuum polarization can be written as an effective potential of the form

$$V_{VP}(r) = \sum_{i=1,j=0}^{\infty} V_{i,2j+1}(r) \tag{2.38}$$

with $V_{i,m=2j+1}(r)$ being increasing contributions of the order $\alpha^i(Z\alpha)^m$, with α here representing the fine structure constant.

As for the self-energy, for a hydrogenoid energy level the contribution takes the form:

$$\Delta E_{SE} = \frac{\alpha(Z\alpha)^4}{\pi n^3} mc^2 F_n^{\kappa}(Z\alpha) \tag{2.39}$$

which depends on the quantum number n and κ and where $F_n^{\kappa}(Z\alpha)$ can be expanded in a power series of $Z\alpha$.

We note that, in this case, the shielding effect by other electrons of the nuclear charge must be taken into account, in contrast to the vacuum polarization correction, where no adjustments are needed since we are working with an effective potential.

These QED contributions are usually added as a perturbative correction to the final value of the energy, regardless of the method used for its computation.

(a) Self-energy **(b)** Vacuum polarization

Figure 2.2: Feynman Diagrams for the main radiative quantum electrodynamics correction performed on atomic structure calculations.

Last but not least, to these corrections we also must add that the nucleus is not infinitesimal, but it does have a finite size. Many models exist to account for this, but here we highlight just the main two that are used in most atomic codes. Assuming a spherically uniform charge distribution, we can model the nuclear potential as

$$V_{\text{nuclear}}(r) = \begin{cases} -\frac{Z}{R_{\text{nuc}}}\left(\frac{3}{2} - \frac{r^2}{2R_{nuc}^2}\right) & \text{for } r \leq R_{nuc} \\ \frac{-Z}{r} & \text{for } r \geq R_{nuc} \end{cases} \tag{2.40}$$

We can also model the nuclear charge by assuming a Fermi charge distribution

$$\rho(r) = \frac{\rho_0}{1 + e^{(r-R_{nuc})/a}} \tag{2.41}$$

with a here being a parameter which accounts for the thickness of the distribution and ρ_0 a normalization constant.

2.3.4 Radiative processes

Once the atom is in an excited state, it can undergo radiative decay through the emission of photons, or decay non-radiatively via Auger electron emission. The decay rate of the two processes is important for the complete description of processes involving excited intermediate states, such as two-electron recombination, collision excitation, and subsequent self-ionization excitation. However, our primary interest at the moment is the computation of transition wavelengths and oscillator strengths associated with photon absorption by the atom.

To be able to describe these quantities, we must first focus on studying the general interaction between an atomic system and radiation, and it is evolution with time [58]. In this particular section, Gaussian units are employed, as it is still the most used system to describe electromagnetic phenomena since it makes the expressions more clear and transparent.

We can describe the radiation as electromagnetic plane waves, which propagate in the direction $\hat{\boldsymbol{k}}$:

$$\boldsymbol{A}_{\pm}(\boldsymbol{r},\omega) = \hat{\epsilon}_{\lambda} e^{\pm i\boldsymbol{k}\cdot\boldsymbol{r}} \tag{2.42}$$

where $\boldsymbol{A}_{\pm}(\boldsymbol{r},\omega)$ is the vector potential in the Coulomb gauge ω, ϵ_{λ} describes the radiation frequency and the polarization vector, respectively, with the last one being always orthogonal to the vector potential. The magnitude of propagating direction is $k = |\boldsymbol{k}| = \omega/c$. The general solution of the time-dependent wave equation of a photon (in the Coulomb gauge), assuming closed box boundary conditions in a volume V can hence be given by a superposition of plane wavefunctions

$$\boldsymbol{A}(\boldsymbol{r},t) = \sqrt{\frac{\hbar}{2\epsilon_0\omega V}} \sum_i \left(c_i \hat{\epsilon}_{\lambda} e^{i\boldsymbol{k}\cdot\boldsymbol{r} - i\omega t} + c_i^{\dagger} \hat{\epsilon}_{\lambda}^{*} e^{-i\boldsymbol{k}\cdot\boldsymbol{r} + i\omega t} \right) \tag{2.43}$$

with c_i and $c_i^{\dagger}$ being the photon annihilation and creation operators.

To completely describe the interaction of the system with radiation, we must add to our many-electron Hamiltonian $H_0 + V$ the terms coming from the electromagnetic field and the interaction term

$$H = H_0 + V + H_{EM} + H_I \tag{2.44}$$

The Hamiltonian for the electromagnetic field is given by [58]

$$\begin{aligned} H_{EM} &= \frac{\epsilon_0}{2} \int d^3r \boldsymbol{E}(r,t) \cdot \boldsymbol{E}(r,t) + \frac{1}{2\mu_0} \int d^3r \boldsymbol{B}(r,t) \cdot \boldsymbol{B}(r,t) \\ &= \sum_i \hbar\omega \left(c_i^{\dagger} c_i + \frac{1}{2} \right) \\ &= \sum_i \hbar\omega \left(\mathcal{N}_i + \frac{1}{2} \right) \end{aligned} \tag{2.45}$$

where $c_i^{\dagger} c_i$ simplifies to the number operator $\mathcal{N}_i$.

It is important to note that this particular expression accounts for the non-zero value of the *zero-point energy* of the electromagnetic field in the vacuum, given as

$$E_0 = \frac{1}{2}\sum_i \hbar\omega_i. \tag{2.46}$$

However, being that value not directly measurable, we can "normalize" the electromagnetic field Hamiltonian simply to

$$H_{EM} = \sum_i \omega \mathcal{N}_i \tag{2.47}$$

Regarding the interaction Hamiltonian, the dominant term is

$$\begin{aligned} H_I &= -\sum_i^N \frac{e}{m_i c}\boldsymbol{A}\cdot\boldsymbol{p}_i \\ &= -\sum_i^N \frac{e}{m_i c}\sum_{\boldsymbol{k}\lambda}\sqrt{\frac{2\pi\hbar}{V\omega_{\boldsymbol{k}}}}\left(\boldsymbol{e}_{\boldsymbol{k}\lambda}\cdot\boldsymbol{p}_i\right)\left[c_{\boldsymbol{k}\lambda}e^{i\boldsymbol{k}\cdot\boldsymbol{r}} + c^\dagger_{\boldsymbol{k}\lambda}e^{-i\boldsymbol{k}\cdot\boldsymbol{r}}\right] \end{aligned} \tag{2.48}$$

which accounts for the interactions between the atom and one photon.

To calculate the transition rate, we can make use of the Fermi golden rule

$$W_{fi} = \frac{2\pi}{\hbar}\left|M_{fi}\right|^2\delta\left(E_f - E_i\right), \tag{2.49}$$

where M_{fi} can be computed from perturbation theory for a transition between a final (f) and an initial (i) states using the interaction Hamiltonian in Equation (2.48)

$$M_{fi} = \langle f\left|H_I\right|i\rangle + \sum_j \frac{\langle f\left|H_I\right|j\rangle\langle j\left|H_I\right|i\rangle}{E_i - E_j} + \ldots. \tag{2.50}$$

In first order, the transition matrix element M_{fi} and the correspondent transition rate are

$$M_{fi} = -\frac{e}{mc}\sqrt{\frac{2\pi\hbar c^2}{L^3\omega_k}}\begin{pmatrix}\sqrt{n_{k\lambda}+1}\\ \sqrt{n_{k\lambda}}\end{pmatrix}\left\langle a_f\left|\boldsymbol{p}\cdot\varepsilon_{\boldsymbol{k}\lambda}e^{-i\boldsymbol{k}\cdot\boldsymbol{r}}\right|a_i\right\rangle \tag{2.51}$$

$$W_{fi} = \frac{2\pi}{\hbar}\left(\frac{e}{mc}\right)^2\frac{2\pi\hbar c^2}{L^3\omega_k}\begin{pmatrix}n_{k\lambda}+1\\ n_{k\lambda}\end{pmatrix}\left|\left\langle a_f\left|\hat{\boldsymbol{p}}\cdot\varepsilon_{k\lambda}e^{-i\boldsymbol{k}\cdot\boldsymbol{r}}\right|a_i\right\rangle\right|^2\delta\left(E_{a_f}+\hbar\omega_k - E_{a_i}\right), \tag{2.52}$$

where the occupation numbers $n_{k\lambda}+1$ and $n_{k\lambda}$ are for the cases of photon emission and absorption, respectively.

In order to compute the transition rate we must take into account the explicit dependence on $e^{-i\boldsymbol{kr}}$ We must recall, however, that for both atomic emission and absorption cases, we are typically dealing with radiation in the UV and optical regions with $\hbar\omega \sim 10$ eV making $kr \sim 2\pi\times 10^{-3} \ll 1$. Therefore, we can expand the exponential in a power series

$$e^{-ikr} = 1 - ikr - \frac{1}{2}k^2r^2 + \ldots \simeq 1. \tag{2.53}$$

For most practical instances, we can truncate the expansion at the first value, resulting in the electric dipole approximation (denoted by E1). In any case, the transition matrix element M_{fi} is many times referred to as the multipole operator, denoted as O^L with L denoting the order of the expansion.

The atomic line strength of a transition is simply the absolute value squared of the multipole operator

$$S_{fi} = \left| < f \left\| O^L \right\| i > \right|^2 \tag{2.54}$$

and is a useful quantity to measure the intensity of a transition, being symmetric on the initial and final states.

At this point it is important to introduce the Einstein's A and B coefficients to describe the radiative transitions, since such formalism is still very prevalent in astrophysical considerations. These coefficients depend only on intrinsic atomic properties and arise from statistical considerations. In particular, considering a radiative process between two levels with $E_j > E_1$, in equilibrium, the levels populations N_j and N_i will satisfy the following rate equations:

$$-\frac{\mathrm{d}n_j}{\mathrm{d}t} = \frac{\mathrm{d}n_i}{\mathrm{d}t} = A_{ji}n_j - B_{ij}\rho(\omega_{ij})n_i + B_{ji}\rho(\omega_{ji})n_j \tag{2.55}$$

where $\rho(\omega)$ is the radiation density of the considered transitions.

Three different coefficients are used to describe the three different main radiative processes that can occur: A_{ji} for spontaneous decay, B_{ij} for absorption of a photon and B_{ji} for stimulated (or induced) emission. They can be related to the W_{ij} transitions rates given in Equation (2.52)

$$W^s_{ji} = A_{ji}n_j \tag{2.56a}$$
$$W^i_{ij} = B_{ji}\rho(\omega_{ij})n_i \tag{2.56b}$$
$$W^i_{ji} = B_{ji}\rho(\omega_{ji})n_j \tag{2.56c}$$

where the s and i superscripts are used to distinguish between spontaneous and induced transitions.

Finally, and by using the intrinsic spontaneous emission rate given by A_{ji} we can define the dimensionless response function f which relates the emission rate of an atom with the emission rate of a classical one-electron oscillator:

$$f_{ji} = -\frac{1}{3}A_{ji}/\gamma_{\mathrm{cl}} \tag{2.57}$$

with

$$\gamma_{\mathrm{cl}} = e^2\omega_{21}^2/\left(6\pi\varepsilon_o mc^3\right) \tag{2.58}$$

being the emission rate of the classical oscillator. We call this quantity the emission oscillator strength of the transition (or simply the emission f-value). The absorption oscillator strength is defined by means of detailed balance such that

$$g_i f_{ij} \equiv -g_j f_{ji} \equiv gf \tag{2.59}$$

with g_i and g_j are the degeneracy factors of lower and upper levels, respectively, obtained from the total angular momentum J such that $g = 2J + 1$.

Choice of gauge

It is important to keep in mind that all expressions derived above are presented in the Coulomb gauge. Although this formulation is commonly also referred to as the *velocity* gauge in the literature, the Coulomb gauge is a special case of the more general velocity gauge formulation. In this case $v = \infty$ is fixed by imposing the condition $\boldsymbol{\nabla} \cdot \boldsymbol{A} = 0$ on the vector potential. Equivalent formulas can be deduced in different gauges simply by performing unitary transformations. Of particular interest under the long wavelength approximation is the length (or Göppert-Mayer)gauge, which relates to the Coulomb gauge by

$$H'_L = \hat{U}^\dagger H_V \hat{U}, \quad \hat{U} = \exp\left[\frac{i}{\hbar}\frac{e}{c}\boldsymbol{A} \cdot \boldsymbol{R}\right]. \tag{2.60}$$

where H_L and H_V represent the many-electron Hamiltonian in the length and velocity gauge, respectively.

In principle, the use of any gauge is viable, as they should arrive at the same results. However, this is only true when a complete basis set is used, which in practice is not possible for complex systems. In most numerical applications, the length gauge representation is usually used, as recent works suggest it to be more stable [59]. For this reason, the oscillator strengths presented in this work are presented in the length gauge, unless otherwise specified.

2.4 Different methods of solving the many-electron Dirac equation

Because we are dealing with nonlinear differential equations, solving the Dirac equation analytically for a system with more than one electron is impossible, as we are dealing with a three-body problem which even in classical physics does not have solution. There are two general approaches to proceed with this calculation: perturbative methods, which use many body perturbation theory (MBPT) [58], and variational methods [41, 60, 61], which focus on constructing and minimizing an energy functional under a particular configuration subspace. It is important to note that, regardless of the approach employed, the central component of the Hamiltonian given in Equation (2.33a) can always be solved numerically without any restrictions.

Each technique is briefly explained in the subsections that follow. In this work, however, only variational techniques based on Relativistic Configuration Interactions (RCI) and Multi-Configurational Dirac Fock (MCDF) were utilized. As a result, the methodologies and codes used in this work are given particular attention.

2.4.1 Many Body Perturbation Theory (MBPT) methods

In a perturbative approach, the two-body contributions in Equation (2.33b) are added as a perturbation to the central field approximation. The wavefunctions and eigenvalues are then represented as a power series, which is utilized to produce a series of consecutive improvements to the zeroth-order approximation through a recurrence relation

$$\begin{aligned}
\left(H^{(0)} - E^{(0)}\right)\Psi^{(1)} &= \left(E^{(1)} - H_{\text{pert}}\right)\Psi^{(0)} \\
\left(H^{(0)} - E^{(0)}\right)\Psi^{(2)} &= \left(E^{(1)} - H_{\text{pert}}\right)\Psi^{(1)} - E^{(1)}\Psi^{(0)} \\
\left(H^{(0)} - E^{(0)}\right)\Psi^{(3)} &= \left(E^{(1)} - H_{\text{pert}}\right)\Psi^{(2)} - E^{(2)}\Psi^{(2)} - E^{(3)}\Psi^{(0)} \\
&\vdots
\end{aligned} \tag{2.61}$$

The complexity of the solutions, and the computing time, increases exponentially with the order of the equations. For that reason, even if in theory corrections to an arbitrary order are possible, in most cases only corrections up to third order are considered. It is also worth stressing out that for the first correction to be considered, the potential of the nearest closed shell is used.

2.4.2 Relativistic Configuration Interaction

In these methods, an energy functional is constructed for the spherically symmetric Hamiltonian. Our main goal is to find a stable point, and more specifically a minimum, of that functional,

$$E[\Psi] = \frac{\langle\Psi|H|\Psi\rangle}{\langle\Psi \mid \Psi\rangle} \tag{2.62}$$

which can be achieved by the introduction of different variational Lagrange-like parameters.

One must be careful when dealing with multi-electronic systems. Besides the mutually felt interactions between the electrons, they are also not fully independent, since the movement of the electrons is also influenced by the electronic structure of the system. The antisymmetrization of the wavefunctions, with the use of a Slater determinant, prevents electrons with the same quantum number to be found in the same point in space, accounting therefore for the Exchange or Fermi correlations. To accurately define the wavefunction of the atom, we must also account for the correlation between the position of the electrons due to their Coulomb repulsion (the so-called Coulomb correlations). Thus, we define an atomic state functions (ASFs)to be a linear combination of multiple CSFs with same symmetries,

$$\Psi^{ASF} = \sum_k c_k \Psi_k\left(r_1, \ldots, r_N\right). \tag{2.63}$$

Under our variational approach, we take the mixing coefficients c_k as Lagrange parameters, and so we look for the coefficients which minimize the energy as follows:

$$\frac{\partial E}{\partial c_k} = \frac{\partial\langle\Psi|H|\Psi\rangle}{\partial c_k\langle\Psi \mid \Psi\rangle} = 0 \tag{2.64}$$

The coefficients that are solutions to the above-mentioned set of differential equations define a set of eigenvalues that are the best approximation in the space described by the basis of CSF's. Expanding the number of CSFs utilized would therefore enhance the accuracy of the results; however, increasing indefinitely the basis set is clearly impractical and would increase the computing time without significantly improving the results. For that reason, there are no obvious criteria for selecting suitable configurations. This set may be determined by looking at how the level energies converge as the number of configurations increases.

2.4.3 Multi-configurational Dirac-Fock

In addition to varying the mixing coefficients c_k the electronic Coulomb correlation can also be taken into account by also applying variations to the mono-electronic wavefunctions, with the idea of increasing the number of degrees of freedom of the variational method. This leads to the Multiconfiguration Dirac-Fock (MCDF) method, or Multiconfiguration Hartree-Fock (MCHF) method for its non-relativistic counterpart. In these methods, besides varying the coefficients c_k, we also minimize the energy by varying the mono-electronic ϕ wavefunctions in the following way

$$\frac{\partial \left(E[H] - \sum_{ij} \varepsilon_{ij} \left\langle \phi_i \mid \phi_j \right\rangle \right)}{\partial P_{n\kappa}(r)} \qquad \frac{\partial \left(E[H] - \sum_{ij} \varepsilon_{ij} \left\langle \phi_i \mid \phi_j \right\rangle \right)}{\partial Q_{n\kappa}(r)} \tag{2.65}$$

where the $\epsilon_{i,j}$ are variational parameters introduced to explicitly induce orthonormalization constraints of the wavefunctions. As in the case of a RCI calculation, the variation of the mixing coefficients c_k can be determined by diagonalization of the Hamiltonian. The variation of the wavefunctions, on the other hand, will give rise to a system of coupled differential equations, which we call the Dirac-Fock equations. For a particular wave-function, it can be written as follows:

$$\begin{bmatrix} \frac{d}{dr} + \frac{\kappa_A}{r} & -2c + \frac{V_A(r)}{c} \\ -\frac{V_A(r)}{c} & \frac{d}{dr} - \frac{\kappa_A}{r} \end{bmatrix} \begin{bmatrix} P_A(r) \\ Q_A(r) \end{bmatrix} = \frac{1}{c} \sum_B \epsilon_{A,B} \begin{bmatrix} P_A(r) \\ Q_A(r) \end{bmatrix} + \begin{bmatrix} X_A^Q(r) \\ X_A^P(r) \end{bmatrix} \tag{2.66}$$

where $V_A(r)$ is the sum of the nuclear potential and the direct part of the Coulomb repulsion, while the generalized exchange potentials $X_A^Q(r)$ and $X_A^P(r)$ include all the electronic interactions. The sum over B accounts for all the orbitals, such that $\kappa_B = \kappa_A$ is satisfied. Since there is no analytical solution to this coupled system of equations, these are solved in a self-consistent process until convergence is achieved.

In practice, a MCDF calculation starts by defining a set of trial orbitals, taking for example a set of Thomas-Fermi orbitals. We then proceed to diagonalize the Hamiltonian matrix to obtain the mixing coefficients, c_k which are then used to solve Equation (2.66) until a self-consistent field (SCF) is achieved. This iterative process is repeated until both the mixing coefficients and the wavefunctions converge within a specified threshold.

We should note that, while this technique is an extension of the simpler RCI method, the former differs in that it only requires a single diagonalization of the Hamiltonian as the orbitals are fixed during the process and must be specified in advance. This increase in degrees of freedom enabled by the MCDF method improves calculation accuracy in general, but it comes at the cost of being considerably more computationally expensive.

2.4.4 Atomic Codes

During the last years, several codes were developed to achieve the atomic structure calculation mentioned in the previous sections. Here we will be referencing the ones which are the more relevant to this thesis.

MCDFGME and GRASP2K

Regarding MCDF calculations, it's worth noting that there are only two codes in which the method is fully implemented, the Multiconfiguration Dirac-Fock and General Matrix Elements (MCDFGME) [41] code developed by P. Desclaux and P. Indelicato at the Université Pierre et Marie Curie, and the General-purpose Relativistic Atomic Structure Package(GRASP, being the most recent version acronym GRASP2K) [4, 42], developed by I.P. Grant and Froese Fischer. For the case of MCDFGME both the Coulomb and the Gaunt (magnetic) interaction are included in the Hamiltonian used in the self-consistent approach being the remaining QED corrections, including the Breit retardation, self-energy and vacuum polarization included in a perturbative manner. In contrast, GRASP2K solves the Dirac-Fock equations in a SCF approach utilizing only a Dirac-Coulomb Hamiltonian. The CSFs obtained by that manner are then used at a latter stage for in a RCI calculation, in which Breit and QED leading order corrections are added. At this step, a larger number of configurations that were not included in the MCDF SCF can be included, in order to account for a larger contribution of the electronic correlations.

Another advantage of these codes is that individual levels can be optimized by making the direct and exchange potentials in Equation (2.66) converge for a optimal solution for the average energy of a specific level. This is known as the optimal-level (OL) scheme, with the average energy being defined as

$$E_{av} = \frac{\sum_{i=1}^{n_{\mathrm{L}}} (2J_i + 1)\, E(J_i)}{\sum_{i=1}^{n_1} (2J_i + 1)} \tag{2.67}$$

MCDFGME employs this OL scheme for optimization of the levels with $n_L = 1$. GRASP2K, on the other hand, enables the possibility to extend the optimization to a sum of energies ($n_L > 1$), making use of an extended optimal-level scheme (EOL).

It is worth noting that this optimization of each individual level does not preserve the orthogonality of the wavefunctions and so different methods are built within each code to deal with this restriction.

The Flexible Atomic Code (FAC)

MCDF codes, despite providing more accurate results than other codes, the convergence process is slower and require more computational power and resources. With that in mind, most of the calculations for this work were performed using the Flexible Atomic Code (FAC)[62]. Unlike the two previous codes, the wavefunctions remained fixed after the diagonalization of the Hamiltonian, meaning that FAC uses and RCI method for the calculation, assuming a parametric potential which is felt by all the electrons

$$U_{FAC}(r) = -\frac{Z}{r} + \frac{N-1}{r}\left(1 - \frac{e^{-\lambda r}}{1+ar}\right), \tag{2.68}$$

with λ and a as the two parameters to be determined.

Prior to the diagonalization procedure, the wavefunctions must also be optimized individually and in advance. By taking advantage of the mutual dependence of the wavefunctions and the radial potential, the set of Dirac-Fock-Slater differential equations are solved in a self-consistent approach, using the orbitals determined in the previous iteration for the calculation of the

potential used in the next step. The process is repeated until convergence (within a specified threshold) is reached.

In addition to the RCI techniques, the accuracy of the computations can be improved further by using Many Body Perturbation Theory methods, which are also accessible inside the FAC code. However, the major benefit of this code over other codes, such as the previously stated MCDF codes, is its great computational efficiency and ease of scriptability, thanks to the presence of an optional Python interface. Not only is the input method easier than in other codes, but it is also practical for extracting large amounts of data, which can subsequently be utilized in other projects.

Lastly, FAC is also able to compute continuum processes, like ionization and recombination in the Distorted Wave Born approximation. Such processes are also important in the modeling of kilonovae, and, by using FAC to compute all these quantities within a single framework, we can ensure self-consistency in the data from different calculations.

2.5 Classification of energy levels

In the central field approximation, only symmetric interactions between the electrons and the nucleus are considered. This means that the energy of an atom is completely determined by the assignment of the principal and orbital quantum numbers to all electrons. Under this approach, ions with the same electron configuration $n_1 l_1, n_2 l_2 \dots$ will be assumed to have the same energy. The inclusion of non-spherical interactions is critical for a complete description of the system and an accurate energy determination.

There are two main types of interactions which must be considered- the electrostatic component of the electron-electron interaction that is not considered in the central approximation, and the so-called spin-orbit interaction, which accounts for the interaction of the electron's spin with its motion inside the potential. Both of these interactions lead to a splitting of nl levels into a multitude of different sublevels.

In practice, however, including both interactions with the same degree of impact on the computation is exceedingly difficult. As a result, one usually must consider one of the interactions to be much smaller than the other one, as both contributions are progressively considered in the Hamiltonian, one after another. As a general guideline, one should start with the coupling scheme that is closest to reality and then optimize it, in order to provide reliable results. While electron interactions are dominant for low Z elements and low-lying energy states, spin-orbit and other relativistic effects have a bigger impact in high Z elements and high-energy states.

A different notation is associated with each of these two different coupling schemes. When the electrostatic correlation effects dominate, the total angular momentum L and total spin S are sufficient to characterize the system, defining a LSJ coupling system with labels of the type ${}^{2S+1}L_J$ (with $J = L + S$). As the relativistic contribution rises, LSJ labels can no longer correctly represent the system, and the total momentum $j = l + s$ of a single electron is the only meaningful conserved variable. In this case, we refer to it as a jj type coupling. In principle, any suitable coupling scheme can be used to represent and label the wave function in the structure calculations. However, for consistency reasons, and since low-energy structures are easier to achieve and have been more computed overall, the LSJ notation is the more commonly used in different databases and in the literature. In order to get correct energy estimates for levels with a high degree of relativistic effects, most MCDF and RCI programs are generally adapted to

proceed with the computations using the jj-coupling scheme. For that reason, a transformation between the two labeling systems is inbuilt in the most recent codes to facilitate the comparison between different results from different codes and with experiment. Both MCDFGME and the GRASP2K codes account for this transformation. However, the FAC code, being built with the intention of providing an easy and scriptable code for calculations on highly ionized ions, does not provide a way of performing this calculation within the code itself, and hence the output for each level is identified with a jj type coupling label. This limitation of FAC has no effect on the computations, but it makes direct comparisons between levels computed using FAC and other codes considerably more difficult.

One possible workaround would be to not perform the coupling scheme transformation, maintaining the output of the calculation using a jj-coupling scheme type label on the other codes, namely, GRASP2K and MCDFGME. This would therefore make a comparison with the results from FAC viable. Since the transformation is done automatically in the case of MCDFGME, this would require accessing the unitary transformation matrix and performing an inverse transformation on each calculated level. This is a highly time-consuming task and was not done during this work.

It is also important to note that, as the levels are described as a linear combination of CSF's, the label of the leading CSF is typically used as the label of the level. For that reason, it is quite typical for two or more levels to have the same leading CSF and therefore be assigned the same label. The GRASP codes, with the use of the RATIP package [63] have developed a technique to address this issue by utilizing CSF with a smaller component in the expansion when the leading one's label has already been utilized. Unfortunately, most literature and databases do not yet employ this labeling method, making unambiguous level identification and comparison more difficult.

Since most of the calculations of this work are done with FAC, direct comparison of energy levels between different sets of calculations is not included. The main goal of this thesis, is nevertheless to provide calculations for different atomic parameters which are relevant for kilonovae modeling. As a result, we are more concerned with how the entire set of computations affects the opacity calculations than the accuracy of particular levels.

Chapter 3

Structure Calculations on Lanthanides and Actinides

As it was discussed in the previous sections, lanthanide and actinides, due to their open f-shell structure, play a major role in the opacities of the kilonovae ejecta. However, these elements are so complex that, despite their importance, little progress has been made in both theoretical calculations and spectroscopy experiments. Looking at the NIST Atomic Spectra Database [64], only a very small fraction of the lines for ions with $Z > 57$ have been computed, as it can be seen in the diagram shown in Figure 3.1. That number is particularly low, considering that the number of lines of f-shell elements is 3 to 4 orders of magnitude higher than the ones with an open d-shell.

Due to the lack of atomic data, most preliminary studies of light curves for r-process transients relied on online lists from iron group elements, for which extensive atomic information is available. It can be thought as is it being a reasonable first approximation, as Fe peak elements possess an open d-shell structure. However, recent studies [7, 65] suggest that such an approach can give us, at most, a lower bound and that the expansion opacity for lanthanides can differ from the ones of iron by 3 orders of magnitude [66].

A fresh wave of atomic structure computations on lanthanide ions has been published in recent years [2, 3, 51, 67], with a special focus on ions considered most important to kilonova opacities, such as Nd, Ce and Gd. Nonetheless, reliable computations using codes based on the most advanced MCDF or MBPT techniques that can reach a high degree of precision might take weeks or even months to complete. Using those codes, systematic calculations that take into consideration a significant number of lines (from lanthanide and actinide ions) to generate realistic models would still take a very long time. One of the main limitations is that these detailed calculations are subject to convergence problems. Even though they are a small fraction of the overall calculation, they result in several hundred cases that have to be treated individually, which makes the process time-consuming and tedious[68].

As a result, recent studies from Tanaka et al. [2, 39, 69, 70] are now turning their attention into using not so time-consuming atomic codes, so that a larger spectrum of ions can be computed to give a more complete view of the ejecta. This comes at the cost of a less precise computation, which may affect the opacities. RCI type codes, as the Hullac and Autostructure have been used for this purpose. Although errors of the order of $10\% - 30\%$ can arise in more complex elements, calculations suggest that this difference is not really noticeable in the opacity. This is specially

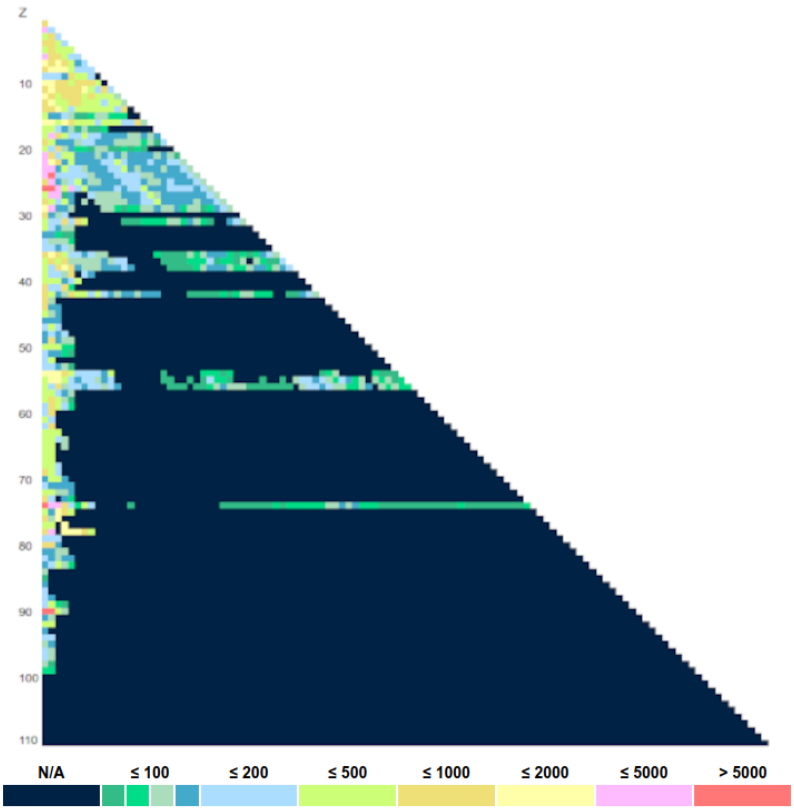

Figure 3.1: Diagram showing the number of the complete line holdings by the NIST Atomic Spectra Database [64] per ion. The color code for the different amount of lines computed is shown at the bottom. Dark blue squares imply that no data is available.

true in the early stages of the explosion, where the number of lines used in the model plays a bigger role than the accuracy of the calculation. Nevertheless, this discussion is still at an initial stage and there's still a lack of agreement on results between different codes and methods used for the calculations.

In this work we are interested, not only in providing reliable calculations for some of the most relevant ions for kilonovae, but also in investigating some of the differences that may arise between different codes, and on what is their impact in the final calculations of the opacities. In the first phase, we started by performing MCDF calculations for the second charged state of neodymium (Nd III) using the MCDFGME code. Neodymium was chosen not only because of its large contribution to the kilonovae opacity, but also because it is one of the most studied lanthanides. This means that data from other calculations is available in the literature to which we could compare the results. This approach was also useful to develop efficient pre- and post-processing scripts to handle the great amount of data that was gathered throughout this work, from energy levels, to transition wavelengths, oscillator strength and finally, bound-bound opacities.

In a second phase, the calculations for that same element were redone using FAC, and the results were also compared with the literature. As will be addressed in detail in the following sections, despite some notable differences in energy levels and oscillator strengths, we show that only small differences are found for the expansion opacities.

Using the knowledge gathered from the FAC calculation on Nd III, and relying on the good convergence of different atomic codes, particularly in the infrared region of the spectra, this work

was extended to investigate the role of actinides on the opacity of the ejecta. This is especially significant because there are just a few publications that incorporate actinides in their opacity models. Yet there is strong evidence that their contribution to opacity may be greater than in the case of lanthanides. With that in mind, calculations on U III were also performed, and presented in light of the prior calculations for neodymium. These are relevant for contemporary kilonovae models and may affect previous results relative to the mass fraction ratio of actinides and lanthanides produced in NSM.

3.1 Calculations on Nd III

A summary of the configurations used in each of the calculations, including the total number of levels and lines computed, is given in Table 3.1. For all calculations, a [Xe] ground configuration was used for the core of the ion.

Table 3.1: Summary of the different set of configurations use on different calculations for Nd III, including experimental results from NIST [64] and the DREAM [71] database. For the calculations of GRASP2K [4], only the configurations from the multireference space are shown, which includes the configurations for which an MCDF calculations was perfromed. The full active space of configurations used in that calculation is shown in [3].

Label	Configurations		All	
	Even	Odd	#Levels	#Lines
FAC (Calculation A)	$4f^4$, $4f^3\,6p$, $4f^2\,5d^2$ $4f^2\,5d\,6s$, $4f^3\,5f$ $4f^3\,7p$, $4f^3\,6f$	$4f^3\,5d$, $4f^3\,6s$, $4f^3\,6d$, $4f^3\,7s$	3206	708077
FAC (Calculation B)	$4f^4$, $4f^3\,6p$, $4f^2\,5d^2$ $4f^2\,5d\,6s$, $4f^3\,5f$ $4f^3\,7p$	$4f^3\,5d$, $4f^3\,6s$, $4f^3\,6d$, $4f^3\,7s$	2702	579796
MCDFGME	$4f^4$, $4f^3\,6p$, $4f^2\,5d^2$ $4f^2\,5d\,6s$	$4f^3\,5d$, $4f^3\,6s$,	2232	178778
GRAPS2K(Gaigalas et al.)	$4f^4$, $4f^3\,6p$, $4f^2\,5d^2$ $4f^2\,5d\,6s$, $4f^3\,5f$ $4f^3\,7p$	$4f^3\,5d$, $4f^3\,6s$, $4f^3\,6d$, $4f^3\,7s$	1453	148759
DREAM	$4f^4$	$4f^3\,5d$	-	51
NIST	$4f^4$	$4f^3\,5d$	29	-

We performed two different FAC calculations (labeled accordingly as Calculation A and B) which are distinguished only by the inclusion in the basis set of the configuration $4f^3\,6f$ in Calculation A (and not in Calculation B).

Only a subset of the configurations used in the FAC calculations was used in the computation performed with the MCDFGME code. Due to computational constraints, the electron-electron correlation was also not fully incorporated. It is worth noting that this basic calculation with MCDFGME required about 2 weeks of calculating time (not considering pre- and post-processing of the data), whereas the simplest (and yet more complete than in the case of MCDFGME when considering the full configuration space) computations with FAC took roughly 2 hours. Although the efficiency of the FAC calculation was vastly superior to the calculation with MCDFGME, it is important to note that this is only the case because the number of configurations included in the RCI calculation of FAC is very low. Typically, RCI calculations must include thousands of configurations to account for a larger extent of the electronic correlations. In such cases, RCI

calculations may require a comparable computing time to MCDF calculations. However, and in particular for the case of FAC, no convergence problems should arise for individual levels, differing from a calculation using MCDFGME where levels are optimized individually.

We compare our results with structure calculations performed with the GRASP2K code by Gaigalas et al. [3]. As mentioned in Section 2.4.4, in this code, MCDF calculations are followed by RCI calculations that include the Breit interaction and leading order QED effects while also including a larger number of configurations not included in the initial MCDF SCF. The full details of the calculation and the construction of the active space are given in [3]. However, as MCDF calculations are so computational expensive, it is possible to perform the calculations entirely using an RCI approach. This is the case of Strategy C (with $5s$ and $5p$) for Nd III use in [3] and, in fact, these results are the ones which best match the NIST data. For that reason, those were the results used for comparison in this work. In this strategy the wave functions were computed using the usual MCDF+RCI approach of GRASP2K[1] and were used in a full RCI calculation, which also included the $5s$ and $5p$ shells in the configuration space. A more in-depth analysis of the importance of these results by Gaigalas is given in Section 3.1.7. We note that only the first 1453 levels, and all the respective E1 transitions between them, are publicly available and only those are used in the opacities calculations provided in the same paper.

Finally, we also compare our results with the NIST and the DREAM databases, with the latter focusing only on experimental results for rare-earth elements. As expected, however, the number of levels and lines measured experimentally in both databases is still very reduced.

3.1.1 Energy Levels

The results for the first 45 energy levels of Nd III using the FAC code are shown in Table 3.2. The states are labeled according to the FAC classification which uses the leading composition of computed eigenvectors in the jj-coupling scheme. In the notation adopted in this work, a given subshell i is denoted as $(n_i l_{i+}^{N_i})_{J_i}$ or $(n_i l_{i-}^{N_i})_{J_i}$. Here n_i and l_i represent the usual principal and angular momentum quantum numbers, N_i represents the number of equivalent electrons within the same subshell while J_i denotes the total angular momentum that the electrons in the subshell couple to. Finally, we adopt the $+$ and $-$ notation to denote $j = l+1/2$ and $j = l-1/2$, respectively. The total angular momentum of the level given by the coupling of all subshells $J = J_1 + J_2 + \ldots$, is also indicated as a subscript. As an example, the ground level of Nd III is labeled as $((4f_-^3)_{9/2}\,(4f_+^1)_{7/2})_4$ - in this case 3 equivalent electrons in a $4f_{5/2}$ subshell couple to give $J_1 = 9/2$ while there is only one electron with $j = 7/2$, and, therefore, $J_2 = 7/2$. The level has a total angular momentum of $J = 4$.

A visual comparison of the results with the results from Gaigalas et al. and with the NIST data is shown in Figure 3.2 while the level density distribution for of all the calculations under analysis can be seen in Figure 3.3.

[1] The results of this calculation were also studied in [3] and are labeled simply as Strategy C.

Table 3.2: First 45 energy levels for Nd III calculated using FAC for the approaches used in this work (Calculation A and Calculation B) and described in the text. The states are labeled according to the FAC classification under a jj-coupling scheme. A full description of the notation used in the level classification is given in Section 3.1.1. The parity (P) of each level and its statistical weight $g = 2J + 1$ are also shown.

Configuration	Level	P	g	Calculation A		Calculation B	
				Energy[eV]	Energy [cm^{-1}]	Energy [eV]	Energy [cm^{-1}]
$4f^4$	$((4f^3_-)_{9/2}\,(4f^1_+)_{7/2})_4$	+	9	0.000	0.00	0.000	0.00
$4f^4$	$((4f^3_-)_{9/2}\,(4f^1_+)_{7/2})_5$	+	11	0.131	1059.29	0.142	1145.44
$4f^4$	$((4f^2_-)_4\,(4f^2_+)_6)_6$	+	13	0.254	2050.96	0.275	2222.25
$4f^4$	$((4f^1_-)_{5/2}\,(4f^3_+)_{15/2})_7$	+	15	0.362	2927.57	0.395	3186.99
$4f^4$	$((4f^1_-)_{5/2}\,(4f^3_+)_{15/2})_8$	+	17	0.451	3638.82	0.495	3995.87
$4f^4$	$((4f^3_-)_{9/2}\,(4f^1_+)_{7/2})_1$	+	3	1.543	12448.83	1.510	12179.45
$4f^4$	$((4f^2_-)_4\,(4f^2_+)_4)_2$	+	5	1.574	12703.00	1.543	12448.29
$4f^4$	$((4f^2_-)_4\,(4f^2_+)_4)_3$	+	7	1.638	13215.90	1.614	13019.66
$4f^4$	$((4f^2_-)_2\,(4f^2_+)_4)_2$	+	5	1.695	13675.57	1.673	13500.64
$4f^4$	$((4f^2_-)_2\,(4f^2_+)_6)_4$	+	9	1.706	13763.62	1.687	13609.60
$4f^4$	$((4f^1_-)_{5/2}\,(4f^3_+)_{15/2})_5$	+	11	1.792	14456.14	1.783	14384.55
$4f^4$	$((4f^3_-)_{9/2}\,(4f^1_+)_{7/2})_6$	+	13	1.829	14756.54	1.799	14514.60
$4f^4$	$((4f^3_-)_{9/2}\,(4f^1_+)_{7/2})_7$	+	15	1.927	15545.87	1.905	15367.47
$4f^4$	$((4f^4_+)_8)_8$	+	17	2.009	16206.81	1.99	16115.25
$4f^3\,5d$	$((4f^3_-)_{9/2}\,(5d^1_+)_{3/2})_6$	−	13	2.089	16854.64	2.024	16327.18
$4f^4$	$((4f^4_-)_4)_4$	+	9	2.291	18483.69	2.026	16344.04
$4f^3\,5d$	$((4f^3_-)_{9/2}\,(5d^1_+)_{3/2})_5$	−	11	2.297	18528.15	2.154	17379.52
$4f^4$	$((4f^3_-)_{9/2}\,(4f^1_+)_{7/2})_2$	+	5	2.311	18641.07	2.230	17988.15
$4f^4$	$((4f^3_-)_{9/2}\,(4f^1_+)_{7/2})_3$	+	7	2.435	19641.45	2.234	18022.07
$4f^4$	$((4f^2_-)_4\,(4f^1_+)_{7/2})_7$	−	15	2.495	20125.32	2.250	18150.44
$4f^4$	$((4f^2_-)_4\,(4f^2_+)_4)_5$	+	11	2.516	20292.87	2.264	18261.27
$4f^4$	$((4f^2_-)_4\,(4f^1_+)_{7/2})_6$	−	13	2.550	20569.32	2.361	19048.85
$4f^4$	$((4f^2_-)_4\,(4f^2_+)_6)_4$	+	9	2.571	20744.00	2.389	19268.46
$4f^4$	$((4f^2_-)_4\,(4f^2_+)_4)_3$	+	7	2.612	21070.00	2.447	19736.73
$4f^4$	$((4f^1_-)_{5/2}\,(4f^3_+)_{15/2})_6$	+	13	2.643	21321.86	2.488	20070.13
$4f^4$	$((4f^2_-)_4\,(4f^1_+)_{7/2})_8$	−	17	2.647	21352.68	2.496	20137.66
$4f^4$	$((4f^2_-)_4\,(4f^2_+)_6)_5$	+	11	2.657	21436.20	2.516	20293.78
$4f^4$	$((4f^2_-)_4\,(4f^2_+)_4)_7$	+	15	2.712	21876.84	2.536	20459.79
$4f^4$	$((4f^3_-)_{9/2}\,(4f^1_+)_{7/2})_2$	+	5	2.745	22146.87	2.545	20529.55
$4f^4$	$((4f^2_-)_4\,(4f^1_+)_{7/2})_7$	−	15	2.747	22156.90	2.579	20806.67
$4f^4$	$((4f^1_-)_{5/2}\,(4f^3_+)_{9/2})_4$	+	9	2.771	22356.95	2.610	21058.01
$4f^4$	$((4f^1_-)_{5/2}\,(4f^3_+)_{15/2})_6$	+	13	2.829	22824.79	2.624	21170.85
$4f^4$	$((4f^2_-)_4\,(4f^2_+)_6)_8$	+	17	2.868	23139.74	2.628	21202.258
$4f^4$	$((4f^2_-)_4\,(4f^2_+)_4)_1$	+	3	2.876	23199.21	2.652	21391.94
$4f^4$	$((4f^4_+)_5)_5$	+	11	2.897	23367.24	2.728	22006.49
$4f^4$	$((4f^1_-)_{5/2}\,(4f^2_+)_6)_9$	−	19	2.929	23624.77	2.728	22007.21
$4f^4$	$((4f^1_-)_{5/2}\,(4f^3_+)_{15/2})_9$	+	19	2.967	23937.13	2.750	22185.03
$4f^4$	$((4f^2_-)_2\,(4f^2_+)_4)_3$	+	7	2.971	23970.13	2.780	22425.68
$4f^4$	$((4f^1_-)_{5/2}\,(4f^2_+)_6)_8$	−	17	3.083	24868.54	2.783	22449.98
$4f^4$	$((4f^2_-)_4\,(4f^2_+)_4)_0$	+	1	3.122	25182.27	2.811	22672.33
$4f^4$	$((4f^2_-)_4\,(4f^2_+)_4)_8$	+	17	3.154	25442.71	2.847	22969.56
$4f^4$	$((4f^3_-)_{3/2}\,(4f^1_+)_{7/2})_2$	+	5	3.190	25730.02	2.873	23175.14
$4f^3\,5d$	$((4f^3_-)_{9/2}\,(5d^1_+)_{5/2})_5$	−	11	3.197	25786.23	2.878	23218.22
$4f^4$	$((4f^1_-)_{5/2}\,(4f^3_+)_{3/2})_1$	+	3	3.218	25957.35	2.925	23591.53
$4f^3\,5d$	$((4f^3_-)_{9/2}\,(5d^1_+)_{5/2})_3$	−	7	3.242	26150.56	2.938	23699.34

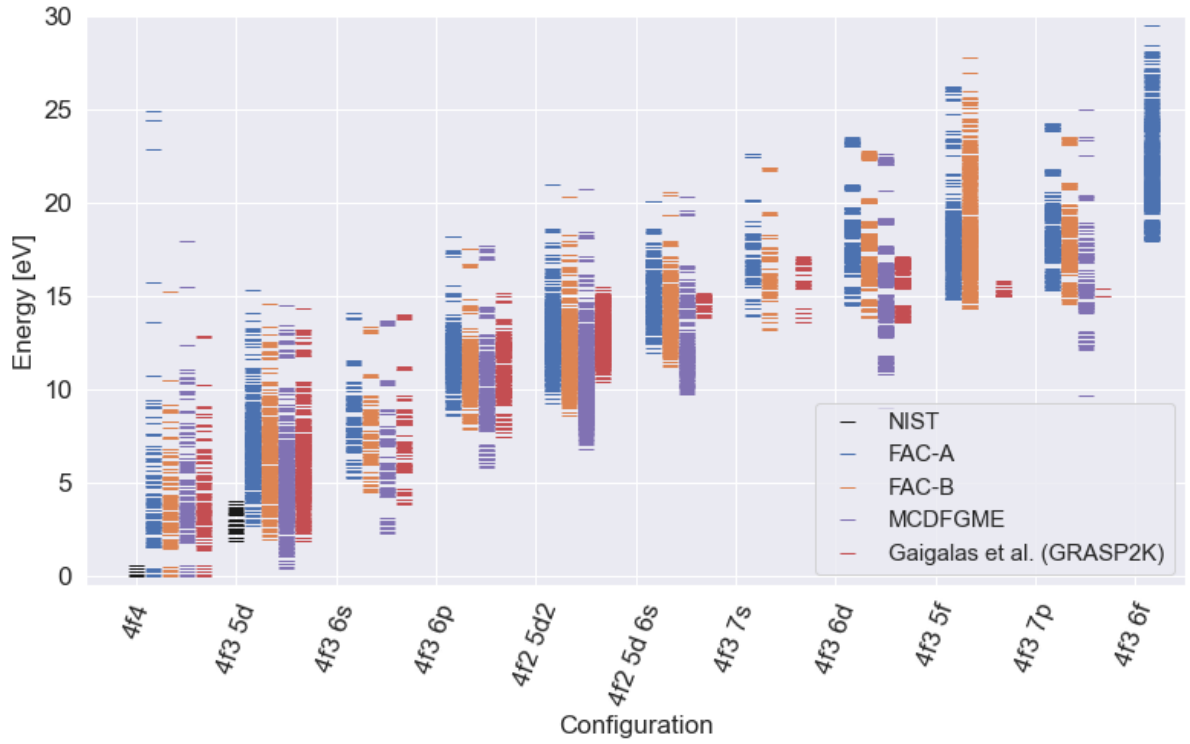

Figure 3.2: Energy levels for configurations of Nd III calculated with FAC and MCDFGME, compared with the results from Gaigalas et al. obtained with the GRASP2K code and with NIST data.

We can clearly see that the FAC results for Calculation B appear to match reasonably well the ones obtained with the GRASP2K code, specially for the lowest lying configurations. A less accurate match is achieved for the $4f^2\,5d^2$ and $4f^2\,5d\,6d$ as FAC seems to underestimate the energies values of those configurations. However, we also note that only data for the ground state and for $4f^3\,5d$ is available in NIST. Not any other database were found for the energy levels of Nd III and hence, no reliable experimental data exists for configurations beyond $4f^3 5d$.

One important point that becomes clear from the FAC results is how sensitive RCI calculations are to the configurations used when the number of configurations included in the basis set is very small. A more precise calculation would require the study of the convergence of the results with the successive inclusion of more configurations in the basis set. In our particular case, the disparity of results from Calculations A and B of FAC alerts for the fact that the energy levels have not yet converged, despite the good results obtained with Calculation B. Hence, although RCI codes can provide a very time efficient calculations when only few configurations are included, which allow for systematic calculations of many ions (as achieved in [2]) one should note that the inclusion of a much higher number of configurations can have a significant impact in the calculation. Moreover, energetic configurations including electrons in a $6f$ shell and beyond, may have a particular high impact in the opacity at high frequencies, as it will be discussed in Section 3.1.6. For all these reasons, we plan to do a more in-depth calculation of Nd III (and of U III) in the future, and assess the impact of the inclusion of different shells in the calculations.

In the case of MCDFGME calculations, the energy levels computed have significantly lower energy than the ones obtained with GRASP2K and FAC. This was to be expected given that neither electron-electron nor core correlations were accounted for in the MCDF self-consistence

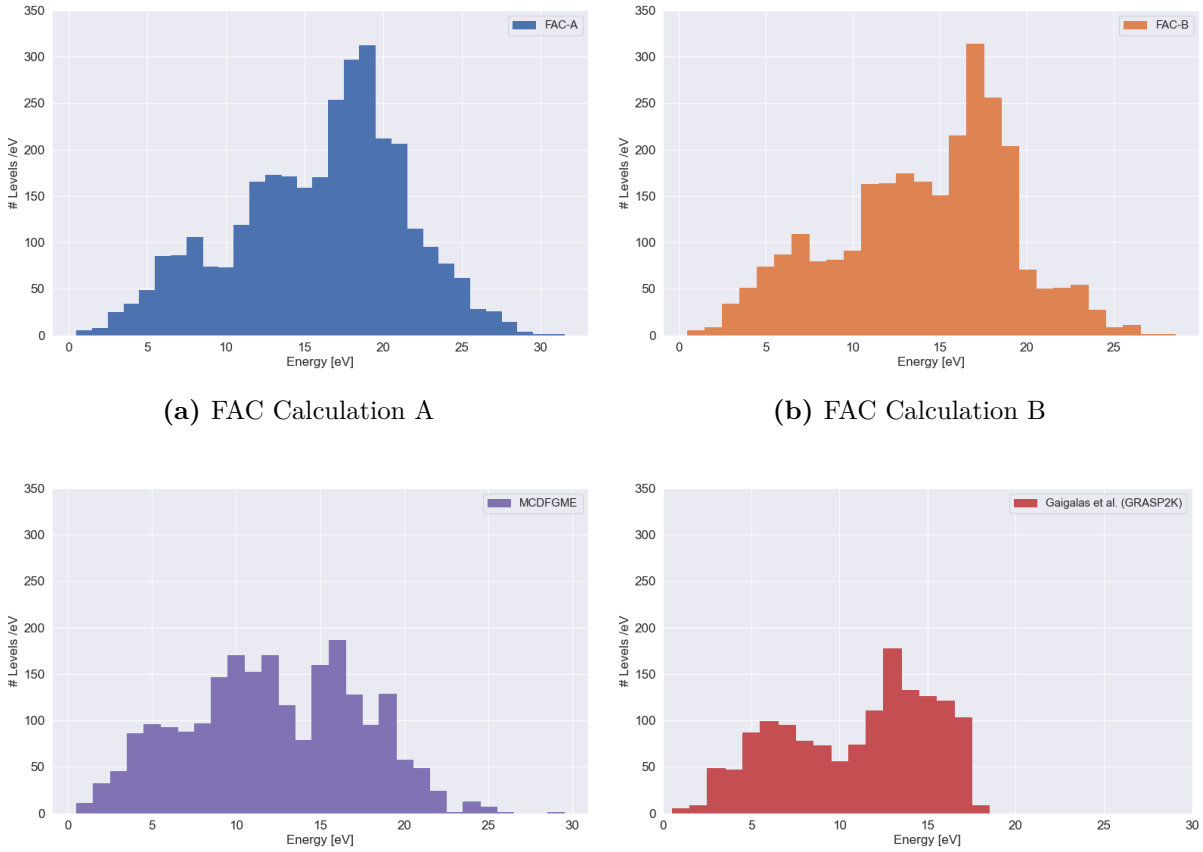

(a) FAC Calculation A

(b) FAC Calculation B

(c) MCDFGME

(d) GRASP2K (Gaigalas et al.)

Figure 3.3: Level density for the two different calculations performed with FAC and MCDFGME, and also performed by Gaigalas et al. with GRASP2K

process. However, one should notice that, for the most excited levels for each configuration, where the impact of the electronic correlations is at its lowest, a reasonable agreement with Calculation B from FAC was reached. The agreement is particularly good for $4f^3\,5d$ and $4f^2\,5d^2$.

3.1.2 Lines and oscillator strengths for NdIII

LTE opacity estimates depend, not only, on the energy level structure of the ions but are also dependent on the oscillator strengths associated between the possible transitions between the levels. In this work, we mainly focused on dipole electric transitions (E1). These so-called "allowed transitions" make up the major contribution of the opacity at the visible, in particular at visible and infrared wavelengths. However, the inclusion of E2 and M1 transitions should also be considered for a complete description. This is specially important for singly ionized rare-earth ions, where many of the low-lying levels have similar parity. Only considering the allowed E1 transitions in this case is not sufficient for a reliable model, as this would allow a lack of lines in the infrared and near-infrared part of the spectra [39]. Although this effect has been shown to affect the doubly-ionized counterparts of lanthanides and actinide elements, it is at a much lower degree however and, therefore, should not have an impact on the particular shape of the spectra.

Table 3.3: Wavelength and gf-values for 45 E1 transitions of Nd III. The states are labeled according to the FAC classification under a jj-coupling scheme. A full description of the notation used in the level classification is given in Section 3.1.1.

Upper Level	Lower Level	Calculation A		Calculation B	
		Wavelength [Å]	gf	Wavelength [Å]	gf
$((4f_-^3)_{9/2}(4f_+^1)_{7/2})_5$	$((4f_-^3)_{9/2}(5d_-^1)_{3/2})_6$	6586.85	5.12635e-04	4742.12	5.14952e-04
$((4f_-^2)_4(4f_+^2)_6)_6$	$((4f_-^3)_{9/2}(5d_-^1)_{3/2})_6$	7089.71	9.17549e-05	4976.13	8.85317e-05
$((4f_-^1)_{5/2}(4f_+^3)_{15/2})_7$	$((4f_-^3)_{9/2}(5d_-^1)_{3/2})_6$	7610.23	1.08729e-05	5203.10	9.92447e-06
$((4f_-^3)_{9/2}(4f_+^1)_{7/2})_4$	$((4f_-^3)_{9/2}(5d_-^1)_{3/2})_5$	5753.89	4.62713e-02	4310.49	4.54245e-02
$((4f_-^3)_{9/2}(4f_+^1)_{7/2})_5$	$((4f_-^3)_{9/2}(5d_-^1)_{3/2})_5$	6159.88	4.61819e-03	4516.72	4.52448e-03
$((4f_-^2)_4(4f_+^2)_6)_6$	$((4f_-^3)_{9/2}(5d_-^1)_{3/2})_5$	6597.49	2.35935e-04	4728.52	2.25520e-04
$((4f_-^2)_4(4f_+^2)_6)_6$	$((4f_-^2)_4(4f_+^1)_{7/2})_{11/2}$	6278.17	6.97646e-04	4562.21	6.87585e-04
$((4f_-^1)_{5/2}(4f_+^3)_{15/2})_7$	$((4f_-^2)_4(4f_+^1)_{7/2})_{11/2}$	6682.95	1.54606e-04	4752.27	1.46919e-04
$((4f_-^1)_{5/2}(4f_+^3)_{15/2})_8$	$((4f_-^2)_4(4f_+^1)_{7/2})_{11/2}$	7064.85	2.73724e-05	4918.52	2.40736e-05
$((4f_-^3)_{9/2}(4f_+^1)_{7/2})_5$	$((4f_-^2)_4(4f_+^1)_{7/2})_{11/2}$	5585.52	5.39831e-02	4200.04	5.28228e-02
$((4f_-^2)_4(4f_+^2)_6)_6$	$((4f_-^2)_4(4f_+^1)_{7/2})_{11/2}$	5942.97	7.22953e-03	4382.58	6.98763e-03
$((4f_-^1)_{5/2}(4f_+^3)_{15/2})_7$	$((4f_-^2)_4(4f_+^1)_{7/2})_{11/2}$	6304.43	4.49451e-04	4557.68	4.19743e-04
$((4f_-^1)_{5/2}(4f_+^3)_{15/2})_5$	$((4f_-^2)_4(4f_+^1)_{7/2})_{11/2}$	21439.46	3.11041e-07	9603.93	5.31843e-07
$((4f_-^3)_{9/2}(4f_+^1)_{7/2})_6$	$((4f_-^2)_4(4f_+^1)_{7/2})_{11/2}$	22054.38	1.26130e-04	9889.24	2.08548e-04
$((4f_-^1)_{5/2}(4f_+^3)_{15/2})_7$	$((4f_-^2)_4(4f_+^1)_{7/2})_{11/2}$	5899.47	1.15339e-04	4342.20	1.05825e-04
$((4f_-^1)_{5/2}(4f_+^3)_{15/2})_8$	$((4f_-^2)_4(4f_+^1)_{7/2})_{11/2}$	6195.10	3.76938e-05	4480.58	3.37839e-05
$((4f_-^3)_{9/2}(4f_+^1)_{7/2})_7$	$((4f_-^2)_4(4f_+^1)_{7/2})_{11/2}$	20963.52	2.10244e-08	9604.78	5.10794e-08
$((4f_+^4)_8)_8$	$((4f_-^2)_4(4f_+^1)_{7/2})_{11/2}$	24860.75	5.94364e-07	10255.84	3.61562e-07
$((4f_-^3)_{9/2}(5d_-^1)_{3/2})_6$	$((4f_-^2)_4(4f_+^2)_4)_7$	24197.77	1.11615e-05	18672.64	5.32891e-07
$((4f_-^2)_4(4f_+^2)_6)_6$	$((4f_-^2)_4(4f_+^1)_{7/2})_{11/2}$	5380.85	6.73868e-02	4069.10	6.54916e-02
$((4f_-^1)_{5/2}(4f_+^3)_{15/2})_7$	$((4f_-^2)_4(4f_+^1)_{7/2})_{11/2}$	5675.47	6.00890e-03	4219.62	5.72248e-03
$((4f_-^1)_{5/2}(4f_+^3)_{15/2})_8$	$((4f_-^2)_4(4f_+^1)_{7/2})_{11/2}$	5948.55	2.20483e-04	4350.18	1.98772e-04
$((4f_-^3)_{9/2}(4f_+^1)_{7/2})_6$	$((4f_-^2)_4(4f_+^1)_{7/2})_{11/2}$	15893.03	5.14218e-07	8424.73	8.86755e-08
$((4f_-^3)_{9/2}(4f_+^1)_{7/2})_7$	$((4f_-^2)_4(4f_+^1)_{7/2})_{11/2}$	18385.05	5.23607e-05	9024.87	8.41816e-05
$((4f_+^4)_8)_8$	$((4f_-^2)_4(4f_+^1)_{7/2})_{11/2}$	21315.53	5.07535e-05	9597.34	6.66135e-05
$((4f_-^3)_{9/2}(5d_-^1)_{3/2})_6$	$((4f_-^1)_{5/2}(4f_+^3)_{15/2})_6$	20645.52	2.33688e-08	8583.36	6.92959e-07
$((4f_-^3)_{9/2}(5d_-^1)_{3/2})_6$	$((4f_+^4)_5)_5$	17607.78	1.53302e-07	9435.64	1.73604e-06
$((4f_-^3)_{9/2}(5d_-^1)_{3/2})_5$	$((4f_+^4)_5)_5$	21612.42	1.33552e-06	4134.26	4.62949e-04
$((4f_-^1)_{5/2}(4f_+^3)_{15/2})_8$	$((4f_-^1)_{5/2}(4f_+^2)_6)_{13/2}$	5552.05	4.57795e-04	8605.78	1.40322e-05
$((4f_+^4)_8)_8$	$((4f_-^1)_{5/2}(4f_+^2)_6)_{13/2}$	16972.29	8.07336e-06	3946.00	8.15943e-02
$((4f_-^1)_{5/2}(4f_+^3)_{15/2})_7$	$((4f_-^1)_{5/2}(4f_+^2)_6)_{13/2}$	5191.30	8.46519e-02	4059.94	2.32216e-03
$((4f_-^1)_{5/2}(4f_+^3)_{15/2})_8$	$((4f_-^1)_{5/2}(4f_+^2)_6)_{13/2}$	5418.84	2.50939e-03	7859.28	9.25200e-06
$((4f_-^3)_{9/2}(4f_+^1)_{7/2})_7$	$((4f_-^1)_{5/2}(4f_+^2)_6)_{13/2}$	14119.28	5.20736e-07	8289.90	1.98868e-05
$((4f_+^4)_8)_8$	$((4f_-^1)_{5/2}(4f_+^2)_6)_{13/2}$	15786.00	1.36057e-05	3443.77	7.38009e-05
$((4f_-^2)_4(4f_+^1)_{7/2})_{11/2}$	$((4f_-^2)_4(4f_+^2)_4)_8$	20750.67	2.21069e-04	3574.15	1.38681e-02
$((4f_-^3)_{9/2}(4f_+^1)_{7/2})_4$	$((4f_-^3)_{9/2}(5d_+^1)_{5/2})_5$	4306.96	1.18367e-04	3705.49	6.71190e-03
$((4f_-^3)_{9/2}(4f_+^1)_{7/2})_5$	$((4f_-^3)_{9/2}(5d_+^1)_{5/2})_5$	4530.46	1.51748e-02	6546.95	1.59650e-03
$((4f_-^2)_4(4f_+^2)_6)_6$	$((4f_-^3)_{9/2}(5d_+^1)_{5/2})_5$	4762.81	7.20786e-03	6857.87	7.17004e-05
$((4f_-^2)_2(4f_+^2)_6)_4$	$((4f_-^3)_{9/2}(5d_+^1)_{5/2})_5$	10407.32	1.77735e-03	7002.13	7.15491e-03
$((4f_-^1)_{5/2}(4f_+^3)_{15/2})_5$	$((4f_-^3)_{9/2}(5d_+^1)_{5/2})_5$	11320.33	7.15782e-05	8207.98	2.10026e-02
$((4f_-^3)_{9/2}(4f_+^1)_{7/2})_6$	$((4f_-^3)_{9/2}(5d_+^1)_{5/2})_5$	11489.48	5.69308e-03	9618.30	1.58838e-03
$((4f_-^4)_4)_4$	$((4f_-^3)_{9/2}(5d_+^1)_{5/2})_5$	14547.20	1.57793e-02	3387.64	1.74943e-02
$((4f_-^2)_4(4f_+^2)_4)_5$	$((4f_-^3)_{9/2}(5d_+^1)_{5/2})_5$	20173.69	1.03360e-03	5946.70	1.33552e-05
$((4f_-^3)_{9/2}(4f_+^1)_{7/2})_4$	$((4f_-^3)_{9/2}(5d_+^1)_{5/2})_3$	4219.52	1.88523e-02	6133.79	6.35647e-05
$((4f_-^2)_4(4f_+^2)_4)_2$	$((4f_-^3)_{9/2}(5d_+^1)_{5/2})_3$	8888.05	8.86343e-06	6311.75	2.04236e-06

Table 3.3 displays the results for the wavelength and gf-values 45 transitions of the two FAC calculations. In Figure 3.4 a plot of the weighted oscillator strengths (gf-values) as a function of wavelength is shown, including comparisons with the GRASP2K data set and the experimental lines available in the DREAM database.

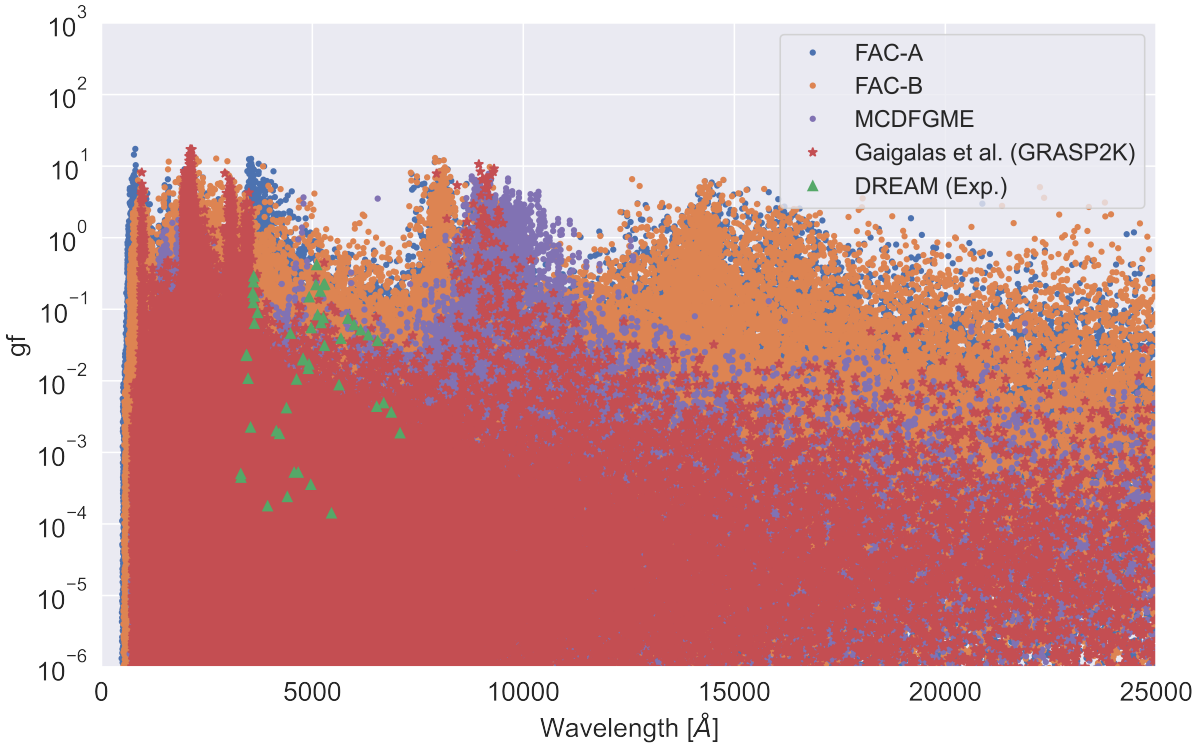

Figure 3.4: Comparison of the results for the oscillator strengths of Nd III, plotted as a function of the wavelength, for the different calculations performed with FAC and MCDFGME and with the results from Gaigalas et al. with the GRASP2K code and experimental lines of the DREAM database.

At first glance, it appears that in this situation, FAC is calculating significantly larger values for oscillator strengths than the generality of the other codes. Unlike when we looked at individual energy levels, the similarity between the results of GRASP2K code and FAC is not as apparent, and the results from MCDFGME appear to provide a better match. However, the number of lines computed by FAC is significantly higher than that of the other codes. As a result, a portion of the gf-values produced by FAC are related to lines for which no data is available.

After carefully analyzing the data, we were able to determine that the cluster of values that arises around $\lambda \sim 15000$ Å is mostly produced by oscillator strengths of transitions between the configurations $4f^3\,6d$ and $4f^3\,7p$. A plot of the weighted oscillator strengths related to the E1 transitions between these two configurations is displayed in Figure 3.5. As predicted by our previous discussion, the number of levels computed by the GRASP2K computation is much lower than in the case of FAC. For instance, for $4f^3\,7p$, just two levels are provided in the paper published by Gaigalas et al. Consequently, and accounting for the fact that a line by line comparison is not viable and potentially not accurate in this case (as discussed in more detail in) Section 2.5) this renders the results produced by both codes incomparable.

The oscillator strengths from MCDFGME for this $6d \rightarrow 7p$ transition do appear to reproduce better the GRASP2K data for this same transitions. As it was previously stated, the

calculations from MCDFGME do not take into consideration correlation effects, so the results are less accurate than any of the other calculations considered in this discussion. However, from Equations (2.52), (2.56) and (2.57) we see that f-values only directly depend on the energy difference between two levels and not on the specific energy of the levels. Furthermore, we notice that the difference between the energy of the ground levels of both configurations is roughly the same. In particular, for GRASP2K the energy difference of the ground levels of the $4f^3\,6d$ and $4f^3\,7p$is $\Delta E^{6d\rightarrow 7p}_{\mathrm{GRASP2K}}$=1.38 eV while for MCDFGME is of $\Delta E^{6d\rightarrow 7p}_{\mathrm{MCDFGME}}$=1.31 eV. For this reason we believe that a comparison between the results of MCDFGME and of GRASP2K is legitimate despite the energy differences we find when comparing the energy levels directly.

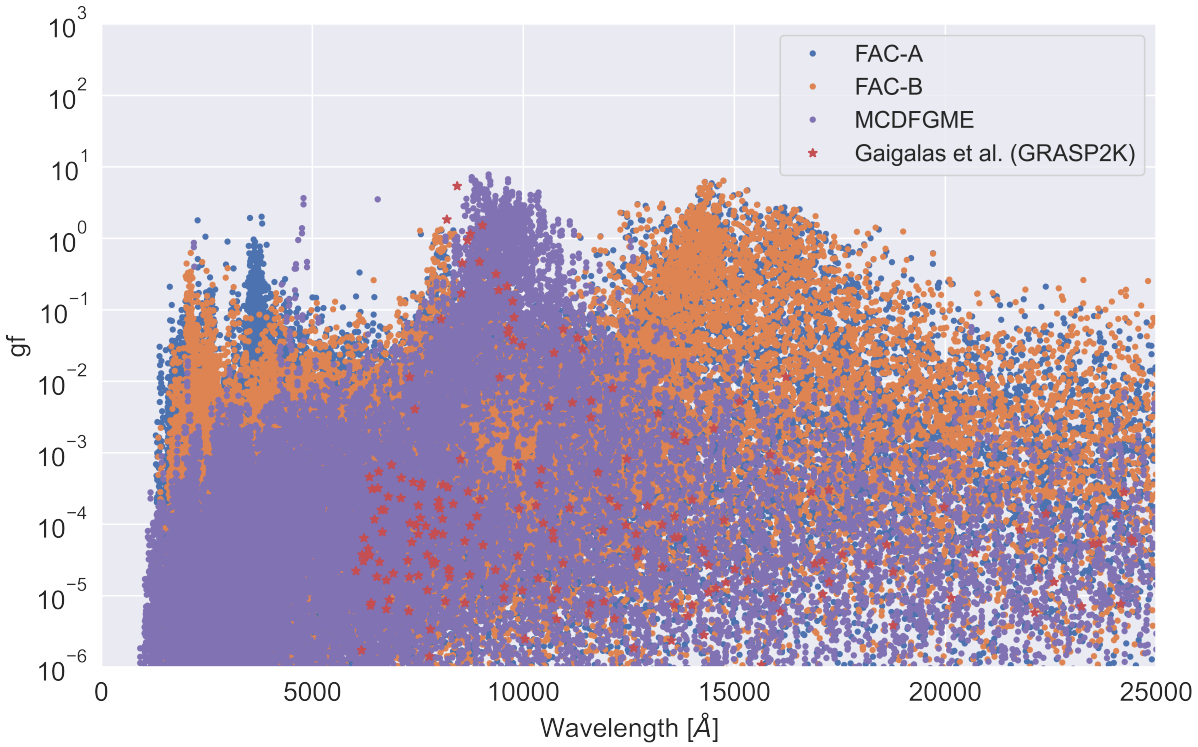

Figure 3.5: Comparison of the results of the different calculations for the oscillator strengths of Nd III, plotted as a function of the wavelength, for all the transitions that occur between the $4f^3\,6d$ and the $4f^3\,7p$.

It is worth noting that some convergence problems were found for some levels computed with MCDFGME. In any case, and given the previously stated assumptions, we notice that we still obtain larger gf-values for both FAC calculations that are not replicated by the MCDFGME calculation. Furthermore, for $\lambda > 5000$ Å, the general pattern of oscillator strengths found with GRASP2K appears to resemble the one obtained with MCDFGME.

Taken together, this analysis shows that, regardless of the reduced number of lines computed in GRASP2K for the $6d \rightarrow 7p$ transition, the MCDFGME calculations do replicate the calculations from Gaigalas et al. more accurately than the FAC ones. Although there can be some contribution of lines that did not converge in the MCDFGME calculation to explain part of the FAC values, it would not be enough to explain the total number of lines with $gf > 10^{-1}$, in particular in IR at $\lambda \sim 15000$ Å and in UV part of the spectrum. Furthermore, the energy difference between the ground states of this transition for FAC is lower when compared with the results of both MCDFGME and GRASP2K, as $\Delta E^{6d\rightarrow 7p}_{\mathrm{FAC}}$=0.78 eV.

For this reason, one must assume that, in the worst-case scenario, FAC is overestimating

the oscillator strengths for $6d \rightarrow 7p$ transition. Therefore, we must proceed with care with the opacity calculations. In the next section, we investigate how the gf-values actually impact the expansion opacities.

3.1.3 Contribution of lines to the opacity

Since the previous analysis was not fully conclusive on the accuracy of the FAC calculations regarding the oscillator strengths and the gf-values, it becomes natural to look into how differences in these values can affect the final opacity calculations. As we are only focused on the timescales of $t_{ej} \lesssim 1$ day, the optical depth can be calculated under an LTE approximation. From Equation (2.13) we have that

$$\tau_k = \left(\frac{\pi e^2}{m_e c}\right)\left(\frac{n t_{exp}}{g_0}\right)\lambda_k g_k f_k e^{-E_k/k_B T} = \left(\frac{\pi e^2}{m_e c}\right)\left(\frac{n t_{exp}}{g_0}\right)\Gamma_k. \tag{3.1}$$

Here, we can clearly see that the variation of τ for a specific ion in the ejecta is all contained in the new defined variable Γ. Moreover, Γ only depends on atomic parameters - the wavelength of the transition λ_k, the weighted absorption oscillator strength $g_k f_k \equiv (gf)_k$ and the energy of the lower level of the transition E_k. This implies that a specific line will have a bigger impact on the shape of the ejecta the greater Γ is.

In the line of study of kilonovae opacities, we define a line to be "strong" if it has a significant contribution to the expansion opacities of the ejecta. In practice, this means that the probability of photons being absorbed by those transitions is high enough to be relevant to the final spectrum. Previously published work [3, 67, 70] has estimated the effective line strength contribution or line strength of the transition just by taking the gf-values weighted by the Boltzmann factor, i.e., $gfe^{-E_k/k_B T}$. In this work we propose the use of $\Gamma(\lambda)$ as a more solid quantity to quantify the line strength. There are two main arguments for this particular choice. Firstly, Γ takes into account the full range of atomic parameters relevant to the description of the opacities under the LTE approximation. For that reason, it can be used to compare the effective atomic contribution of different ions to the opacity. Furthermore, any threshold used to distinguish between a "strong" and a "weak" transition will be wavelength independent, in contrast to the case where the wavelength is not considered in the definition.

In the particular case of this work, we are considering strong lines with $\Gamma_k > 10^{-10}$ cm. This is comparable to the more usual definition of $gf \exp(-E_k/k_B T) > 10^{-5}$ in the visible region, and corresponds to an optical depth of $\tau_k \gtrsim 1$ for both lanthanides and actinides. Nevertheless, this threshold is just used as a visual cue for facilitating the comparison between different results, as all the lines calculated were used for the opacity calculations. In any case, a solid definition of line strength is important because using a whole set of lines becomes problematic as the complexity of kilonovae models increases and more ions are needed for a more complete description. f-block elements are of particular importance due to their large number of lines. This issue becomes even more critical as we approach the far infrared and radio wavelengths. Nevertheless, even in the NIR region the number of strong lines considered, depending on the definition used and the threshold defined can differ, for nearly one order of magnitude, as it will be seen in Section 3.2.2 when we examine calculations for U III.

From the point of view of the atomic calculations, this definition is also important as it can be used as estimator to investigate and quantify the impact of the inclusion of more energetic configuration in the basis set of the RCI or MCDF calculations. Moreover, the number of strong

lines can be used to compare the impact of different ions and/or of different calculations on the opacity spectra, without the need of performing simulations for specific models.

Although $\Gamma_k(\lambda)$ depends on an equilibrium level population distribution, the features of this function for comparing the atomic contribution of a single ion to the opacities should still hold even at lower temperatures. Most ions in the media will deexcite and remain at lower energy levels as the medium expands and freezes with time. At most, the level density distribution will be sharper than the Boltzmann factor's expected exponential distribution. Here, collisional and photoionization rates are crucial in determining the precise level distribution.

3.1.4 $\Gamma(\lambda)$ for Nd III

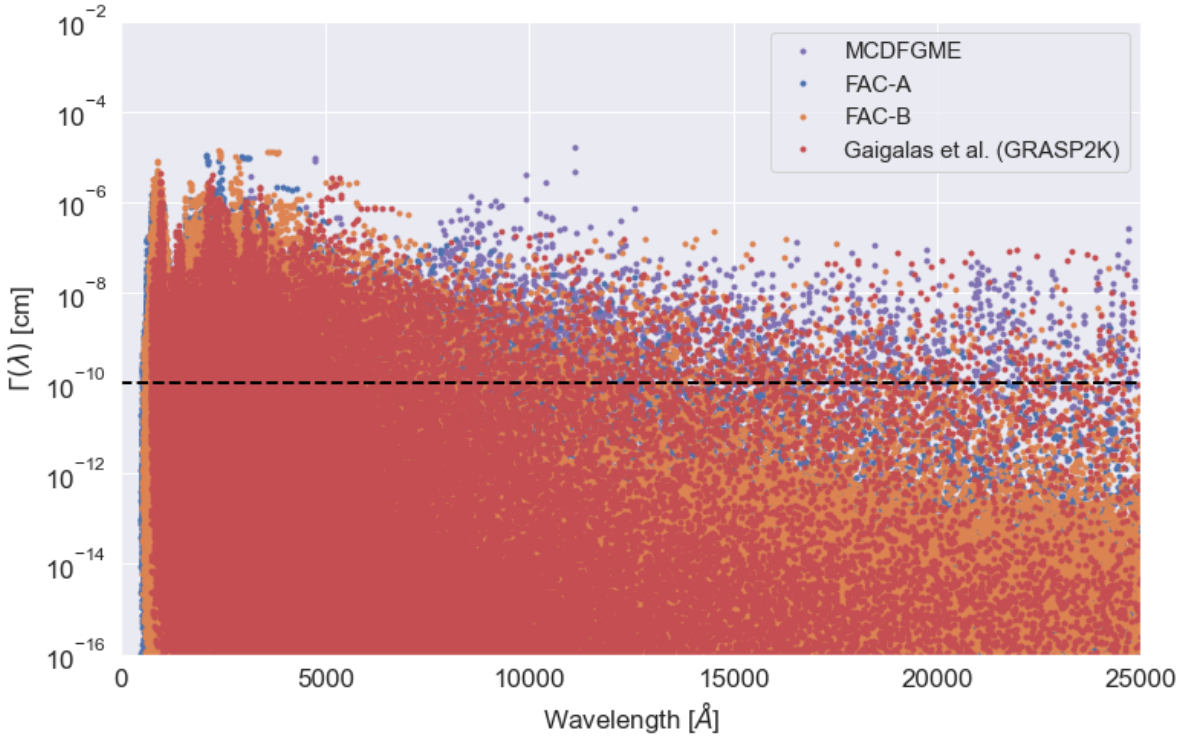

Figure 3.6: Plot of $\Gamma(\lambda)$, with $T = 10000$ K for the results obtained by the different FAC calculations and MCDFGME and comparison with the results of GRASP2K for Nd III.

A plot of Γ as a function of the wavelength, for Nd III is shown in Figure 3.6. Based on previous work for doubly ionized ions [2, 3, 67], and in order to facilitate comparisons, a temperature of $T = 10000$ K is used. Here we see that the picture is very different from when we were considering the gf-values. To begin with, we can see that the evolution of this quantity with wavelength is consistent across all codes, appearing to decay as transitions become less energetic. This is explained by the dependency of $\Gamma_k(\lambda)$ on the exponential Boltzmann factor, which in turn is only dependent on the energy of the transition's lowest level. As a result of their higher occupancy density in equilibrium, lower energy states have a bigger contribution to the opacity.

Looking at the level distribution in Figure 3.3 we find that the density of levels is larger for excitation energies between $E_k \sim 10$ and $E_k \sim 20$ eV. This explains why $\Gamma_k(\lambda)$ is higher in the visible and UV part of the spectrum, as most transitions to lower energies levels will be

conducted at lower wavelengths. On the other hand, despite the very high density of levels of neodymium, the density of low-lying levels (with $E < 5$ eV) is particularly low. This implies that infrared transitions, although accounting for the vast majority of transitions, have a much lower impact on the opacities. In fact, after 10000 Å, only a few transitions are found with $\Gamma_k \gtrsim 10^{-10}$ cm. For $\Gamma_k < 10^{-10}$ cm, $\tau < 1$, the contribution of such transitions to the opacity calculations is highly suppressed.

Taking into considering the strengths of the lines and their contribution to the optical depth, we can now safely conclude that any overestimation of the FAC values for the $6d \rightarrow 7p$ transition, as discussed in Section 3.1.2 won't have any measurable impact in the final opacity spectra. As it can be seen from fig. 3.7 all E1 transitions between both configurations have $\Gamma_k < 10^{-10}$ cm, except for the results obtained with MCDFGME. Due to the lack of electronic correlations in the MCDFGME calculation, and consequent underestimation of the energy levels, we do expect Γ_k to be overestimated for this particular calculation. Thus, we can confidently conclude, from the low values of Γ_k, that the impact of $6d \rightarrow 7p$ transitions will be negligible and, therefore, any overestimation of the gf-values in the FAC calculation won't affect the final spectra.

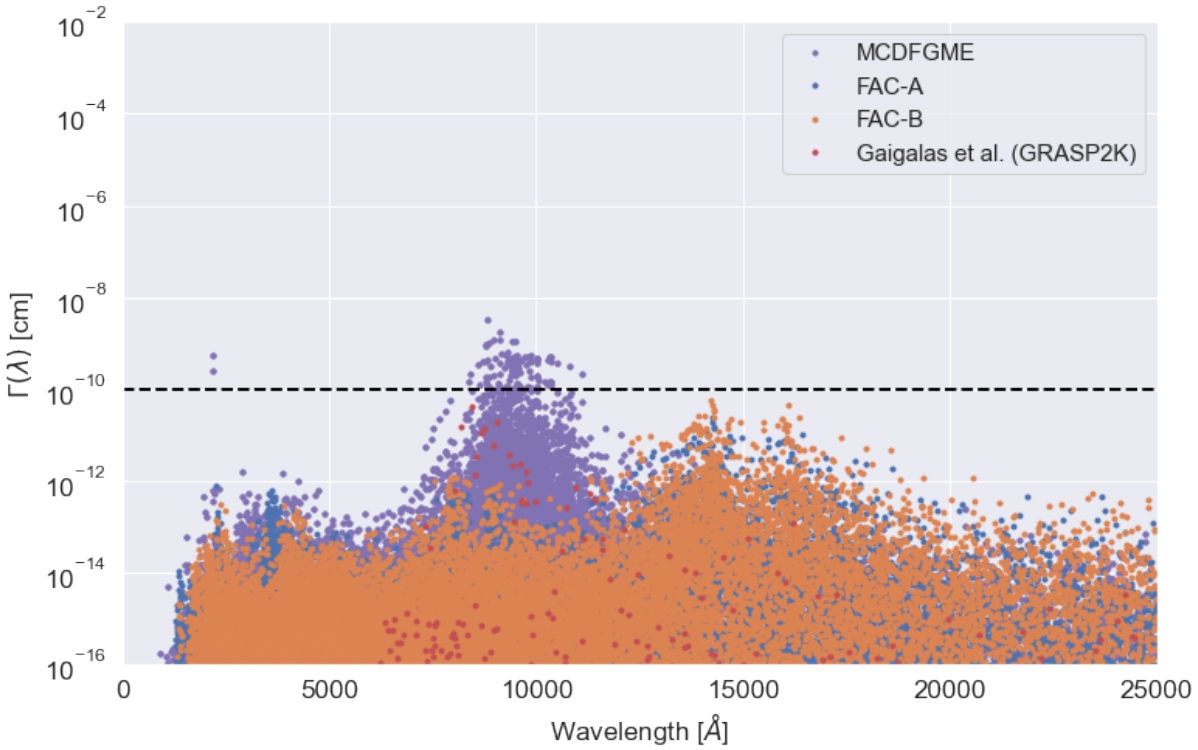

Figure 3.7: Plot of $\Gamma(\lambda)$, with $T = 10000$ K, or the results obtained by the different FAC calculations and MCDFGME and comparison with the results of GRASP2K for the $6d \rightarrow 7p$ transition of Nd III.

The impact of the results obtained for the different codes on the opacities calculations can be measured by looking at the number of strong lines. The total number of strong transitions (fulfilling $\Gamma_k > 10^{-10}$ cm at $T = 10000$ K) for 3 main wavelength ranges is shown in Table 3.4 while a plot of the dependence of the number of strong lines with the wavelength is shown in Figure 3.8.

As predicted, the number of strong lines greater is in the UV and visible regions of the spectrum for FAC's and GRASP2K calculations due to the higher contribution of low-lying levels to Γ_k. For the case of the MCDFGME calculation, as the energy of the levels are underestimated

Figure 3.8: Number of strong transitions for Nd III as a function of the wavelength obtained with both FAC calculations and with the MCDFGME calculations compared with the results of GRASP2K of Gaigalas et al.

due to the lack of correlations, we see an increase of the number of strong IR transitions when compared to the other results, also associated with a very low number of strong lines in the UV. Moreover, we see the effect of the inclusion of the $4f^3 6f$ configuration in Calculation A of FAC when compared with Calculation B. The upwards shift of the energy levels induced by the inclusion of a $6f$ shell in the basis set increases, in general, the energy of the transitions, reducing the number of strong lines in the IR and visible regions while increasing that number in the UV.

3.1.5 Ionic density population of Nd III

The accuracy of the opacity calculations, not only relies on the accurate calculation of atomic parameters described in the previous sections, but also depends on the mass fraction of that element present in the ejecta. Thereby comparing the results of simulations with the observed spectra from different events, we can directly infer the presence of different species in the plasma and correct the current models.

The determination of the ionic density in the plasma is, however, also dependent atomic properties of the elements under consideration. In particular, in LTE, ionic balance is established and can be calculated by means of the Saha equation given in Equation (2.21), which depends on the ionization potential energies χ_{N-1} on the partition functions U_N. Although the ionization energies are usually easy to calculate or even measured experimentally for specific ions, the partitions functions involve a weighted sum over all the energy levels of that ion. While the contribution of high-lying levels is usually negligible, as their weight to the sum decreases exponentially, an accurate and extensive knowledge of the energy of low-lying levels is required to ensure the accurate calculation of the partitions functions and,

Table 3.4: Number of strong lines computed for the 4 calculations under analysis, FAC-A, FAC-B, MCDFGME and GRASP2K, for 3 wavelength ranges: UV (0 - 4000 Å), Visible (4000 - 8000 Å) and IR (8000 - 25000 Å)

Code	Number of lines		
	UV (0-4000) Å	Visible (4000-8000) Å	IR (8000 - 25000) Å
FAC-A	75724	2049	375
FAC-B	67878	3008	924
MCDFGME	1620	1686	2162
GRASP2K	26537	2423	1234

consequently, of the density of ions present in the medium.

The impact on the ionic density calculations from the lack of extensive atomic data can be seen in Figure 3.9 where the ionization-stage fraction (z) for a pure Nd gas is plotted using the available data from NIST. We note that for a pure gas of an element X, the number density is simply given by

$$n_X = \frac{N_A}{M_X}\rho \tag{3.2}$$

where $N_A = 6.02214076 \times 10^{23}$ mol $^{-1}$ is the Avogadro constant, M_X is the molar mass of the element X and ρ is the mass density of the gas. According to the NIST estimates of the partition functions, virtually no Nd III is found at $T = 10000$ K, accounting for an ionization fraction $z_{\mathrm{NdIII}} = n_{\mathrm{NdIII}}/n_{\mathrm{Nd}} \approx 10^{-5}$. However, when larger datasets are used, ionization fractions of the order of $z_{\mathrm{NdIII}} \approx 0.01$ at $T = 10000$ K are predicted [72].

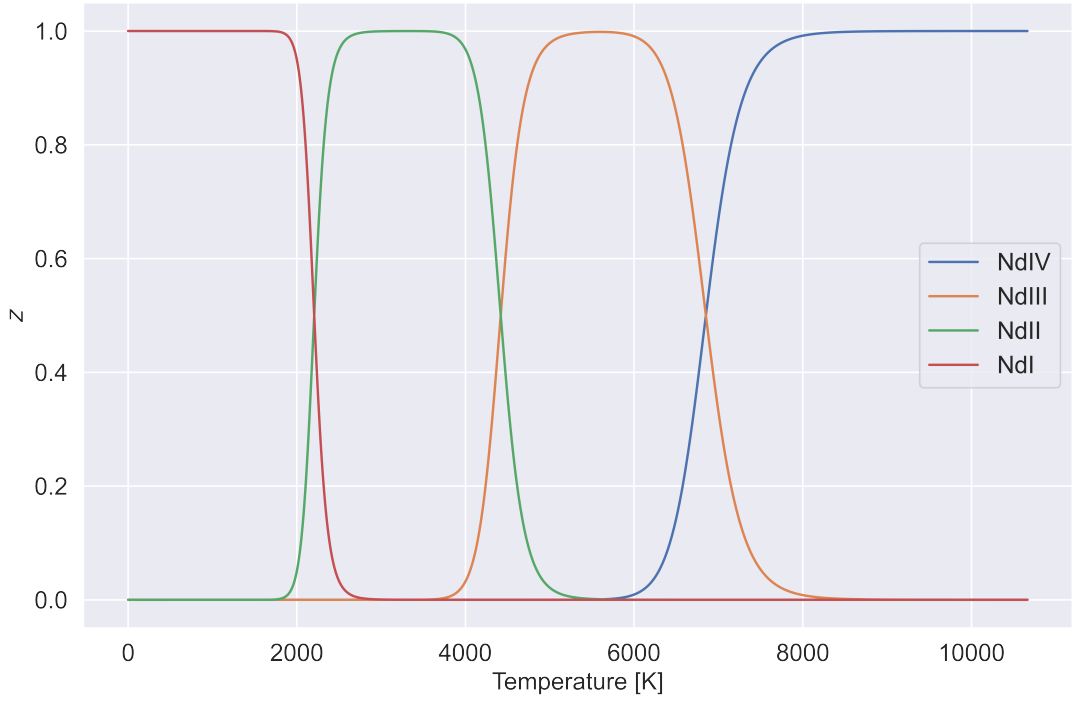

Figure 3.9: Ionization-stage fraction (z) for a pure neodymium gas for a density $\rho = 1 \times 10^{-13}$ based on the atomic data for Nd I - IV found in NIST.

During the time period of this work, we only produced and analyzed data for doubly ionized

neodymium. For that reason, no reliable calculations of the partitions functions were produced. Nevertheless, we noticed that the opacity calculations for Nd III computed by Gaigalas and co-workers was better reproduced by using $z_{\mathrm{NdIII}} \approx 0.01$. Considering that the Gaigalas et al. calculations are one of the most relevant ones regarding lanthanides and that an extensive comparison between the results from this work and their data for Nd III is performed in this work, we decided to use an ionization fraction $z(T = 10000\ \mathrm{K})_{\mathrm{NdIII}} = 0.01$ for the opacity calculations presented. We are working on atomic calculations for the neutral Nd and for the singly and triply ionized species to be able to provide a full computation of the ionic density populations of this ion until temperatures of $T \sim 15000$ K.

3.1.6 Opacity of Nd III

The preceding discussion concerning the precision of the various codes may be easily extended to the opacities. The expansion opacity was calculated using the LTE approximation over a time period of one day following the explosion, when the medium density is about $\rho = 10^{-13}$ cm^{-3} [33]. Additionally, a temperature of $T = 10000$ K was specified based on prior estimates for doubly ionized ions [2, 70]. The ionic density population of $z_{\mathrm{NdIII}} = 0.01$ was used based on the discussion on Section 2.2. The results are shown in Figure 3.10.

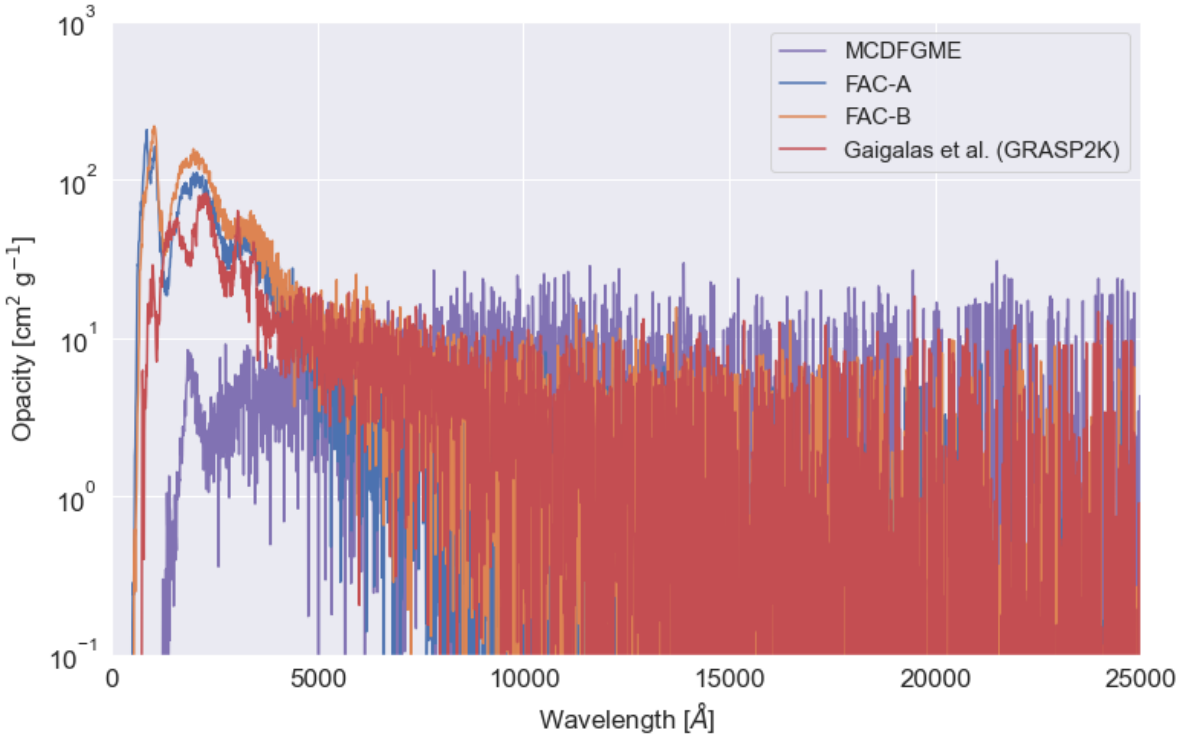

Figure 3.10: Expansion opacity calculations for all the calculations done with FAC and MCDFGME and comparison with the results from Gaigalas et al. with GRAPS2K. The opacity was evaluated at $t = 1$ day for the typical density and temperature values of $\rho = 10^{-13}$ cm^{-3}and $T = 10000$ K assumed by other calculations.

Two clearly distinct regions can be immediately identified in the plot based on overall the convergence of the codes on the behavior of the curves: A UV/Visible region with $\lambda \lesssim 7000$ Å, where less agreement is found between calculations; and an infrared region with $\lambda \gtrsim 7000$ Å, where we notice a general decrease in the opacity, with far greater agreement between calculations.

In the lower wavelength region we find not only a discrepancy in the absolute value of the opacities (with the highest opacity output provided by the FAC calculation) but also differences in the structure of the curves. We notice that even when using the same code, in this case FAC, the position of the first peak in the high-UV region does not match between Calculations A and B. This may be explained by the increased energy difference between the excited and ground states as a result of the $4f^3\,6f$ configuration being included in the Calculation A. Additionally, while the position of the first peak in the GRASP2K calculation appears to be similar to that in FAC Calculation B, the shape of the curve at $\lambda \sim 2000$ Å is completely different with two bumps instead of one. Finally, as predicted from prior considerations, particularly the number of strong lines in the UV region, the MCDFGME calculation's output opacity is significantly lower than the output of the other calculations. These discrepancies demonstrate that the calculations in this region are highly dependent not only on the number of lines calculated, but also on the set of configurations used in the calculation.

This higher sensitivity of the opacity curve in the UV/visible region, although it forces further optimization of the calculations in order to provide accurate results and comparisons to experiment, it can also be seen as advantageous since certain spectral features, characteristic of different ions, could, in principle, be seen in the and studied in this region. This requires great precision on energies for low-lying levels, as they are the ones that most contribute to a line's strength but, but in particular, it requires great accuracy on the wavelength of the transitions that may induce these features. Identification of these transitions is, therefore, of utmost importance in order to reduce the number of calculations needed, and consequently computation time required in the study of such spectral features.

On the other hand, in the IR range, we observe that the calculations agree far better than they do in the ultraviolet and visible range. Indeed, the curve appears to behave consistently throughout all calculations, with MCDFGME outputs having greater values than those from the other codes. This is not surprising, as the number of strong transitions in this region for MCDFGME is greater than any of the other codes. Nevertheless, we can see the effect of a lower number of transitions with $\Gamma \sim 10^{-10}$ cm. Even though the number computed by FAC (in both approaches) is largely superior to the number used in the Gaigalas et al. calculation, the actual number of lines that actively contribute to the opacity is similar, as could be estimated by the number of strong displayed in Table 3.4.

Contrary to what occurs in the UV areas, the IR region is significantly less sensitive to the quality or the amount of computed lines. Additionally, we can observe that the dispersion of values is considerably greater in the higher wavelength region than in the lower wavelength zone. As $\tau \sim 0$ for small Γ_k, we have that $1 - e^{\tau} \approx \tau$ and hence

$$\kappa_{\text{exp}} \approx \frac{1}{\rho c t_{exp}} \sum_k \frac{\lambda_k}{\Delta\lambda} \tau_k \sim \Gamma_k. \tag{3.3}$$

This implies that when the optical depth decreases, the linear dependency of the opacities on Γ_k rises. This large fluctuation in opacity with wavelength is thus associated with the large dispersion of points we find for the gf-values and, consequently for Γ_k as seen in Figure 3.4 and Figure 3.6.

In any case, the employment of extremely precise, but computationally expensive, atomic codes in this region may be superfluous as no spectral features seem to be noticeable in this region. Calculations with RCI codes, even without the most appropriate basis set, can yield

results comparable to theoretically more accurate codes like GRASP2K and a systematic calculation for a large number of lanthanides and actinides ions might be accomplished considerably more quickly.

3.1.7 Impact of the choice of the active space in the calculations

Considering that one of the objectives of this study is to offer an assessment of the performance of various methods, it is critical to examine this scenario in which RCI calculations outperform MCDF calculations in terms of accuracy. The sole difference between the active space of configurations utilized in Strategies C and C with $5s$ and $5p$ in the Gaigalas et al. calculations with GRASP2K [3] is that the latter case includes $5s$ and $5p$ orbitals. While for Strategy C energy levels are computed using MCDF calculations followed by RCI calculations which include the Breit interactions and QED corrections, Strategy C with $5s$ and $5p$ uses the wave functions computed in Strategy C in a full RCI calculation with the addition of configurations in the basis set, including the $5s$ and the $5p$ shells. Despite the latter calculation performing a full RCI calculation, the addition of the $5s$ and the $5p$ shells in the configuration space dramatically changed their results.

As demonstrated by Cowan et al. in [66], the collapse of the $4f$ radial function occurs considerably more rapidly than that of other orbitals. As a result, the radii of the $4f$ orbital is extremely small, making the orbital even tighter and closer to the core than the orbitals of $5s$ and $5p$. For that reason $4f$ orbitals have comparable (and even lower) energies to $5s$ and $5p$. As such, it is critical to include those shells in the active space in order to ensure an accurate description. This, however, would make MCDF computations unreasonably expensive. What this is actually showing is that the inclusion of these orbitals to the active space has a greater effect on the calculations than the individual optimization performed by MCDF techniques. RCI techniques can thus offer a more accurate description of the system at a significantly reduced computational cost, if the active space is selected appropriately.

These same general considerations should hold when considering actinides. It is worth noting, that $5f$ orbitals extend further from the core and are more diffuse than $4f$ orbitals. As a result, the $6s$ and $6p$ orbitals are unlikely to have as much influence on the calculations as they do in the case of lanthanides. In this case, due to the larger $5f$ radii, interactions with $7s$ and $7p$ orbitals tends to be stronger. On the other hand, $5f$ electrons are less bound to the core than in the case of $4f$ electrons, which cause many more actinides to have a d or an s electron in the ground configuration [73].

3.2 Calculations on U III

While lanthanide should account for the majority of f-shell elements produced in kilonovae via the r-process, the contribution of actinides to the ejecta's opacity cannot be overlooked. Indeed, their properties are very similar to those of lanthanides, having a similar shell structure with all principal quantum numbers increased by one. Therefore, most of the conclusions discussed previously will also apply for actinides. The main difference lies in the higher radius of the $5f$ shell when compared to the $4f$. Therefore, $5f$ electrons tend to be less deeply buried in the core and less shielded from the effect of outer valence electrons than $4f$ electrons. This effect associated to the higher Z of actinide elements can, in theory, contribute to a smaller gap

between the ground state and the first few excited levels. Hence, we expect a higher density of levels closer to the core, which may have a sizable impact in the opacities of those ions.

The narrow radii of the $4f$ orbitals of lanthanides lead the $4f$ electrons to be extremely close together, resulting in significant mutual Coulomb repulsions. This impact is mitigated by the larger dispersion of the $5f$ orbitals in actinides. On the other hand, spin-orbits interactions increase because of the higher Z, which increase the impact of relativistic corrections.

In addition, it is worth mentioning that the vast majority of actinide elements (as all the elements past uranium in the periodic table) do not have any stable isotopes. As a result, the overall mass fraction of actinides in the kilonovae ejecta is expected to me lower than of lanthanides [74]. Nevertheless, it is important to remember that even these radioactive species have isotopes with half-lives of hours or even days, and thus, the opacity contribution of these elements on such timescales cannot be disregarded.

For all of these reasons, and based on our prior Nd III results, we opted to proceed with an FAC calculation for doubly-ionized uranium. The choice of this ion is self-explanatory, as it is the actinide with the most comparable shell structure to Nd III. In this way, we can compare these two ions directly and, hopefully, draw conclusions that can be applied to the rest of the elements in the f-block. Furthermore, uranium is one of the most researched actinides and one of the few for which structure calculations in weakly ionized species have been performed.

At the time of writing, the only experimental data available for actinide ions is from Blaise et al. from 1992 [75]. Furthermore, two independent groups from the *Los Alamos* institute have developed calculations for the first ionized states of Uranium using the CI-MBPT [76] and the ATOMIC codes [77]. Only the data from Savukov et al. [5], who used a many body perturbation theory approach, is publicly available. Finally, Sultana N. Nahar of the Ohio State University's Astronomy Department hosts and maintains the NORAD-Atomic-Data database [78], which contains calculations for a broad range of structure calculations for important astrophysical ions, including uranium, using the SUPERSTRUCTURE [79] algorithm. In that database, however, only highly ionized elements are available.

3.2.1 Energy Levels

Based on the similarities between the shell structure of NdIII and UIII, as an initial approach to the calculations, the basis set for the FAC RCI calculations was determined by raising the principal quantum number n of the configurations used in the Nd III by one. The configuration set of Calculation B of Nd III was chosen since that calculation produced the best results when compared to the experimental NIST data.

Table 3.5 provides an overview of the FAC calculation achieved in the work as well as the prior calculations for U III with the CI-MBPT code from Savukov et al. and of the experimental data from Blaise et al. The first 45 energy levels calculated with FAC are shown in Table 3.6.

Although the name of the code used by Savukov et al. suggests the use of a variation of a MBPT approach, the vast majority of the results published in [5], and that are used for comparison in this work were performed using a hybrid configuration interaction (CI) plus linearized coupled cluster (LCC) methods described in [6]. Despite having calculated a total of 192 levels and 3024 transitions, only the energies of 96 levels and the gf-values of 20 lines are published. For the case of the experimental data provided by Blaise et al. only the data from 123 identified levels is available.

Table 3.5: Summary of the different set of configurations use on the FAC calculation for U III. An overview of the experimental data from Blaise et al. [75] and the calculations produced by Savukov et al. [5] using a hybrid configuration interaction (CI) plus linearized coupled cluster (LCC) methods, described in [6], also shown. For the CI+LCC calculations, we only show the configurations for which levels and lines data was published.

Label	Configurations		All	
	Even	Odd	#Levels	#Lines
FAC	$5f^4$, $5f^3\,7p$, $5f^2\,6d^2$ $5f^2\,6d\,7s$, $5f^3\,6f$ $5f^3\,8p$	$5f^3\,6d$, $5f^3\,7s$, $5f^3\,7d$ $5f^3\,8s$	2702	542264
CI+LCC - Savukov et al.	$5f^4$, $5f^2 6d^{2a}$	$5f^3\,6d$, $5f^3\,7s^a$	192[b]	3024[c]
Exp. - Blaise et al.	$5f^4$, $5f^3 7p$, $5f^2 6\,d^2$ $5f^2\,6d\,7s$	$5f^3\,6d$, $5f^3\,7s$	123	-

[a] Only configurations for published levels and lines are shown.
[b] Only the energies for 96 levels are published.
[c] Only the gf-values for 20 lines are published.

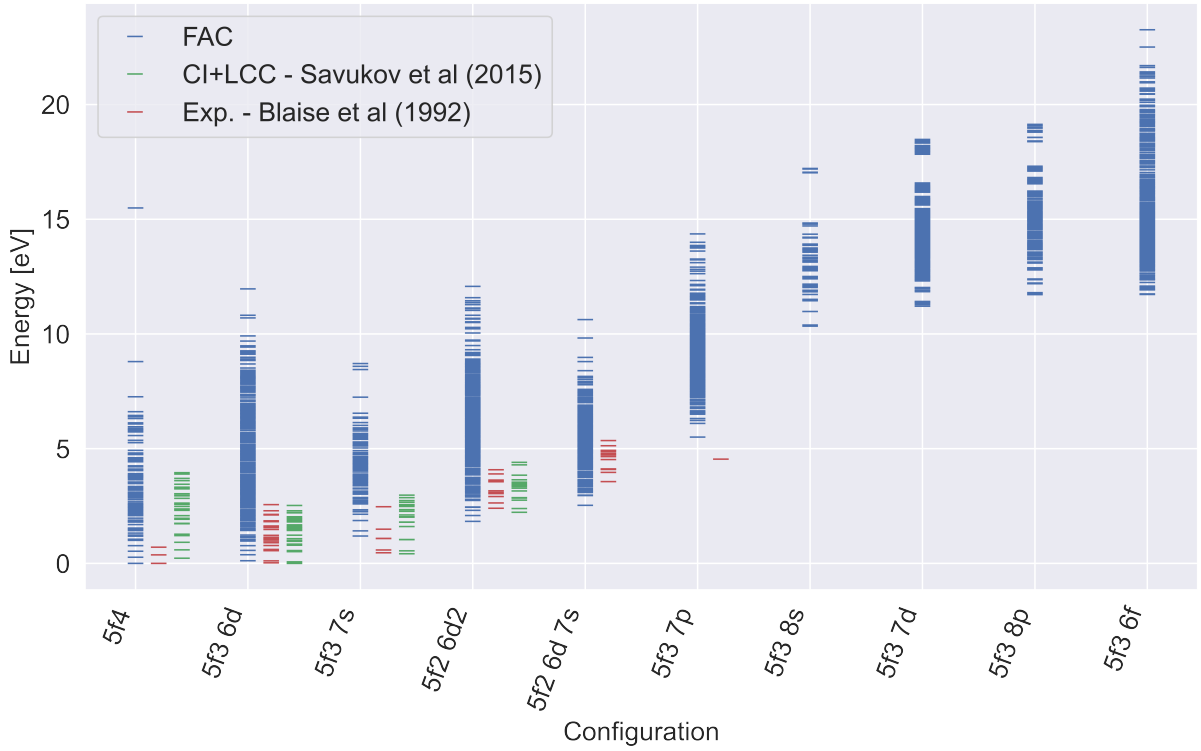

Figure 3.11: Energy levels for configurations of U III calculated with FAC. The excitation energies are compared with the experimental results from Blaise et al. [75] and the CI-MBPT from Savukov et al. [5].

We can observe from Figure 3.11 that, as with Nd III, we were able to reproduce the lowest lying levels fairly accurately when compared to both experimental and computational data.

From spectroscopic studies, Blaise et al. determined $5f^4$ to be the ground configuration for U III. On the other hand, the CI+LCC calculations suggest an electron in the $6d$ shell in the ion's lowest energy state. Our FAC calculations do provide better agreement with the experimental data when it comes to the ground state and give the even $5f^4$ configuration has the ground state of U III. This disparity between calculations, however, is not surprising given the high diffuseness of the $5f$ shell, which makes the excitation energies of $5f$ and $6d$ exceedingly close

Table 3.6: First 45 energy levels for U III calculated using FAC for the approaches used in this work (Calculation A and Calculation B) and described in the text. The states are labeled according to the FAC classification under a jj-coupling scheme. A full description of the notation used in the level classification is given in Section 3.1.1. The parity (P) of each level and its statistical weight $g = 2J + 1$ are also shown.

Configuration	Level	P	g	Energy [eV]	Energy[cm^{-1}]
$5f^4$	$((5f_-^4)_4)_4$	+	9	0.000	0.00
$5f^3\,6d$	$((5f_-^3)_{9/2}\,(6d_-^1)_{3/2})_{11/2}$	−	13	0.131	1059.29
$5f^4$	$((5f_-^3)_{9/2}\,(5f_+^1)_{7/2})_5$	+	11	0.254	2050.96
$5f^3\,6d$	$((5f_-^3)_{9/2}\,(6d_-^1)_{3/2})_5$	−	11	0.362	2927.57
$5f^4$	$((5f_-^2)_4\,(5f_+^2)_6)_6$	+	13	0.451	3638.82
$5f^3\,6d$	$((5f_-^2)_4\,(5f_+^1)_{7/2})_7$	−	15	1.543	12448.83
$5f^4$	$((5f_-^2)_4\,(5f_+^2)_6)_7$	+	15	1.574	12703.00
$5f^3\,6d$	$((5f_-^2)_4\,(5f_+^1)_{7/2})_6$	−	13	1.638	13215.90
$5f^3\,6d$	$((5f_-^3)_{3/2}\,(6d_-^1)_{3/2})_3$	−	7	1.695	13675.57
$5f^4$	$((5f_-^1)_{5/2}\,(5f_+^3)_{15/2})_8$	+	17	1.706	13763.62
$5f^3\,6d$	$((5f_-^3)_{3/2}\,(6d_-^1)_{3/2})_0$	−	1	1.792	14456.14
$5f^3\,6d$	$((5f_-^2)_4\,(5f_+^1)_{7/2})_8$	−	17	1.829	14756.54
$5f^4$	$((5f_-^4)_2)_2$	+	5	1.927	15545.87
$5f^4$	$((5f_-^3)_{9/2}\,(5f_+^1)_{7/2})_1$	+	3	2.009	16206.81
$5f^3\,6d$	$((5f_-^2)_4\,(5f_+^1)_{7/2})_6$	−	13	2.089	16854.64
$5f^3\,6d$	$((5f_-^2)_4\,(5f_+^1)_{7/2})_7$	−	15	2.291	18483.69
$5f^3\,6d$	$((5f_-^3)_{9/2}\,(6f_-^1)_{5/2})_5$	−	11	2.297	18528.15
$5f^4$	$((5f_-^4)_4)_4$	+	9	2.311	18641.07
$5f^3\,7s$	$((5f_-^3)_{9/2}\,(7s_+1)_1$	−	9	2.435	19641.45
$5f^3\,6d$	$((5f_-^3)_{9/2}\,(6f_-^1)_{5/2})_4$	−	9	2.495	20125.32
$5f^4$	$((5f_-^3)_{3/2}\,(5f_+^1)_{7/2})_3$	+	7	2.516	20292.87
$5f^4$	$((5f_-^3)_{3/2}\,(5f_+^1)_{7/2})_2$	+	5	2.550	20569.32
$5f^3\,7s$	$((5f_-^3)_{9/2}\,(7s_+^1)_1)_5$	−	11	2.571	20744.00
$5f^4$	$((5f_-^3)_{9/2}\,(5f_+^1)_{7/2})_2$	+	5	2.612	21070.00
$5f^3\,6d$	$((5f_-^3)_{9/2}\,(6f_-^1)_{5/2})_3$	−	7	2.643	21321.86
$5f^3\,6d$	$((5f_-^2)_2\,(5f_+^1)_{7/2})_1$	−	3	2.647	21352.68
$5f^3\,6d$	$((5f_-^3)_{3/2}\,(6f_-^1)_{5/2})_4$	−	9	2.657	21436.20
$5f^4$	$((5f_-^3)_{9/2}\,(5f_+^1)_{7/2})_3$	+	7	2.712	21876.84
$5f^3\,6d$	$((5f_-^1)_{5/2}\,(5f_+^2)_6)_9$	−	19	2.745	22146.87
$5f^4$	$((5f_-^3)_{9/2}\,(5f_+^1)_{7/2})_6$	+	13	2.747	22156.90
$5f^3\,6d$	$((5f_-^2)_2\,(5f_+^1)_{7/2})_2$	−	5	2.771	22356.95
$5f^4$	$((5f_-^2)_2\,(5f_+^2)_6)_4$	+	9	2.829	22824.79
$5f^3\,6d$	$((5f_-^1)_{5/2}\,(5f_+^2)_6)_8$	−	17	2.868	23139.74
$5f^4$	$((5f_-^3)_{3/2}\,(5f_+^1)_{7/2})_5$	+	11	2.876	23199.21
$5f^3\,6d$	$((5f_-^3)_{9/2}\,(6f_-^1)_{5/2})_2$	−	5	2.897	23367.24
$5f^3\,6d$	$((5f_-^2)_4\,(5f_+^1)_{7/2})_7$	−	15	2.929	23624.77
$5f^3\,6d$	$((5f_-^2)_4\,(5f_+^1)_{7/2})_{11/2}$	−	12	2.967	23937.13
$5f^4$	$((5f_-^3)_{9/2}\,(5f_+^1)_{7/2})_7$	+	15	2.971	23970.13
$5f^3\,6d$	$((5f_-^2)_4\,(5f_+^1)_{7/2})_6$	−	13	3.083	24868.54
$5f^3\,6d$	$((5f_-^3)_{9/2}\,(6f_-^1)_{5/2})_3$	−	7	3.122	25182.27
$5f^3\,6d$	$((5f_-^3)_{3/2}\,(6d_-^1)_{3/2})_2$	−	5	3.154	25442.71
$5f^3\,6d$	$((5f_-^2)_4\,(5f_+^1)_{7/2})_5$	−	11	3.190	25730.02
$5f^4$	$((5f_-^1)_{5/2}\,(5f_+^3)_{15/2})_5$	+	11	3.197	25786.23
$5f^4$	$((5f_-^2)_4\,(5f_+^2)_6)_4$	+	9	3.218	25957.35

and susceptible to relativistic effects. Similarly, we calculated lower values for the level energies of $5f^2\ 6d^2$ when compared to the other results, arguably due to this same effect. Furthermore, as discussed for the calculations on Nd III, the number of configurations included in the FAC calculation for U III is not enough to ensure a convergence of the results nor the inclusion of the most important correlation effects to a full extent. For this reason, these results can still be improved in further calculations with a larger basis set.

Nonetheless, we are convinced that the FAC calculations are reasonably accurate, since only slight discrepancies of $\Delta E \sim 1$ eV were observed for the few levels for which experimental data is available, which is within the uncertainty of the FAC code.

It is important to notice that, as predicted, the level density of low-lying levels is significantly greater when compared to the previously discussed calculations on Nd III, as it can be seen from Figure 3.12. Despite the fact that the same number of levels were calculated in both situations (due to the identical structure of the configurations utilized in the basis set), we notice a considerably greater level density at energies below 10 eV. This is specially important for the opacity calculations, as the population of low-lying levels is favored in LTE conditions.

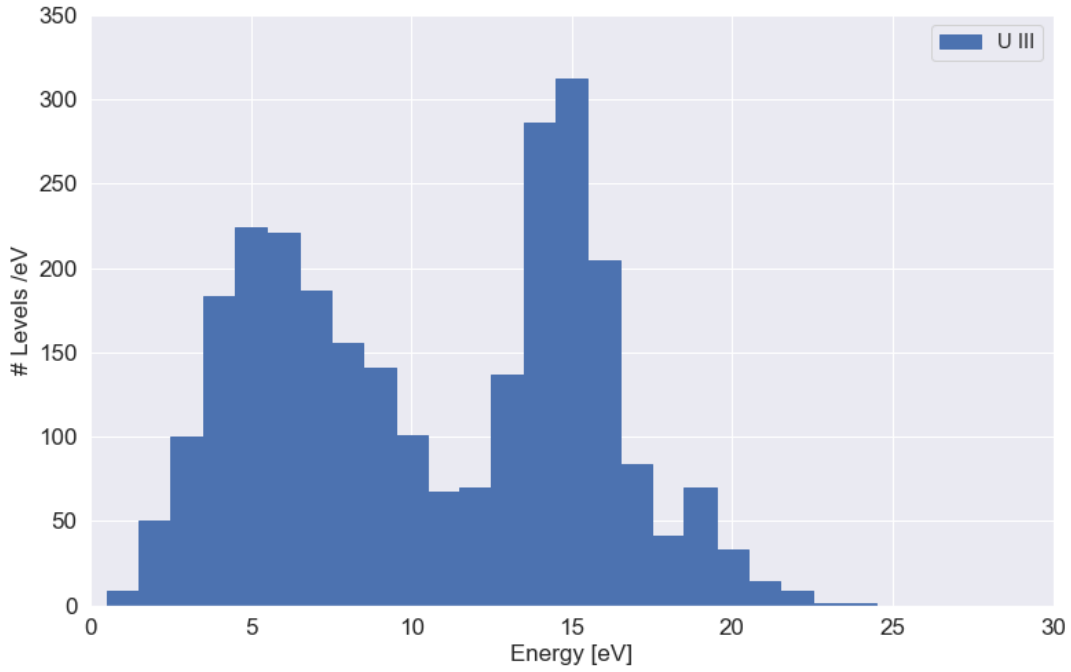

Figure 3.12: Level density distribution of U III as calculated from FAC.

Table 3.7: Wavelength and gf-values for 45 E1 transitions of U III. The states are labeled according to the FAC classification under a jj-coupling scheme. A full description of the notation used in the level classification is given in Section 3.1.1.

Upper level	Lower Level	Wavelength [Å]	gf
$((5f_-^4)_4)_4$	$((5f_-^3)_{3/2}(6d_-^1)_{3/2})_3$	12680.5979	1.22721e-04
$((5f_-^4)_4)_4$	$((5f_-^3)_{9/2}(6d_+^1)_{5/2})_5$	10663.76	3.22539e-06
$((5f_-^4)_4)_4$	$((5f_-^3)_{9/2}(7s_+^1)_{1/2})_4$	10358.21	1.18116e-04
$((5f_-^4)_4)_4$	$((5f_-^3)_{9/2}(6d_+^1)_{5/2})_4$	10032.12	1.38784e-03
$((5f_-^4)_4)_4$	$((5f_-^3)_{9/2}(7s_+^1)_{1/2})_5$	8723.27	1.04805e-05
$((5f_-^4)_4)_4$	$((5f_-^3)_{9/2}(6d_+^1)_{5/2})_3$	8628.18	1.51141e-05
$((5f_-^4)_4)_4$	$((5f_-^3)_{3/2}(6d_+^1)_{5/2})_4$	8438.50	4.28958e-04
$((5f_-^4)_4)_4$	$((5f_-^2)_4(5f_+^1)_{7/2})_{11/2}$	7358.66	9.24586e-05
$((5f_-^3)_{9/2}(6d_-^1)_{3/2})_6$	$((5f_-^2)_4(5f_+^2)_6)_7$	18907.42	1.81441e-05
$((5f_-^3)_{9/2}(6d_-^1)_{3/2})_6$	$((5f_-^3)_{9/2}(5f_+^1)_{7/2})_6$	8959.30	2.58323e-03
$((5f_-^3)_{9/2}(6d_-^1)_{3/2})_6$	$((5f_-^3)_{3/2}(5f_+^1)_{7/2})_5$	8707.04	5.96741e-06
$((5f_-^3)_{9/2}(6d_-^1)_{3/2})_6$	$((5f_-^3)_{9/2}(5f_+^1)_{7/2})_7$	7884.79	5.29508e-04
$((5f_-^3)_{9/2}(5f_+^1)_{7/2})_5$	$((5f_-^2)_4(5f_+^1)_{7/2})_{11/2}$	24616.32	6.74774e-03
$((5f_-^3)_{9/2}(5f_+^1)_{7/2})_5$	$((5f_-^2)_4(5f_+^1)_{7/2})_{9/2}$	14596.76	6.42041e-05
$((5f_-^3)_{9/2}(5f_+^1)_{7/2})_5$	$((5f_-^3)_{9/2}(6d_+^1)_{5/2})_5$	13942.13	3.02563e-03
$((5f_-^3)_{9/2}(5f_+^1)_{7/2})_5$	$((5f_-^3)_{9/2}(7s_+^1)_{1/2})_4$	13424.40	2.38481e-05
$((5f_-^3)_{9/2}(5f_+^1)_{7/2})_5$	$((5f_-^3)_{9/2}(6d_+^1)_{5/2})_4$	12881.73	6.02619e-04
$((5f_-^3)_{9/2}(5f_+^1)_{7/2})_5$	$((5f_-^3)_{9/2}(7s_+^1)_{1/2})_5$	10800.83	4.97735e-05
$((5f_-^3)_{9/2}(5f_+^1)_{7/2})_5$	$((5f_-^3)_{3/2}(6d_+^1)_{5/2})_4$	10367.64	3.26256e-03
$((5f_-^3)_{9/2}(5f_+^1)_{7/2})_5$	$((5f_-^2)_4(5f_+^1)_{7/2})_{11/2}$	8783.97	1.00619e-04
$((5f_-^3)_{9/2}(5f_+^1)_{7/2})_5$	$((5f_-^2)_4(5f_+^1)_{7/2})_{11/2}$	8493.11	1.40892e-06
$((5f_-^3)_{9/2}(6d_-^1)_{3/2})_5$	$((5f_-^4)_4)_4$	15363.97	1.50968e-05
$((5f_-^3)_{9/2}(6d_-^1)_{3/2})_5$	$((5f_-^3)_{9/2}(5f_+^1)_{7/2})_6$	11039.26	2.17988e-03
$((5f_-^3)_{9/2}(6d_-^1)_{3/2})_5$	$((5f_-^2)_2(5f_+^2)_6)_4$	10944.77	6.31478e-05
$((5f_-^3)_{9/2}(6d_-^1)_{3/2})_5$	$((5f_-^3)_{3/2}(5f_+^1)_{7/2})_5$	10658.78	3.79072e-05
$((5f_-^2)_4(5f_+^2)_6)_6$	$((5f_-^2)_4(5f_+^1)_{7/2})_{9/2}$	20992.04	1.39145e-04
$((5f_-^2)_4(5f_+^2)_6)_6$	$((5f_-^2)_4(5f_+^1)_{7/2})_{11/2}$	19670.06	1.00509e-02
$((5f_-^2)_4(5f_+^2)_6)_6$	$((5f_-^3)_{9/2}(6d_+^1)_{5/2})_5$	19664.21	3.68230e-04
$((5f_-^2)_4(5f_+^2)_6)_6$	$((5f_-^3)_{9/2}(7s_+^1)_{1/2})_5$	13944.23	3.97217e-06
$((5f_-^2)_4(5f_+^2)_6)_6$	$((5f_-^2)_4(5f_+^1)_{7/2})_{11/2}$	11371.44	7.32052e-04
$((5f_-^2)_4(5f_+^2)_6)_6$	$((5f_-^2)_4(5f_+^1)_{7/2})_{11/2}$	10755.87	1.32505e-04
$((5f_-^2)_4(5f_+^2)_6)_6$	$((5f_-^2)_4(5f_+^1)_{7/2})_{11/2}$	10322.97	2.00939e-03
$((5f_-^2)_4(5f_+^1)_{7/2})_{11/2}$	$((5f_-^3)_{9/2}(5f_+^1)_{7/2})_6$	13264.12	3.33829e-07
$((5f_-^2)_4(5f_+^1)_{7/2})_{11/2}$	$((5f_-^3)_{9/2}(5f_+^1)_{7/2})_7$	11037.30	2.78824e-04
$((5f_-^2)_4(5f_+^2)_6)_7$	$((5f_-^1)_{5/2}(5f_+^2)_6)_{13/2}$	16335.50	1.49941e-02
$((5f_-^2)_4(5f_+^2)_6)_7$	$((5f_-^2)_4(5f_+^1)_{7/2})_{11/2}$	14630.58	1.97670e-04
$((5f_-^2)_4(5f_+^2)_6)_7$	$((5f_-^2)_4(5f_+^1)_{7/2})_{11/2}$	12939.67	5.02753e-06
$((5f_-^2)_4(5f_+^1)_{7/2})_{11/2}$	$((5f_-^3)_{9/2}(5f_+^1)_{7/2})_6$	17075.34	3.11473e-05
$((5f_-^2)_4(5f_+^1)_{7/2})_{11/2}$	$((5f_-^3)_{3/2}(5f_+^1)_{7/2})_5$	16181.88	1.91769e-05
$((5f_-^2)_4(5f_+^1)_{7/2})_{11/2}$	$((5f_-^3)_{9/2}(5f_+^1)_{7/2})_7$	13554.82	1.40039e-03
$((5f_-^3)_{3/2}(6d_-^1)_{3/2})_3$	$((5f_-^3)_{9/2}(5f_+^1)_{7/2})_3$	24986.33	2.94600e-04
$((5f_-^3)_{3/2}(6d_-^1)_{3/2})_3$	$((5f_-^2)_2(5f_+^2)_6)_4$	23169.99	1.22704e-05
$((5f_-^1)_{5/2}(5f_+^3)_{15/2})_8$	$((5f_-^1)_{5/2}(5f_+^2)_6)_{13/2}$	23364.53	1.02539e-03
$((5f_-^1)_{5/2}(5f_+^3)_{15/2})_8$	$((5f_-^2)_4(5f_+^1)_{7/2})_{11/2}$	20026.63	1.07978e-03
$((5f_-^2)_4(5f_+^1)_{7/2})_{11/2}$	$((5f_-^3)_{9/2}(5f_+^1)_{7/2})_7$	18951.30	5.40646e-06

3.2.2 Oscillator Strengths and $\Gamma(\lambda)$ for U III

Figure 3.13: Results for the weighted oscillator strengths of U III and comparison with the results of Calculation B of Nd III

Looking at the gf-values of doubly ionized uranium, we notice that the distribution of points is almost identical as in the case of Nd III. To facilitate this comparison, the gf-values for both the FAC calculation of U III and for the FAC Calculation B of Nd III are shown in Figure 3.13. This is not surprising given the identical shell structure of both ions. Hence, the possible E1 transitions of U III will be analogous to those computed for Nd III, with the only difference being the principal quantum numbers of the upper and lower levels. The only noticeable difference on the distribution of the gf-values lies on the two peaks found at around $\lambda \sim (8000 - 9000)$ Å . In the case of U III the first peak appears at a lower wavelength than in the case of Nd III. The wavelength and

We must recognize that the FAC gf-values for the $7d \rightarrow 8p$ transitions in U III may be overestimated, analogously to the $6d \rightarrow 7p$ transition in Nd III. In any case, just like in the neodymium case, for most the transitions between these two shells $\Gamma_k(\lambda) < 10^{-10}$ cm, making the atomic contribution of this specific transition negligible when compared to the overall contribution of U III E1 transitions. As a result, even if the contribution of these lines is larger than in the case of Nd III, it will still not offer any important contribution to the expansion opacities.

Despite the similarities of both ions on the oscillator strength distributions, the atomic contribution of those lines to the opacity, which we quantify using the $\Gamma(\lambda)$ parameter, is significantly larger in the case of the actinide, as we can see from Figure 3.14. In fact, for an analogous E1 transition k in U III and Nd III, we find that in general $E_k^{\mathrm{UIII}} < E_k^{\mathrm{NdIII}}$. Hence, higher density of low-lying levels in U III contributes to an overall increase of $\Gamma_k(\lambda)$ which has

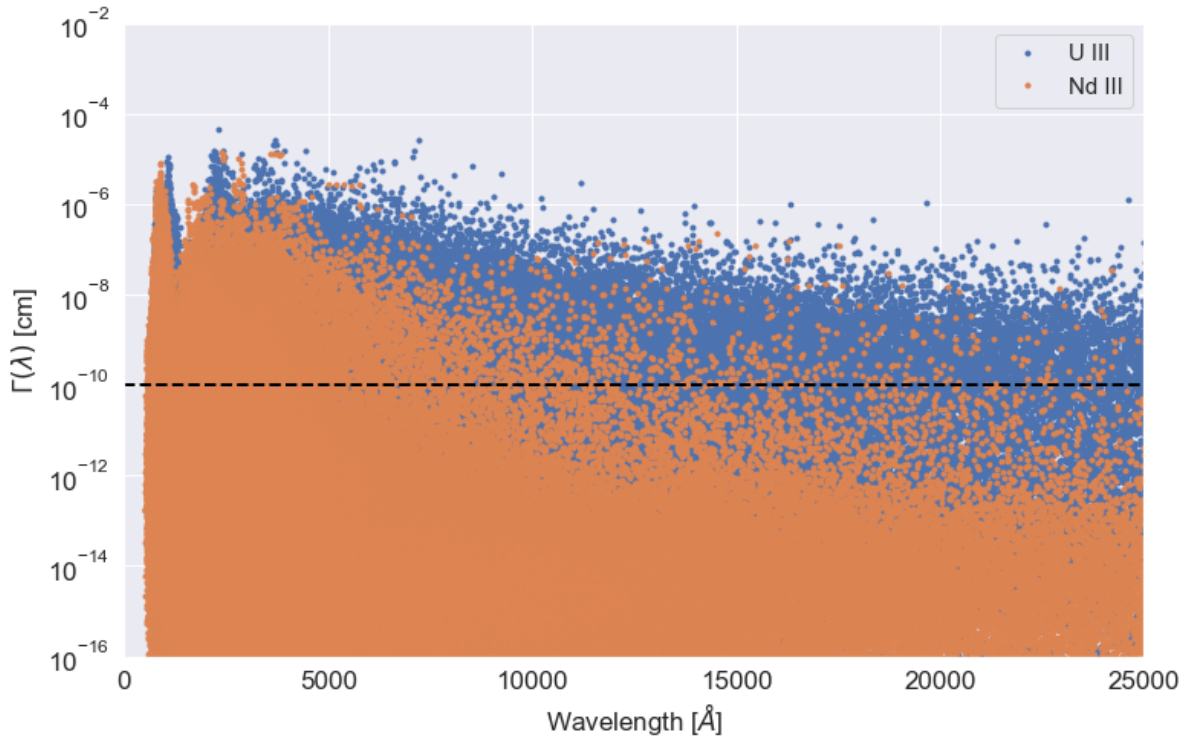

Figure 3.14: Plot of $\Gamma(\lambda)$ for the results obtained by the FAC calculations for UIII compared with Calculation B of Nd III.

a significant impact in the opacities, as it will be seen in Section 3.2.3 . We observe that this discrepancy is considerably greater at infrared wavelengths.

Ion	Number of lines		
	UV	Visible	IR
	(0-4000)Å	(4000-8000)Å	(8000 - 25000)Å
U III (FAC)	150425	32126	21441
Nd III (FAC-B)	67878	3008	924

Table 3.8: Comparison between the number of strong lines computed with FAC for UIII and NdIII (Calculation B) in the UV, visible and IR wavelength ranges.

A better way to quantify this difference in $\Gamma_k(\lambda)$ and assess the atomic contribution of each ion is to count the number of strong lines under the wavelength range of interest. As one can see from Section 3.2.2, where a systematization of the number of strong lines (with $\Gamma_k(\lambda) > 10^{-10}$ cm according to this work) is provided, the number of strong lines in U III is greater to the number of strong lines in Nd III by at least one order of magnitude, consistently through all wavelength ranges. Greater differences are found, once again, in the visible and in the IR which indicates that the main differences in the opacity spectra between these two elements should be found at these two wavelength ranges.

Finally, as it is depicted in Figure 3.16, our characterization of strong lines by defining a threshold on $\Gamma(\lambda)_k$, $\Gamma_k(\lambda) > 10^{-10}$ cm, actually accounts for significantly more lines than the definition used in other works ([2, 3, 39, 70]). The difference is particularly noticeable for uranium, since the total number of strong lines decreases more steadily with the wavelength

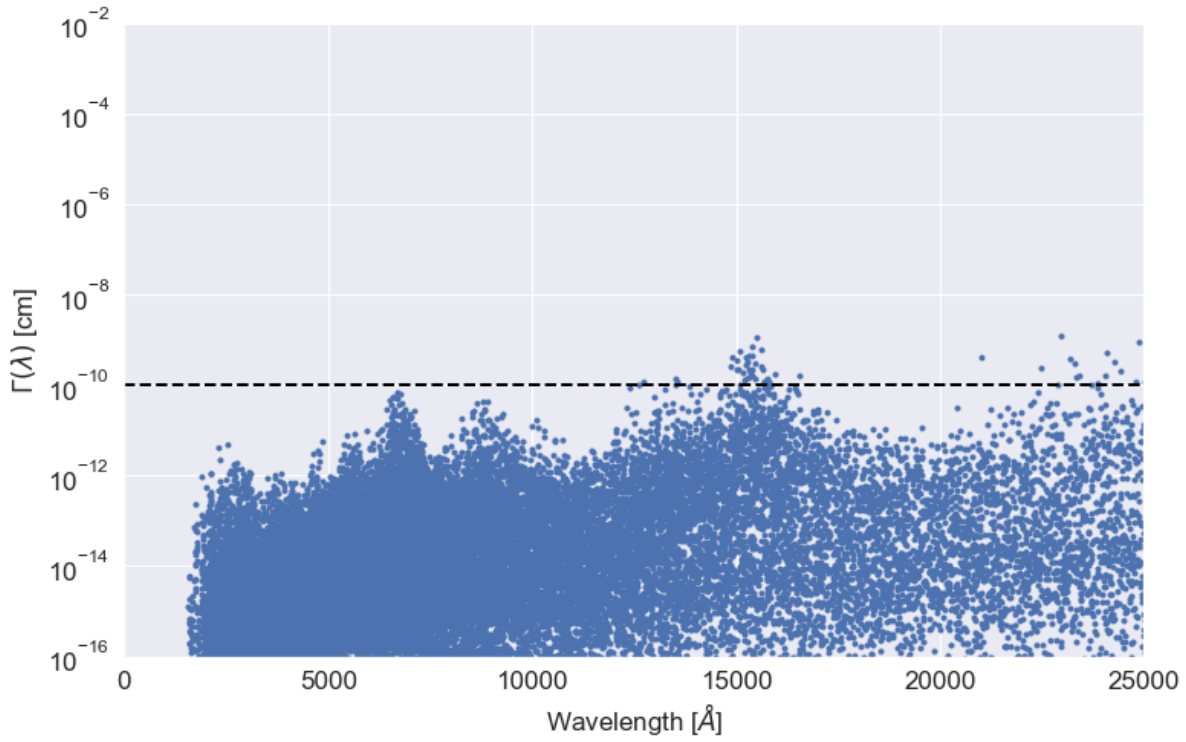

Figure 3.15: Comparison of the results of the different calculations for the oscillator strengths of Nd III, plotted as a function of the wavelength, for all the transitions that occur between the $4f^3 6d$ and the $4f^3 7p$.

than for neodymium. Although this discrepancy should only have a measurable impact at the highest IR wavelengths, it is important to keep this effect in mind when filtering the atomic data, for instance, to reduce the computation time when modeling the luminosity of kilonovae. Nevertheless, and independently of the definition of "strong lines" used, in this astrophysical context one should never consider only a line's gf-value as a measure of its strength as this could lead to erroneous interpretations.

3.2.3 Opacity of U III

Just as in the case of Nd III, the expansion opacity of U III was calculated under the LTE approximation over a time period of one day after the explosion at a temperature of $T = 10000$K for a density $\rho = 10^{-13}$ cm^{-3}. Following the discussion in Section 3.1.5, and to provide a more reliable comparison to the results of neodymium, a ionic density of $z_{\mathrm{UIII}} = 0.01$ was used for the calculations. The results are presented in Figure 3.17, along with a comparison to the results for the expansion opacity of Nd III according to the FAC Calculation B.

As is readily apparent, the opacity of U III is nearly and order of magnitude greater than in the case of Nd III, as it was predicted by the analysis of the atomic contribution of each ion in the previous section. The difference is especially prominent in the visible, and while it remains significant in the IR, it is less noticeable because of the large fluctuations in the opacity of Nd III.

Furthermore, the opacity fluctuations with wavelength are considerably reduced in the case of U III. The high Γ_k for uranium minimize the opacity's dependency on the optical depth since $1 - e^{-\tau} \sim 1$ for $\Gamma \gtrsim 10^{-10}$cm. Not only does this decrease dispersion on the opacities for a

Figure 3.16: Number of strong lines for Nd III and U III, by $\Gamma > 10^{-10}$ cm^{-1} (filled lines) and by $gfe^{-E/k_BT} > 10^{-5}$ (dotted lines).

given wavelength bin, but it also reduces the opacities' sensitivity to specific Γ_k and oscillator strength values. In this limit, the expansion opacity can, be approximated by

$$\kappa_{\text{exp}} \approx \frac{1}{\rho c t_{exp}} \sum_k \frac{\lambda_k}{\Delta\lambda} \tag{3.4}$$

Additionally, if we neglect the variation of wavelength within a specific bin

$$\kappa_{\text{exp}} \approx \frac{1}{\rho c t_{exp}} \lambda \sum_k \frac{1}{\Delta\lambda} = \frac{1}{\rho c t_{exp}} \lambda \frac{N}{\Delta\lambda} \tag{3.5}$$

Equation (3.5) emphasize the importance of the number lines taken into account in these calculations. Given a high optical depth and under LTE conditions, the major contribution to opacity comes from the ion's line count per unit of wavelength and not from individually strong transitions. As a result, the precision of individual lines will be negligible in environments where the density of levels is sufficiently high to sustain local thermodynamical equilibrium and a high optical depth. These insights are particularly pertinent in the case of lanthanides and actinides, owing to their extremely complicated shell structure, which makes accurate computation extremely difficult to achieve within a reasonable amount of time and computer resources.

Another interesting observation is that the number of lines of both actinide and lanthanide elements seems to vary smoothly with the wavelength. In particular, we found that after the initial peak at $\lambda \sim 1000$ Å that the number of transitions decreases smoothly with $N \sim \lambda^{-2}$, specially at infrared wavelengths. Substituting the number of transitions by its wavelength dependence in, Equation (3.5) we can obtain a parametrization of the opacities with the wavelength:

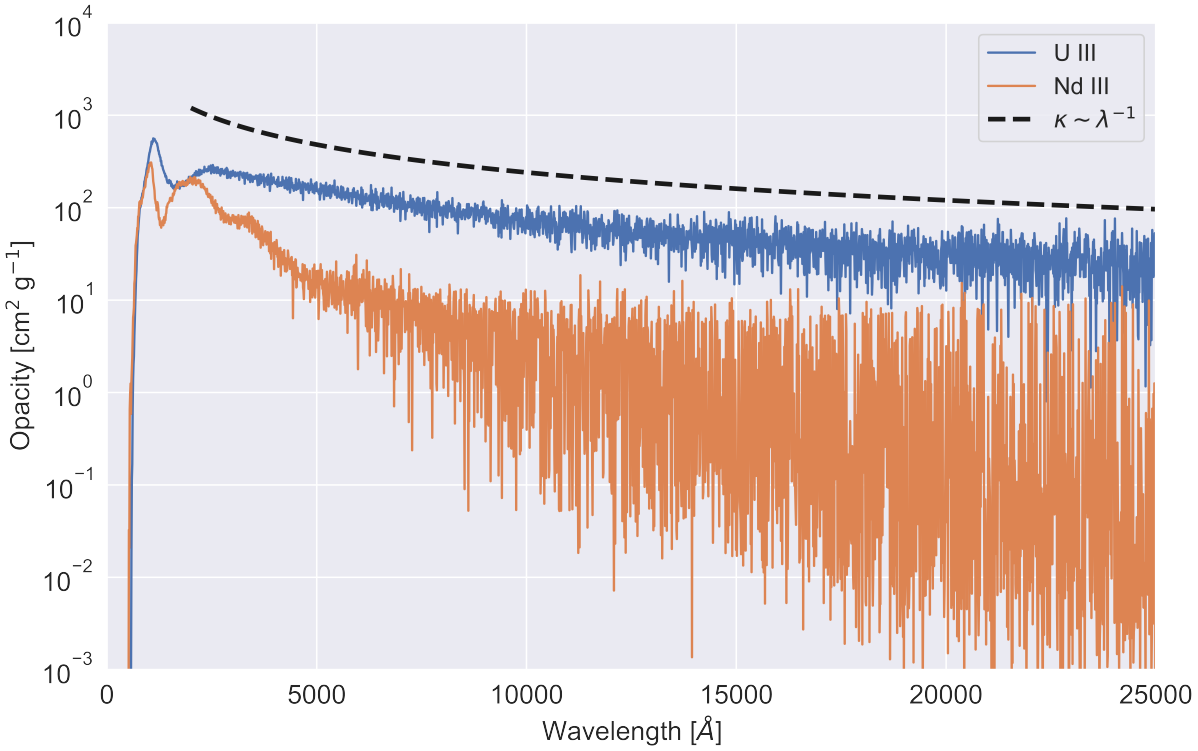

Figure 3.17: Expansion opacity for U III from the calculations performed with FAC. The results are compared with the with opacity for Nd III obtained with Calculation B from FAC and a sum of the contribution of both ions to the opacities is shown in black. The opacity was evaluated at $t = 1$ day for the typical density and temperature values of $\rho = 10^{-13}$ cm^{-3}and $T = 10000$ K assumed by other calculations. The black dashed line highlights the wavelength dependence of the opacity following approximately a λ^{-1} power law

$$\kappa_{\text{exp}} = \frac{1}{\rho c t_{exp}} \lambda \frac{\lambda^{-2}}{\Delta\lambda} \sim \lambda^{-1} \tag{3.6}$$

This power law parametrization of the opacities, which is also highlighted in, Figure 3.17, describes particularly well the evolution of the opacity spectra for U III, since the number of lines that have an important contribution to the opacity is consistently high in the considered wavelength range. For the case of Nd III, with a much lower number of strong lines, this parametrization gives, at most, a upper limit of the expansion opacity spectra.

Nonetheless, this parametrization can be useful in differentiating the contributions of actinides and lanthanides to the opacity ejecta. The high density of low-energy levels should be consistent for the different actinides, Hence, a high dependence of their opacities with the number of transitions is expected which makes this parametrization possibly valid. This effect won't be so notorious for lanthanides due to the fluctuations of the opacities at high wavelengths caused by a low optical depth, which increases the opacities' dependence on the gf-values.

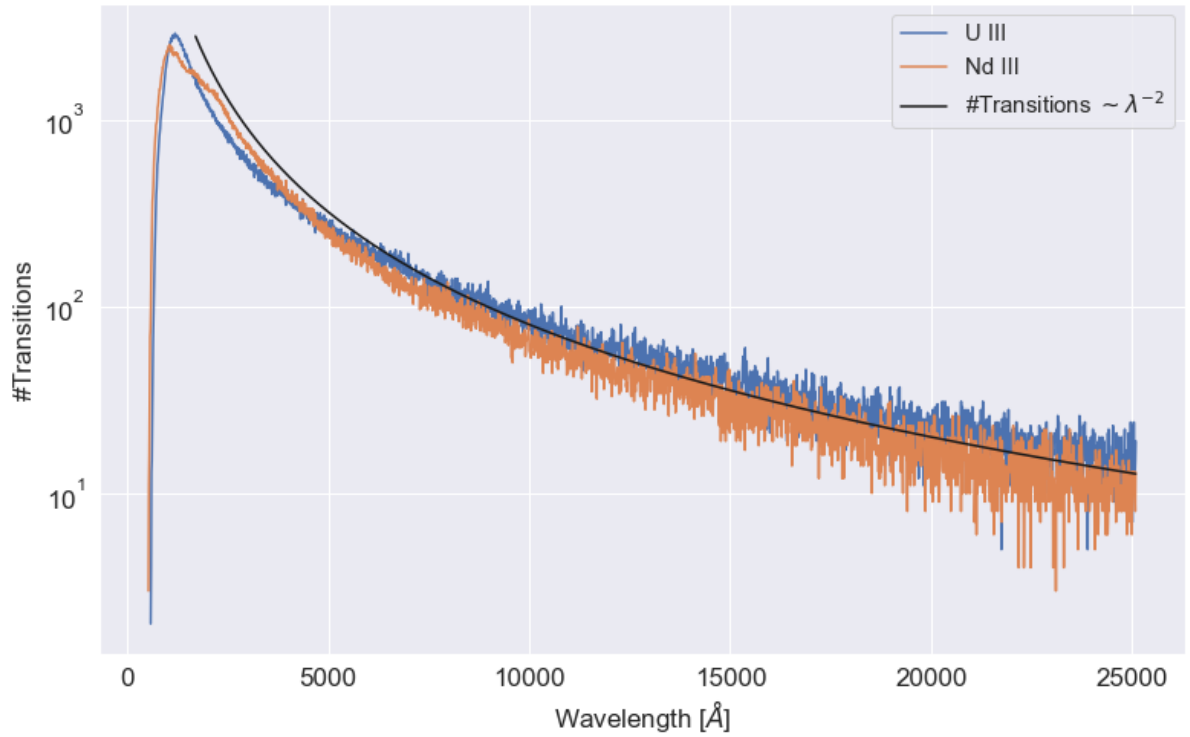

Figure 3.18: Total number of lines for Nd III and U III as a function of the wavelength. The power law dependence with the wavelength is highlighted.

Chapter 4

Conclusions and future prospects

The roots of this work lie in the change of paradigm in r-process research associated with the direct observational data from kilonovae explosions. The observation of the kilonova electromagnetic transient associated with the gravitational wave signal GW170817, provide the first indication that heavy r-process elements, in particular lanthanides and actinides, are produced in NSM. In this work we have tried, not only, to supply reliable data for two representative rare-earth ions, Nd III and U III, but, most importantly, we have analyzed some of the caveats of these calculations that must be taken into consideration when large-scale calculations are achieved.

With the computational expense of the calculations in mind, the FAC code has been used to compute level energies and transitions wavelengths and oscillator strengths for electric dipole (E1) transitions for the two mentioned ions. We have noticed a reasonable agreement of the energies of low-lying levels with experimental data as well as with other theoretical calculations achieved with the GRASP2K code (for Nd III) and with the CI+LCC method (for U III). Furthermore, when compared to the calculations available in the literature using other methods, we were able to compute a substantially larger quantity of data and in a fraction of the time required by those approaches.

Although some discrepancies were found for the gf-values of Nd III when compared with calculations from MCDFGME and GRASP2K, we have shown that they should not have any measurable impact in expansion opacities. In fact, the opacity spectra of Nd III obtained in [3] using the atomic data supplied by GRASP2K was fully reproduced in the IR, and differences in the UV are explained by the inclusion of higher energy states in our calculation.

In any case, it is important to remember that the FAC calculations achieved in this work only include a very small number of configurations in the basis set of the RCI calculation. Although this approach is in line with other works (for instance [2]) it does not guarantee the convergence of the results and, hence, the level energies may vary significantly with the inclusion of a larger number of configurations. A more detailed study of the electronic correlation of different shells and more precise structure calculations for Nd III, U III and other relevant ions are planned for future works. Nevertheless, we have demonstrated that FAC calculations, even with the inclusion of only a few configurations in the basis set, may provide a viable alternative for calculation of the atomic parameters in large-scale opacity calculations, specially at redder wavelengths.

It is important to mention that this is one of the very first few works that takes into account the impact that actinides can have in the kilonovae opacity spectra. In this work, we predict the opacity of U III to be roughly an order of magnitude higher than of Nd III, in all wavelength

ranges of interest. Moreover, the larger number of strong transitions of uranium makes the spectra extremely reliant on the number of transitions included in the making, making the precision of individual lines negligible. Due to the higher density of levels characteristic of actinide elements when compared to lanthanides, we predict these differences to extend beyond Nd III and U III. Therefore, despite the predictions of very low mass fractions of actinides to be present in the kilonovae ejecta [74], the impact of these ions must not be neglected as they could have a measurable impact in the evolution of the flux and light-curves.

These predictions must be validated by including this atomic data into radiative transfer simulations of kilonovae. Furthermore, additional calculations of various lanthanide and actinide ions are still required, as are accurate calculations of collisional excitation cross sections and photoionization rates for realistic modeling in non-LTE regimes. All of these tasks must be addressed in future works.

References

[1] M. R. Wu, I. Tamborra, O. Just, and H. T. Janka, Phys. Rev. D **96** (2017) 10.1103/PhysRevD.96.123015 (cited on pages v, 9).

[2] M. Tanaka, D. Kato, G. Gaigalas, and K. Kawaguchi, Mon. Not. R. Astron. Soc. **496**, 1369 (2020) 10.1093/mnras/staa1576 (cited on pages vi, 8, 16, 33, 38, 44, 48, 57, 63).

[3] G. Gaigalas, D. Kato, P. Rynkun, L. Radžit, M. Tanaka, L. Radžite, and M. Tanaka, Astrophys. J. Suppl. Ser. **240**, 29 (2019) 10.3847/1538-4365/aaf9b8 (cited on pages vi, 33, 35–36, 43–44, 50, 57, 63).

[4] P. Jönsson, G. Gaigalas, J. Bieroń, C. F. Fischer, and I. P. Grant, Comput. Phys. Commun. **184**, 2197 (2013) 10.1016/j.cpc.2013.02.016 (cited on pages vi, 9, 29, 35).

[5] I. Savukov, U. I. Safronova, and M. S. Safronova, Phys. Rev. A **92**, 052516 (2015) 10.1103/PhysRevA.92.052516 (cited on pages vi, 51–52).

[6] M. S. Safronova, M. G. Kozlov, W. R. Johnson, and D. Jiang, Phys. Rev. A **80**, 012516 (2009) 10.1103/PhysRevA.80.012516 (cited on pages vi, 51–52).

[7] J. Barnes and D. Kasen, Astrophys. J. **775** (2013) 10.1088/0004-637X/775/1/18 (cited on pages 4–5, 33).

[8] J. A. Johnson, B. D. Fields, and T. A. Thompson, Philosophical Transactions of the Royal Society A: Mathematical, Physical and Engineering Sciences **378**, 20190301 (2020) 10.1098/rsta.2019.0301 (cited on page 4).

[9] C. E. Rolfs and W. S. Rodney, *Cauldrons in the cosmos : nuclear astrophysics* (University of Chicago Press, 1988), page 561 (cited on page 4).

[10] C. Fröhlich, J. Phys. G Nucl. Part. Phys. **41** (2014) 10.1088/0954-3899/41/4/044003 (cited on page 4).

[11] T. A. Thompson, A. Burrows, and B. S. Meyer, Astrophys. J. **562**, 887 (2001) 10.1086/323861 (cited on page 4).

[12] A Arcones, H.-T. Janka, and L Scheck, Astron. Astrophys. **467**, 1227 (2007) 10.1051/0004-6361:20066983 (cited on page 4).

[13] T Fischer, S. C. Whitehouse, A Mezzacappa, F. K. Thielemann, and M Liebendörfer, Astron. Astrophys. **517**, 80 (2010) 10.1051/0004-6361/200913106 (cited on page 4).

[14] L. Hüdepohl, B. Müller, H.-T. T. Janka, A. Marek, and G. G. Raffelt, Phys. Rev. Lett. **104**, 251101 (2010) 10.1103/PhysRevLett.104.251101 (cited on page 4).

[15] L. F. Roberts, S. E. Woosley, and R. D. Hoffman, Astrophys. J. **722**, 954 (2010) 10.1088/0004-637X/722/1/954 (cited on page 4).

[16] G. Martínez-Pinedo, T. Fischer, A. Lohs, and L. Huther, Phys. Rev. Lett. **109**, 1 (2012) 10.1103/PhysRevLett.109.251104 (cited on page 4).

[17] L. F. Roberts, S. Reddy, and G. Shen, Phys. Rev. C - Nucl. Phys. **86**, 1 (2012) 10.1103/PhysRevC.86.065803 (cited on page 4).

[18] K. Langanke, G. Martínez-Pinedo, B. Müller, H. T. Janka, A. Marek, W. R. Hix, A. Juodagalvis, and J. M. Sampaio, Phys. Rev. Lett. **100** (2008) 10.1103/PhysRevLett.100.011101 (cited on page 4).

[19] G. Martínez-Pinedo, T. Fischer, and L. Huther, J. Phys. G Nucl. Part. Phys. **41**, 1 (2014) 10.1088/0954-3899/41/4/044008 (cited on page 4).

[20] M. Bulla, Mon. Not. R. Astron. Soc. **489**, 5037 (2019) 10.1093/mnras/stz2495 (cited on page 4).

[21] C. Y. Cardall and G. M. Fuller, Astrophys. J. **486**, L111 (1997) 10.1086/310838 (cited on page 5).

[22] P. Banerjee, W. C. Haxton, and Y. Z. Qian, Phys. Rev. Lett. **106**, 201104 (2011) 10.1103/PhysRevLett.106.201104 (cited on page 5).

[23] T. A. Thompson, P. Chang, and E. Quataert, Astrophys. J. **611**, 380 (2004) 10.1086/421969 (cited on page 5).

[24] N. Nishimura, T. Takiwaki, and F.-K. Thielemann, Astrophys. J. **810**, 109 (2015) 10.1088/0004-637X/810/2/109 (cited on page 5).

[25] A. Wallner, T. Faestermann, J. Feige, C. Feldstein, K. Knie, G. Korschinek, W. Kutschera, A. Ofan, M. Paul, F. Quinto, G. Rugel, and P. Steier, Nat. Commun. **6**, 5956 (2015) 10.1038/ncomms6956 (cited on page 5).

[26] Y. Utsumi, M. Tanaka, N. Tominaga, M. Yoshida, S. Barway, T. Nagayama, T. Zenko, K. Aoki, T. Fujiyoshi, H. Furusawa, K. S. Kawabata, S. Koshida, C. H. Lee, T. Morokuma, K. Motohara, F. Nakata, R. Ohsawa, K. Ohta, H. Okita, A. Tajitsu, I. Tanaka, T. Terai, N. Yasuda, F. Abe, Y. Asakura, I. A. Bond, S. Miyazaki, T. Sumi, P. J. Tristram, S. Honda, R. Itoh, Y. Itoh, M. Kawabata, K. Morihana, H. Nagashima, T. Nakaoka, T. Ohshima, J. Takahashi, M. Takayama, W. Aoki, S. Baar, M. Doi, F. Finet, N. Kanda, N. Kawai, J. H. Kim, D. Kuroda, W. Liu, K. Matsubayashi, K. L. Murata, H. Nagai, T. Saito, Y. Saito, S. Sako, Y. Sekiguchi, Y. Tamura, M. Tanaka, M. Uemura, and M. S. Yamaguchi, Publ. Astron. Soc. Japan **69**, 69 (2017) 10.1093/pasj/psx118 (cited on page 5).

[27] R. Ciolfi, Front. Astron. Sp. Sci. **7**, 27 (2020) 10.3389/fspas.2020.00027 (cited on page 5).

[28] R. Chornock, E. Berger, D. Kasen, P. S. Cowperthwaite, M. Nicholl, V. A. Villar, K. D. Alexander, P. K. Blanchard, T. Eftekhari, W. Fong, R. Margutti, P. K. G. Williams, J. Annis, D. Brout, D. A. Brown, H. Y. Chen, M. R. Drout, R. J. Foley, J. A. Frieman, C. L. Fryer, D. E. Holz, T. Matheson, B. D. Metzger, E. Quataert, A. Rest, M. Sako, D. M. Scolnic, N. Smith, and M. Soares-Santos, arXiv **848**, L19 (2017) 10.3847/2041-8213/aa905c (cited on page 5).

[29] Abbott, B. P. et al, Astrophys. J. **848**, L12, L12 (2017) 10.3847/2041-8213/aa91c9 (cited on page 5).

[30] L.-X. Li and B. Paczyński, Astrophys. J. **507** (1998) 10.1086/311680 (cited on page 5).

[31] O. Just, S. Goriely, A. Bauswein, M. Obergaulinger, R. A. Pulpillo, and H.-T. Janka, in Jps conf.proc. Vol. 14 (2017), 10.7566/jpscp.14.010704 (cited on page 5).

[32] B. D. Metzger, Living Rev. Relativ. **23** (2020) 10.1007/s41114-019-0024-0 (cited on pages 5, 7, 11).

[33] D. Kasen, B. Metzger, J. Barnes, E. Quataert, and E. Ramirez-Ruiz, Nature **551**, 80 (2017) 10.1038/nature24453 (cited on pages 6, 8, 48).

[34] D. Watson, C. J. Hansen, J. Selsing, A. Koch, D. B. Malesani, A. C. Andersen, J. P. Fynbo, A. Arcones, A. Bauswein, S. Covino, A. Grado, K. E. Heintz, L. Hunt, C. Kouveliotou, G. Leloudas, A. J. Levan, P. Mazzali, and E. Pian, Nature **574**, 497 (2019) 10.1038/s41586-019-1676-3 (cited on pages 6–7).

[35] M. George, M. R. Wu, I. Tamborra, R. Ardevol-Pulpillo, and H. T. Janka, Phys. Rev. D **102**, 103015 (2020) 10.1103/PhysRevD.102.103015 (cited on page 6).

[36] N. Domoto, M. Tanaka, S. Wanajo, and K. Kawaguchi, Astrophys. J. **913**, 26 (2021) 10.3847/1538-4357/abf358 (cited on page 6).

[37] N. R. Badnell, Badnell, and N. R., *AUTOSTRUCTURE: General program for calculation of atomic and ionic properties*, 2016, 10.3847/1538-4357/aaee7d (cited on page 8).

[38] A. Bar-Shalom, M. Klapisch, and J. Oreg, J. Quant. Spectrosc. Radiat. Transf. **71**, 169 (2001) 10.1016/S0022-4073(01)00066-8 (cited on page 8).

[39] K. Hotokezaka, M. Tanaka, D. D. Kato, and G. Gaigalas, Mon. Not. R. Astron. Soc. **000**, 1 (2021) 10.1093/mnras/stab1975 (cited on pages 8, 33, 39, 57).

[40] J. Barnes, "Radiation Transport Modeling of Kilonovae and Broad-lined Ic Supernovae", PhD thesis (2017) (cited on page 8).

[41] P Indelicato, O Gorveix, and J. P. Desclaux, J. Phys. B At. Mol. Phys. **20**, 651 (1987) 10.1088/0022-3700/20/4/007 (cited on pages 9, 26, 29).

[42] K. G. Dyall, I. P. Grant, C. T. Johnson, F. A. Parpia, and E. P. Plummer, Comput. Phys. Commun. **55**, 425 (1989) 10.1016/0010-4655(89)90136-7 (cited on pages 9, 29).

[43] R. G. Eastman and P. A. Pinto, Astrophys. J. **412**, 731 (1993) 10.1086/172957 (cited on page 11).

[44] P. A. Pinto and R. G. Eastman, Astrophys. J. **530**, 744 (2000) 10.1086/308376 (cited on page 11).

[45] P. A. Pinto and R. G. Eastman, Astrophys. J. **530**, 757 (2000) 10.1086/308380 (cited on pages 11, 17).

[46] F. H. Shu, *The physics of astrophysics. Volume 1: Radiation.* (1991) (cited on page 13).

[47] A. K. Prdhan and S. N. Nahar (), https://doi.org/10.1017/CBO9780511975349 (cited on page 13).

[48] A. H. Karp, G. Lasher, K. L. Chan, and E. E. Salpeter, Astrophys. J. **214**, 161 (1977) 10.1086/155241 (cited on page 14).

[49] V. V. Sobolev, *Moving Envelopes of Stars* (Harvard University Press, 1960), 10.4159/harvard.9780674864658 (cited on page 14).

[50] D. Kasen, N. R. Badnell, and J. Barnes, Astrophys. J. **774** (2013) 10.1088/0004-637X/774/1/25 (cited on page 15).

[51] C. J. Fontes, C. L. Fryer, A. L. Hungerford, R. T. Wollaeger, and O. Korobkin, Mon. Not. R. Astron. Soc. **493**, 4143 (2020) 10.1093/mnras/staa485 (cited on pages 16, 33).

[52] E. Tiesinga, P. J. Mohr, D. B. Newell, B. N. Taylor, D. J. Baker, M Douma, and S Kotochigova, *The 2018 CODATA Recommended Values of the Fundamental Physical Constants*, (Web Version 8.1). Gaithersburg, MD (cited on page 19).

[53] S. Weinberg and S. Weinberg, in *Lect. quantum mech.* (Cambridge University Press, Cambridge, 2015), pages 55–103, 10.1017/CBO9781316276105.005 (cited on page 19).

[54] E. F. Westrum, J. Chem. Educ. **41**, A288 (1964) 10.1021/ed041pA288 (cited on page 19).

[55] W. Greiner, *Relativistic Quantum Mechanics* (Springer Berlin Heidelberg, 1995), 10.1007/978-3-642-88082-7 (cited on page 20).

[56] G. Breit, Phys. Rev. **34**, 553 (1929) 10.1103/PhysRev.34.553 (cited on page 20).

[57] O. Gorceix and P. Indelicato, Phys. Rev. A **37**, 1087 (1988) 10.1103/PhysRevA.37.1087 (cited on page 21).

[58] W. R. Johnson, *Atomic structure theory: Lectures on atomic physics* (2007), pages 1–312, 10.1007/978-3-540-68013-0 (cited on pages 23, 26).

[59] P. J. Lestrange, F. Egidi, and X. Li, J. Chem. Phys. **143**, 234103 (2015) 10.1063/1.4937410 (cited on page 26).

[60] I. P. Grant, Comput. Phys. Commun. **84**, 59 (1994) 10.1016/0010-4655(94)90203-8 (cited on page 26).

[61] J. P. Desclaux, Comput. Phys. Commun. **9**, 31 (1975) 10.1016/0010-4655(75)90054-5 (cited on page 26).

[62] M. F. Gu, Can. J. Phys. **86**, 675 (2008) 10.1139/P07-197 (cited on page 29).

[63] S. Fritzsche, Comput. Phys. Commun. **183**, 1525 (2012) 10.1016/j.cpc.2012.02.016 (cited on page 31).

[64] A. Kramida, Y. Ralchenko, and J. Reader, *No Title*, NIST Atomic Spectra Database (ver. 5.8), [Online]. Available: https://physics.nist.gov/asd [2017, April 9]. National Institute of Standards and Technology, Gaithersburg, MD. 2020 (cited on pages 33–35).

[65] D. Kasen, R. C. Thomas, and P. Nugent, Astrophys. J. **651**, 366 (2006) 10.1086/506190 (cited on page 33).

[66] R. D. Cowan, *The Theory of Atomic Structure and Spectra* (University of California Press, 1981), page 731, 10.1525/9780520906150 (cited on pages 33, 50).

[67] H. Carvajal Gallego, P. Palmeri, and P. Quinet, Mon. Not. R. Astron. Soc. **501**, 1440 (2021) 10.1093/mnras/staa3729 (cited on pages 33, 43–44).

[68] A Conroy, C Ramsbottom, C Ballance, F Keenan, A. Conroy, C. Ramsbottom, C. Ballance, and F. Keenan, Galaxies **6**, 91 (2018) 10.3390/GALAXIES6030091 (cited on page 33).

[69] M. Tanaka and K. Hotokezaka, Astrophys. J. **775**, 113 (2013) 10.1088/0004-637X/775/2/113 (cited on page 33).

[70] M. Tanaka, D. Kato, G. Gaigalas, P. Rynkun, L. Radžit, S. Wanajo, Y. Sekiguchi, N. Nakamura, H. Tanuma, I. Murakami, and H. A. Sakaue, Astrophys. J. **852**, 109 (2018) 10.3847/1538-4357/aaa0cb (cited on pages 33, 43, 48, 57).

[71] P.Quinet, P.Palmeri, and A. Physics, *No Title*, Database on Rare Earths At Mons University [Online]. Available: https://hosting.umons.ac.be/html/agif/databases/dream.html [2020, Februrary]. Mons University, Belgium, 2020 (cited on page 35).

[72] C. J. Fontes, C. L. Fryer, and A. L. Hungerford, AIP Conf. Proc. **1811**, 190 (2017) 10.1063/1.4975739 (cited on page 47).

[73] M. Fred, in (1967), pages 180–202, 10.1021/ba-1967-0071.ch014 (cited on page 50).

[74] J. Lippuner, L. F. Roberts, and W. Burke, Astrophys. J. **815**, 82 (2015) 10.1088/0004-637X/815/2/82 (cited on pages 51, 64).

[75] J Blaise and J. F. Wyart, *Energy levels and atomic spectra of actinides.* (Tables internationales de constantes, 1992), page 479 (cited on pages 51–52).

[76] M. G. Kozlov, S. G. Porsev, M. S. Safronova, and I. I. Tupitsyn, Comput. Phys. Commun. **195**, 199 (2015) 10.1016/J.CPC.2015.05.007 (cited on page 51).

[77] P. Hakel, M. E. Sherrill, S. Mazevet, J. Abdallah, J. Colgan, D. P. Kilcrease, N. H. Magee, C. J. Fontes, and H. L. Zhang, J. Quant. Spectrosc. Radiat. Transf. **99**, 265 (2006) 10.1016/j.jqsrt.2005.04.007 (cited on page 51).

[78] S. Nahar, Atoms 2020, Vol. 8, Page 68 **8**, 68 (2020) 10.3390/ATOMS8040068 (cited on page 51).

[79] W Eissner, J. Phys. IV Proc. **1**, C1 (1991) 10.1051/jp4:1991101ï (cited on page 51).